MICROSTRUCTURE AND ELEVATED TEMPERATURE MECHANICAL BEHAVIOR OF Ti-15Al-33Nb AND Ti-21Al-29Nb ALLOYS

BY

CHRISTOPHER J. COWEN

A THESIS
SUBMITTED TO THE FACULTY OF

ALFRED UNIVERSITY

IN PARTIAL FULFILLMENT OF THE REQUIREMENTS
FOR THE DEGREE OF

MASTER OF SCIENCE

IN

MATERIALS SCIENCE AND ENGINEERING

ALFRED, NEW YORK

NOVEMBER, 2004

Alfred University theses are copyright protected and may be used for education or personal research only. Reproduction or distribution in part or whole is prohibited without written permission from the author.

MICROSTRUCTURE AND ELEVATED TEMPERATURE MECHANICAL BEHAVIOR OF Ti-15A1-33Nb AND Ti-21A1-29Nb ALLOYS

BY

CHRISTOPHER J. COWEN

B.S. ALFRED UNIVERSITY (2004)

SIGNATURE OF AUTHOR (Signature on file)

APPROVED BY (Signature on file)
CARL BOEHLERT, ADVISOR

(Signature on file)
ALAN MEIER, ADVISORY COMMITTEE

(Signature on file)
SCOTT MISTURE, ADVISORY COMMITTEE

(Signature on file)
DOREEN EDWARDS, CHAIR, ORAL THESIS DEFENSE

ACCEPTED BY (Signature on file)
ALASTAIR CORMACK, DEAN,
SCHOOL OF ENGINEERING

ACKNOWLEDGEMENTS

I would like to first and foremost thank my advisor Dr. Carl Boehlert, and my thesis committee members Dr. Al Meier and Dr. Scott Misture. I would especially like to thank Dr. Boehlert for giving me the opportunity for graduate study and say that I consider him an excellent advisor and a great friend. I would also like to thank RMI Titanium, Inc. for processing the Ti-Al-Nb.

I would like to thank John, Darlene, Marissa, and Nicole for always being there for me, and I would not be where I am today without their love and support. Special thanks go to my Dad, who machined my mechanical testing samples, which in it itself provided invaluable help in the completion of this thesis.

There are numerous undergrads I would like to thank, because without their hard work this thesis would not have been possible. So, thank you Istvan Szabo, John Rich, Mike Wallace, Katherine Rider, Cassandra Clark, Jesse Struble, Matt Dispenza, and Dan Burnett.

I would also like to thank Gerry Wynick for help with metallography and showing me the Nomarski, Mr. Ward Votava for the SEM assistance, and Dr. Dingqiang Li for the EBSD and TEM work.

As with my bachelors thesis, I would like to dedicate this thesis to the memory of my fraternity brother Benjamin Klein, and my uncle David Root.

TABLE OF CONTENTS

Page

Acknowledgements……...iii

Table of Contents……..iv

List of Tables……vi

List of Figures……viii

I. INTRODUCTION AND BACKGROUND……...1

A. General Titanium Background……..1

B. Orthorhombic Titanium Aluminides……..2

1. Constituent Phases and Crystal Structures……...2

2. Phase Equilibria……4

3. Mechanical Properties……..6

a. Tensile Properties……...6

b. Creep Properties……8

II. OBJECTIVES……..12

III. EXPERIMENTAL PROCEDURE……...13

A. Processing……13

B. Chemical Analysis of Rolled Sheets……...13

C. Microstructural Evaluation……..15

1. Heat Treatments……15

2. Sample Preparation and Metallography……16

3. Microstructures and Phase Volume Fraction Analysis……17

4. Grain Size Analysis……..17

5. Differential Thermal Analysis (DTA)……..18

6. X-ray Diffraction (XRD)……..18

D. Tensile Testing……19

E. Creep Testing……..20

IV. RESULTS……22

A. Microstructure Results……22

1. Chemical Composition of the As-Processed Sheets……22

2. Differential Thermal Analysis……23

3. Solution Treatment Study……25

4. Phase Volume Fractions……..29

5. Grain Size……31
6. X-ray Diffraction……32
7. β-Transus Temperature Determination……...36
8. BCC Grain Growth Kinetics……...36
B. Tensile Study Results……38
1. Room Temperature Behavior……38
2. Elevated Temperature Behavior……42
C. Creep Study Results..……46
1. Steady State Strain Rates, Creep Stress Exponents, and Apparent Activation Energies……...46
2.Proposed Deformation Mechanisms..……57
V. DISCUSSION……...60
A. Microstructure Discussion……...60
1. Phase Equilibria……60
2. Phase Transformation Mechanisms……..65
B. Tensile Behavior Discussion…..……66
1. Room Temperature Ductility……66
2. Grain Size Effects……67
3. Orthorhombic Phase Strengthening……..68
4. Temperature Dependence of Yield Strength……70
C. Creep Behavior Discussion..……..……...71
1. Phase Volume Fraction and Grain Size Effects……71
2. Alloy Comparisons and Deformation Mechanism Map Construction……..73
VI. SUMMARY AND CONCLUSIONS……79
A. Summary……..79
B. Conclusions……..81
1. Processing……81
2. Microstructural Evolution……81
3. Tensile Behavior……...82
4. Creep Behavior……82
5. Evaluation……83
REFERENCES……84
APPENDIX……89

LIST OF TABLES

Page

Table I. Microstructural Influence on Tensile Properties of Ti-Al-Nb alloys……8

Table II. Tensile Test Matrix……19

Table III. Creep Test Matrix……..21

Table IV. Measured Chemical Composition of Ti-17Al-33Nb As-Processed Sheets……..22

Table V. Measured Chemical Composition of Ti-22Al-28Nb As-Processed Sheets……..22

Table VI. Phase Volume Fractions for Ti-15Al-33Nb Microstructures……29

Table VII. Phase Volume Fractions for Ti-21Al-29Nb Microstructures……29

Table VIII. Average Equiaxed Grain Size for Ti-15Al-33Nb and Ti-21Al-29NbMicrostructures……...31

Table IX. Room Temperature Tensile Properties of Ti-15Al-33Nb and Ti-21Al-29Nb Microstructures……..39

Table X. 650°C Tensile Properties of Ti-15Al-33Nb and Ti-21Al-29Nb Microstructures……..43

Table XI. Difference In Tensile Properties at 650°C Compared to Room Temperature……43

Table XII. Measured Steady State Strain Rates and Grain Size for Subtransus Heat-Treated Ti-15Al-33Nb Microstructures……..48

Table XIII. Measured Steady State Strain Rates and Grain Size for Supertransus Heat-Treated Ti-15Al-33Nb Microstructures……..49

Table XIV. Measured Steady State Strain Rates and Grain Size for Heat-Treated Ti-21Al-29Nb Microstructures……50

Table XV. Measured Creep Exponents and Apparent Activation Energies for Ti-15Al-33Nb and Ti-21Al-29Nb Heat-Treated Microstructures……50

Table XVI. RT Tensile Properties of O + BCC Ti-Al-Nb Alloys……66

Table XVII. Comparison of Creep Parameters for α, α_2 and O-based Ti-Alloys……75

Table A-I. Activation Energy Range Determined for Creep-Tested Samples……98

Table A-II. Activation Energy Range Determined for BCC Grain Growth……98

LIST OF FIGURES

Page

Figure 1. Crystal structures of the constituent phases: (a) four bcc unit cells with an O unit cell inlaid depicting the orientation relationship (OR) between the O and BCC structures, (b) the α_2 unit cell, and (c) the O unit cell……3

Figure 2. The similarities between the α_2 phase and the O phase are shown oriented perpendicular to the c-axis at the basal planes……..4

Figure 3. Pseudobinary diagram based on TiAl and TiNb, for Ti = 50 at%, with differing ratios of Al:Nb……..5

Figure 4. Schematic illustrating the creep stress exponent (n) values for the diffusion and dislocation controlled creep regimes for pure metals……10

Figure 5. The as-forged Ti-17Al-33Nb and Ti-22Al-28Nb ingots……..…..14

Figure 6. An as-processed Ti-22Al-28Nb sheet……...14

Figure 7. SEM images of the as processed microstructures: (a) Ti-17Al-33Nb, (b) Ti-22Al-28Nb……15

Figure 8. Schematic depicting the heat treatment schedule for a HT:1005 aged sample……16

Figure 9. The ATS 2710 creep frame used in this study……...21

Figure 10. DTA curve for Ti-15Al-33Nb powder specimen……...23

Figure 11. DTA curve for Ti-21Al-29Nb powder specimen……...24

Figure 12. Ti-15Al-33Nb solutionized and water-quenched microstructures: (a) 855°C, (b) 910°C, (c) 960°C, (d) 990°C, (e) 1005°C, (f) 1050°C, (g) 1075°C, and (h) 1105°C……26

Figure 13. Ti-21Al-29Nb solutionized and water-quenched microstructures: (a) 855°C, (b) 910°C, (c) 960°C, (d) 990°C, (e) 1005°C, (f) 1050°C, (g) 1075°C, and (h) 1105°C……27

Figure 14. Photomicrographs of heat-treated microstructures: (a) Ti-15Al-33Nb HT:960°C, (b) Ti-21Al-29Nb HT:960°C, (c) Ti-15Al-33Nb HT:1005°C, (d) Ti-21Al-29Nb HT:1005°C, (e) Ti-15Al-33Nb HT:650°C, and (f) Ti-15Al-33Nb HT:1105°C……28

Figure 15. Orthorhombic volume fraction versus solutionizing temperature for both alloys……30

Figure 16. Grain size versus solutionizing temperature for both alloys……..31

Figure 17. Intensity versus 2θ XRD patterns for all Ti-15Al-33Nb solution-treated samples…….33

Figure 18. Intensity versus 2θ XRD patterns for all Ti-21Al-29Nb solution-treated samples…….34

Figure 19. High-resolution scans between 60-65° 2θ for (a) Ti-15Al-33Nb, (b) Ti-16Al-33Nb, and (c) Ti-21Al-29Nb…….35

Figure 20. BCC-phase grain growth kinetics for Ti-15Al-33Nb and Ti-21Al-29Nb samples heat-treated at different temperatures above the β-transus temperature followed by water-quenching……37

Figure 21. Room temperature tensile behavior of Ti-15Al-33Nb and Ti-21Al-29Nb microstructures……...38

Figure 22. Photomicrographs of RT tensile fracture surfaces: (a) Ti-15Al-33Nb AP, (b) Ti-21Al-29Nb AP, (c) Ti-15Al-33Nb HT:960, (d) Ti-21Al29Nb HT:960, (e) Ti-15Al-33Nb HT:1005, (f) Ti-21Al-29Nb HT:1005, (g) Ti-15Al-33Nb HT:650, and (f) Ti-15Al-33Nb HT:1105……41

Figure 23. 650°C tensile behavior of Ti-15Al-33Nb and Ti-21Al-29Nb microstructures……...44

Figure 24. Photomicrographs of 650°C tensile fracture surfaces:
(a) Ti-15Al-33Nb AP, (b) Ti-21Al-29Nb AP,
(c) Ti-15Al-33Nb HT:960, (d) Ti-21Al-29Nb HT:960,
(e) Ti-15Al-33Nb HT:1005, (f) Ti-21Al-29Nb HT:1005,
(g) Ti-15Al-33Nb HT:650, and
(f) Ti-15Al-33Nb HT:1105……45

Figure 25. Creep strain versus time data obtained from a Ti-15Al-33Nb HT:1105 sample during a load-jump experiment……..46

Figure 26. Creep strain versus time data obtained from a Ti-15Al-33Nb HT:1105 sample during a temperature-jump experiment……..47

Figure 27. Plot of log $\dot{\varepsilon}_{ss}$ versus log σ for Ti-15Al-33Nb creep tested microstructures at T = 650°C…….51

Figure 28. Plot of log $\dot{\varepsilon}_{ss}$ versus log σ for Ti-21Al-29Nb creep tested microstructures at T = 650°C…….52

Figure 29. Plot of log $\dot{\varepsilon}_{ss}$ versus log σ for all microstructures creep tested in this study at T = 650°C……..53

Figure 30. Activation Energies determined at σ = 50 MPa……..54

Figure 31. Activation Energies determined at σ = 150 MPa……...55

Figure 32. Activation Energies determined at σ = 275 MPa……...56

Figure 33. Plot of log $\dot{\varepsilon}_{ss}$ versus log σ for the Ti-15Al-33Nb HT:960 microstructure tested at 650°C and 710°C…….59

Figure 34. Pseudobinary diagram based on TiAl and TiNb, for Ti = 50 at%…….61

Figure 35. Pseudobinary phase diagram constructed in this study…….…….62

Figure 36. A Ti-21Al-29Nb HT:960/3h/WQ microstructure…….…….64

Figure 37. RT stress versus strain curves for Ti-12Al-38Nb and Ti-15Al-33Nb microstructures……...69

Figure 38. RT stress versus strain curves for Ti-21Al-29Nb and Ti-25Al-24Nb microstructures……...69

Figure 39. Yield strength versus temperature comparisons for Ti-Al-Nb alloys……..70

Figure 40. Creep strain versus time for microstructures initially loaded at σ = 172 MPa and T = 650°C……..73

Figure 41. The log $\dot{\varepsilon}_{ss}$ versus log σ behavior of the most creep resistant Ti-Al-Nb alloys……..76

Figure 42. Deformation map including data from this study……..78

Figure A-1. AP Ti-15Al-33Nb XRD pattern…….89

Figure A-2. AP Ti-21Al-29Nb XRD pattern…….89

Figure A-3. Ti-15Al-33Nb HT:855°C/3h/WQ XRD pattern……90

Figure A-4. Ti-21Al-29Nb HT:855°C/3h/WQ XRD pattern……90

Figure A-5. Ti-15Al-33Nb HT:910°C/3h/WQ XRD pattern……91

Figure A-6. Ti-21Al-29Nb HT:910°C/3h/WQ XRD pattern……91

Figure A-7. Ti-15Al-33Nb HT:960°C/3h/WQ XRD pattern……92

Figure A-8. Ti-21Al-29Nb HT:960°C/3h/WQ XRD pattern……92

Figure A-9. Ti-15Al-33Nb HT:990°C/3h/WQ XRD pattern……93

Figure A-10. Ti-21Al-29Nb HT:990°C/3h/WQ XRD pattern……93

Figure A-11. Ti-15Al-33Nb HT:1005°C/3h/WQ XRD pattern……..94

Figure A-12. Ti-21Al-29Nb HT:1005°C/3h/WQ XRD pattern……..94

Figure A-13. Ti-15Al-33Nb HT:1050°C/3h/WQ XRD pattern……..95

Figure A-14. Ti-21Al-29Nb HT:1050°C/3h/WQ XRD pattern……..95

Figure A-15. Ti-15Al-33Nb HT:1075°C/3h/WQ XRD pattern……..96

Figure A-16. Ti-21Al-29Nb HT:1075°C/3h/WQ XRD pattern……..96

Figure A-17. Ti-15Al-33Nb HT:1105°C/3h/WQ XRD pattern……..97

Figure A-18. Ti-21Al-29Nb HT:1105°C/3h/WQ XRD pattern……..97

Figure A-19. Ti-16Al-33Nb HT:1105°C/3h/WQ XRD pattern……..98

ABSTRACT

This work comprises a study of the physical metallurgy of two titanium-aluminum-niobium (Ti-Al-Nb) alloys, Ti-15Al-33Nb and Ti-21Al-29Nb. In particular, the microstructural evolution, tensile, and creep behavior were characterized in detail in order to determine processing-microstructure-property relationships.

Monolithic sheet material was produced through conventional thermomechanical processing. The processing for both alloys was performed at subtransus temperatures, which produced fine-grained microstructures and allowed for the control of microstructural features through post-processing heat treatment.

These alloys were found to posses four constituent phases: the intermetallic orthorhombic O phase, the intermetallic HCP α_2 phase, the ordered intermetallic BCC B2 phase, and the disordered BCC β phase. Grain size and phase volume fractions were quantified for each microstructure produced and phase field ranges were determined. Widmanstatten precipitation of the α_2 and O phases from the parent BCC phase was the only phase transformation mechanism observed. The pseudobinary phase diagram based on TiAl and TiNb, for Ti = 50 at%, was modified according to the findings of this study.

The tensile properties of the alloys were determined at room temperature and 650°C. All microstructures displayed a loss in yield strength and a gain in ductility at 650°C. The BCC phase is an essential microstructural requirement for these alloys to possess adequate room temperature ductility.

The creep behavior was studied for stresses between 50-275 MPa and temperatures between 650-710°C. Deformation mechanisms were proposed based on calculated creep stress exponents and apparent activation energies. The suggested deformation mechanisms were highly dependent on stress and temperature. Coble creep, grain boundary sliding, and dislocation climb were the deformation mechanisms proposed to be active for the stress and temperature range studied. Grain size was determined to be the most important microstructural feature influencing the secondary creep behavior of these alloys.

I. INTRODUCTION AND BACKGROUND

A. General Titanium Background

After the Second World War, titanium-based alloys gained consideration as key components for aircraft engines. Today, the aerospace industry is still the prime consumer of titanium and its alloys, but titanium is beginning to gain increased acceptance in architecture, chemical processing, medicine, power generation, transportation, marine and offshore, and sports and leisure markets. The reason titanium alloys stand out as prime candidates for these applications is due to two properties: high specific strength and excellent corrosion resistance.[1]

Titanium is an allotropic element, meaning that it can exist in more than one type of crystal structure. The two crystal structures that pure titanium exists in are the hexagonal close-packed structure (HCP), referred to as α, and the body-centered cubic structure (BCC), referred to as β. At high temperatures β-titanium is the stable phase and at lower temperatures α-titanium is the stable phase. The temperature above which a titanium alloy is completely BCC is referred to as the beta-transus temperature (β-transus), and for pure titanium this transformation occurs at $882 \pm 2°C$.[1]

Titanium alloys are classified as either α alloys, β alloys, or $\alpha+\beta$ alloys and can be further divided into near-α and metastable β alloys. The amount and type of alloying elements determine what type of alloy a particular titanium alloy is classified as. Elements such as carbon, oxygen, nitrogen, and aluminum stabilize the α phase and raise the β-transus temperature. Chromium, nickel, molybdenum, and niobium are β stabilizers and therefore lower the β-transus temperature. The α alloys are generally categorized by good strength, toughness, creep resistance, and weldability. These types of alloys cannot be strengthened by heat treatment, but can be used for cryogenic temperature applications due to the absence of a ductile-to-brittle transition. The β alloys are characterized by high hardenability and forgeability, and are unfortunately susceptible to a ductile-to-brittle transition due to the BCC structure. In the solution-treated condition, these alloys have good ductility, toughness, excellent formability, and can be age hardened.[2(pp.706-18)]

B. Orthorhombic Titanium-Aluminides

The two alloys that comprise this work, Ti-15Al-33Nb and Ti-21Al-29Nb (both compositions are in atomic percent, and henceforth all compositions will be reported in atomic percent unless otherwise stated), differ from conventional titanium alloys in that they contain an orthorhombic (O) intermetallic phase based on the composition Ti_2AlNb. This phase was first discovered in a Ti-25Al-12.5Nb alloy using Transmission Electron Microscopy (TEM), convergent beam electron diffraction (CBED), and channeling enhanced microanalysis.[3] The atomic coordinates of the Ti, Al, and Nb atoms in the O structure were later determined using neutron diffraction.[4]

1. Constituent Phases and Crystal Structures

These Ti-Al-Nb alloys can posses up to 4 constituent phases: α_2, β, B2, and O. The α_2 phase is an intermetallic HCP phase based on the composition Ti_3Al with DO_{19} symmetry, in Pearson notation. As previously mentioned, the O phase is an intermetallic phase based on the composition Ti_2AlNb. This phase has cmcm orthorhombic symmetry, in Hermann-Maguin notation. The BCC phase can be either B2 or β, depending on alloy composition. The B2 phase is an ordered intermetallic phase based on the CsCl crystal structure and the Ti_2AlNb composition. The β phase is a disordered BCC phase that is typically depleted in Al and enriched in Nb. The crystal structures of the constituent phases are presented in Figure 1. From Figure 1 (a) it can be seen that the (100) faces of the O unit cell are derived from the (110) planes of the bcc unit cell. Figure 2 shows the similarities between the O phase and the α_2 phase. These phases differ from each other by their arrangement of Ti and Nb atoms.

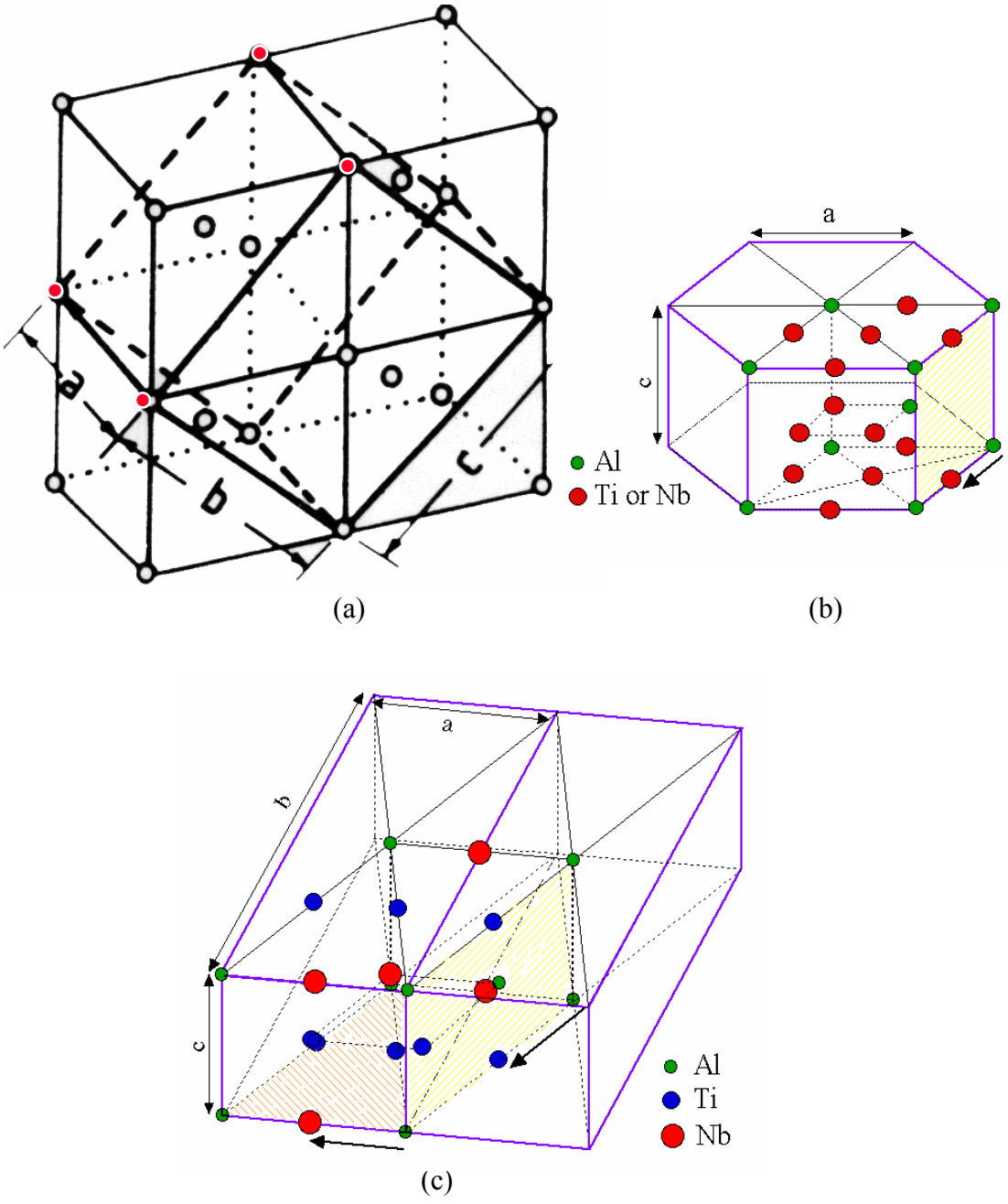

Figure 1. Crystal structures of the constituent phases: (a) four BCC unit cells with an O unit cell inlaid depicting the orientation relationship (OR) between the O and BCC structures,[3] (b) the α_2 unit cell, and (c) the O unit cell.[4,5]

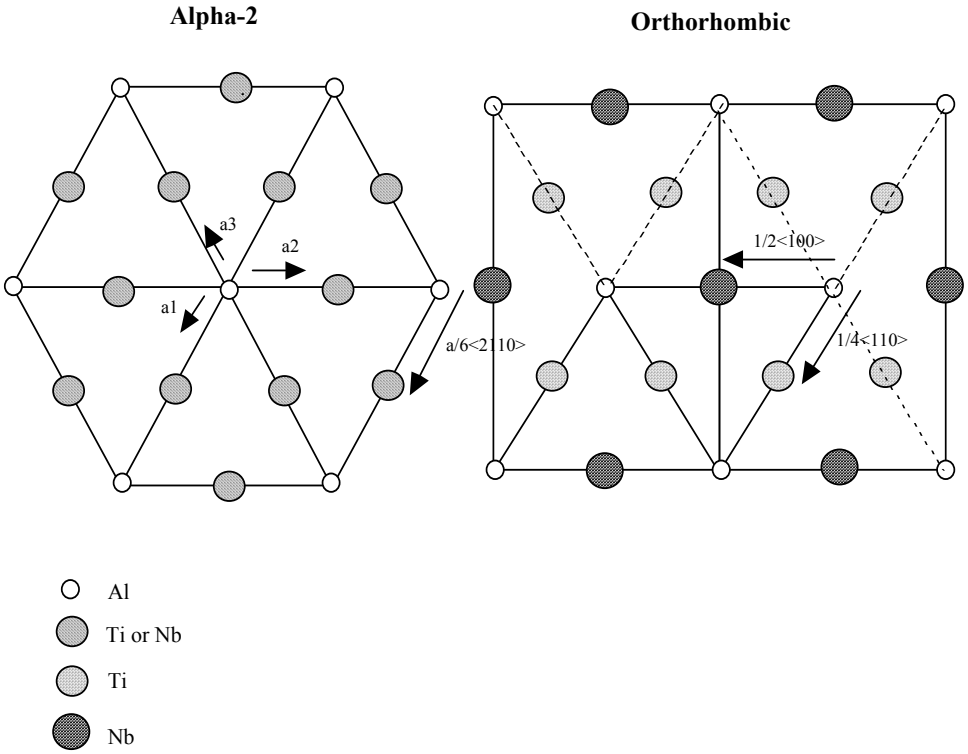

Figure 2. The similarities between the α_2 phase and the O phase are shown oriented perpendicular to the c-axis at the basal planes.

In particular, the ordered arrangement of Nb atoms in the O phase destroys the hexagonal symmetry present in the α_2 phase. The combination of these phases gives rise to interesting mechanical properties, and the amount, type, and morphology of the phases present in the microstructures of these alloys control the mechanical behavior.

2. Phase Equilibria

Since the discovery of the O phase, numerous studies have been performed on the phase equilibria of the O phase.[5-11] Since the alloys in this work were processed at subtransus temperatures, which significantly influences the range of microstructures that can be produced through post processing heat treatment, an example of previously determined phase equilibria will be given for subtransus processed Ti-23Al-27Nb, Ti-25Al-24Nb, and Ti-25Al-23Nb alloys.[12] Solution treatments followed by water quenching for these alloys above the B2 transus lead to fully-B2 microstructures. When

solution treated and water-quenched at temperatures between 1000°C and the B2 transus, α_2+B2 microstructures result. A narrow three phase O+B2+α_2 regime lies below the α_2+B2 phase field for the temperature range of 975-1000°C. The O+B2 phase field for these alloys occurred in the temperature range of 875-975°C. Three important microstructural observations were made from this phase equilibria study. First, fine grained equiaxed microstructures are only obtainable when hot working is performed below the β-transus temperature. Second, lower temperature solutionizing (but still above 875°C) leads to larger O grains at the expense of B2 grain size, and vice-versa for increasing temperatures. Third, a fully lenticular O+B2 microstructure was observed in the Ti-25Al-24Nb alloy when the fully equiaxed O microstructure of this alloy was resolutionized at 900°C and water-quenched. The pseudobinary phase diagram first constructed by Bendersky *et al.*[10] and modified due to the work in the above mentioned phase evolution study is depicted in Figure 3.

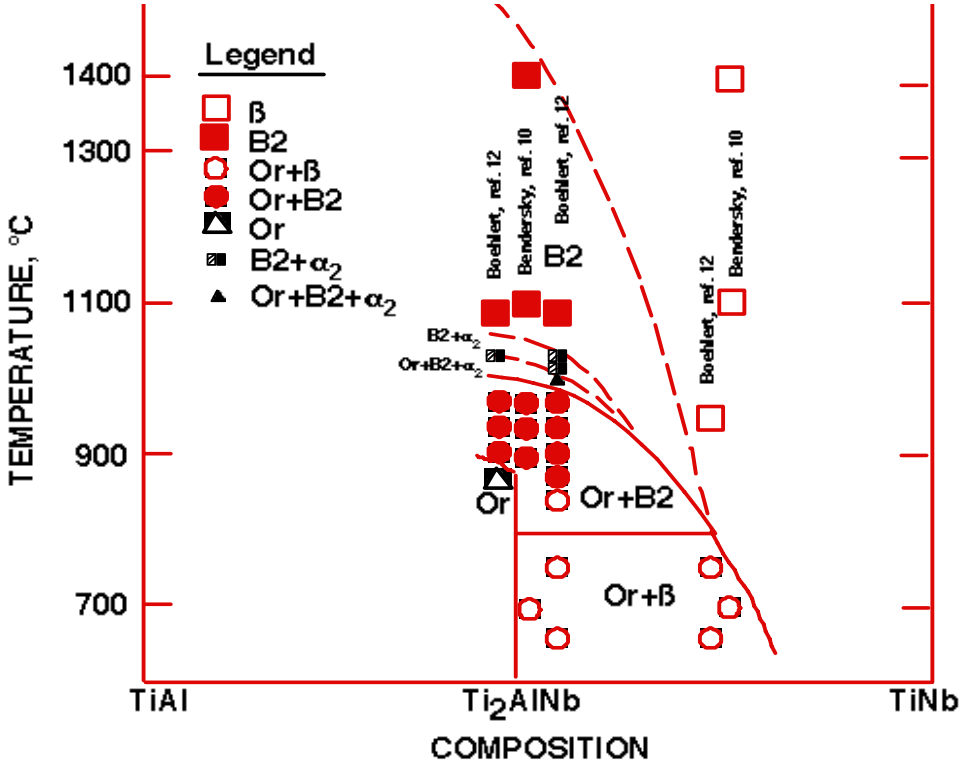

Figure 3. Pseudobinary diagram based on TiAl and TiNb, for Ti = 50 at%, with differing ratios of Al:Nb, first developed by Bendersky *et al.*[10] and further modified by Boehlert *et al.*[12].

From Figure 3 it is evident that this phase diagram is lacking in information between the compositions of Ti-23Al-27Nb and Ti-12Al-38Nb. The goal of the microstructural evolution study of this work was three-fold.

1. To quantify microstructural features such as grain size, phase volume fractions, and phase morphology then relate these features to mechanical properties and deformation behavior.
2. To determine phase equilibria, and further modify the pseudobinary phase diagram presented in Figure 3 for lower Al and higher Nb containing alloys.
3. To determine phase transformation mechanisms that occur in these alloys.

3. Mechanical Properties

Ti-Al-Nb alloys based on the Ti_2AlNb composition have an attractive balance of mechanical properties that can be optimized through changes in composition and processing parameters. In particular, increasing the Nb content is beneficial to strength, ductility, fracture toughness, and creep resistance. Increasing the Al content can improve the creep resistance, but reduce the workability of Ti_2AlNb based alloys, and it can significantly deteriorate the ductility and fracture toughness.[13] A major disadvantage of increasing the Nb content in Ti-Al-Nb alloys is increasing the density, due to the molecular weight of niobium being 92.91 g/mol.

a. Tensile Properties

The tensile properties of Ti-Al-Nb alloys are highly dependent on microstructure, which arises due to the constituent phases present in these microstructures and their inherent deformation characteristics. The least ductile of the constituent phases is the HCP α_2 phase, due to the inherently low number of available slip systems in this microstructure at both ambient and elevated temperature. Slip in hexagonal metals occurs on the {0001} planes in the <11-20> directions. This yields a total of 3 slip systems per unit cell.[2(p. 143)] This is contrary to von Mises Criterion, which states that five

independent slip systems are necessary to allow for deformation accommodation at grain boundaries.[14] It has been discovered that adjacent α_2/α_2 grain boundaries provide preferential crack initiation sites which lead to failure and are detrimental to both strength and ductility.[15,16] Therefore, to produce microstructures with adequate ductility, the α_2 phase is undesirable, especially when α_2 grains are adjacent to one another.

Although the α_2 and O phase structures are similar, they exhibit different deformation characteristics. This was shown in a study comparing the deformation behavior of an O based Ti-26Al-21Nb alloy and an α_2 based Ti-27Al-10Nb alloy.[17] All possible <c+a> slip systems were active in the O alloy and not in the α_2 alloy. Thus it was suggested that the O phase possesses a lower critical resolved shear stress, which allows more dislocation motion at lower applied stresses, and therefore increases ductility. The O phase structure also allows for cross-slip of screw dislocations, and the frequency with which cross-slip occurs was observed to increase with increasing temperature.[17]

The BCC structure is characterized by four close-packed directions, the <111> directions, and the lack of a truly close-packed plane such as the octahedral plane of the face-centered cubic (FCC) lattice or the basal plane of the HCP lattice. Slip in BCC metals occurs in the <111> directions, however the slip plane is not well defined. The {110}, {112}, and {123} planes have all been identified as slip planes in BCC crystals, which yields nearly 48 equivalent slip systems.[2(pp.145-6)] The B2 and β phases will inherently provide ductility to this intermetallic system due their large number of available slip systems.

Surface slip observations, using samples that were metallographically polished prior to tensile testing have provided much insight into the deformation behavior of Ti-Al-Nb alloys. Planar slip has been observed in the O and α_2 phases and wavy slip has been observed in the B2 phase.[17,18,19] Slip has been shown to be transmittable between adjacent O and B2 grains, which reduces stress concentration effects that induce cracking.[18] Thus, due to its wavy slip character and crack blunting capabilities, the BCC phase is an essential requirement for ductility in this intermetallic system.

By varying the amount and types of phases present in the Ti-Al-Nb system through alloying and heat treatment, a wide range of tensile properties can be acquired.

Three examples of the range in tensile properties and their dependence on microstructure are given in Table I.[20]

Table I. Microstructural Influence on Tensile Properties of Ti-Al-Nb alloys

Alloy and Heat Treatment	YS, MPa	UTS, MPa	ε_f, %	E, GPa	O Vp	β Vp	B2 Vp
Ti-12Al-38Nb 650°C/55h/WQ	809	869	12.3	89	28 platelet	72	0
Ti-23A-27Nb 950°C/24h/WQ	n/a	572	0.5	126	45 equiaxed	0	55
Ti-25Al-24Nb 875°C/100h/WQ	694	704	1	137	100 equiaxed	0	0
Ti-26Al-27Nb As-Processed	789	860	>5.9	73	0	0	100

n/a indicates the 0.2% proportional requirement for yield strength was not met
Vp is the phase volume percent

The goal of the tensile behavior portion of this thesis was to determine the tensile properties of these alloys at room temperature (RT) and elevated temperature (ET), and to determine microstructure-tensile property relationships and the effect of temperature on these relationships.

b. Creep Properties

As with the tensile properties of Ti-Al-Nb alloys, the creep properties are also highly dependent on microstructure, which arises due to the constituent phases present in these microstructures and their inherent deformation characteristics.

In Ti-25Al-17Nb and Ti-22Al-23Nb alloys it was found that increasing the O phase volume percent and decreasing the α_2 volume percent increased creep resistance, neglecting possible tension/compression testing effects, stress levels, and morphology.[18,21] Grain size (d) is an important factor influencing the secondary creep rates. For Coble creep the steady state strain rate is proportional to d^{-3} while for Nabarro-Herring creep it is proportional to d^{-2}.[22] When deforming by Coble creep, grain size will be more influential on the secondary creep rate for Ti-Al-Nb alloys. Morphology effects also play a role as the O phase typically has a lath morphology and the α_2 phase is typically equiaxed.[23-27] BCC phase volume percent also plays a role, because this phase

will transform to the O phase at projected application temperatures (see Figure 3). The BCC phase also has a higher diffusivity, which leads to lower creep resistance, than the α_2 and O phases due to its less densely packed structure. At 1000°C the self-diffusion coefficient in α-Ti is ~10^{-15} m^2/s while in β-Ti the self-diffusion coefficient is 10^{-13} m^2/s.[1] In addition the ordered B2 structure will provide better creep resistance than the disordered β phase due to its ordered arrangement of atoms, which decreases diffusivity.

The focus of the creep behavior study of this thesis was to determine the deformation mechanisms controlling the secondary creep behavior of these Ti-Al-Nb alloys. The values of creep stress exponents (n) and apparent activation energies (Qapp) give insight into the deformation mechanisms that occur during the secondary stage of creep. These parameters were calculated from the following equation for minimum creep rate:

$$\dot{\varepsilon}_{ss} = B\sigma^n \exp(-Qapp/RT) \qquad (1)$$

where B is a constant, σ is the applied stress, n is the creep stress exponent, Qapp is the apparent activation energy, R is the gas constant, and T is the absolute creep temperature. The n values were determined by applying a power law curve fit to the plot of log $\dot{\varepsilon}_{ss}$ versus log σ and the Qapp values were determined from the slope of the least squares linear curve fit to the plot of ln $\dot{\varepsilon}_{min}$ versus 1/T. The n and Qapp values determined were used to predict the active secondary-creep deformation mechanisms.

Based on creep theories for pure metals, n values close to unity suggest that stress directed atomic diffusion of vacancies as the deformation mechanism.[28] Nabarro-Herring (N-H) creep deformation occurs by diffusion of vacancies through the lattice, i.e. lattice bulk diffusion.[29] Coble creep deformation occurs by diffusion of vacancies along grain boundaries.[30] Activation energies determined when N-H creep deformation is active are typically close to those for lattice bulk diffusion. When Coble creep is the dominant deformation mechanism, activation energies are typically 0.5-0.6 of those for lattice bulk diffusion. Grain boundary sliding can be the active deformation mechanism, which is accommodated by diffusional creep at high temperatures and the glide and climb of dislocations at low temperatures and high stresses.[31] Grain boundary sliding deformation can have activation energies within the range associated for either grain boundary

diffusion or lattice bulk diffusion and n values between those for diffusion and dislocation controlled creep. For n values greater than or equal to 3.5, deformation typically occurs by a dislocation climb mechanism.[31] A dislocation climb mechanism typically has an activation energy associated with lattice bulk diffusion. Therefore, based on previous secondary creep theories of pure metals, by combining n and Qapp values the deformation mechanism at a particular stress range and temperature may be suggested. A change in n value typically corresponds with a change in deformation mechanism. Therefore, by determining n values over a range of stresses at a constant temperature, the stress ranges where particular deformation mechanisms are active at that temperature can be estimated. Figure 4 illustrates the dependence of n on applied stress. In several cases alloys have also exhibited similar secondary creep behavior as pure metals,[23-27,31] and therefore the secondary creep theories based on pure metals have been applied to alloys.

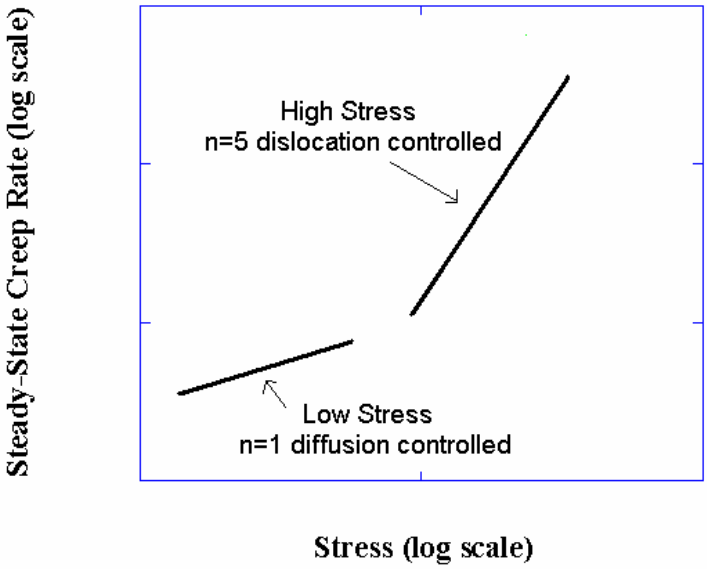

Figure 4. Schematic illustrating the creep stress exponent (n) values for the diffusion and dislocation controlled creep regimes for pure metals.

It is very important to note that n and Qapp values alone are not sufficient for conclusively verifying the exact deformation mechanism occurring. In order to state that grain boundary sliding is the dominant secondary creep deformation mechanism, surface observations of metallographically polished fiducially marked samples that have been

creep tested in a vacuum or inert environment is necessary. TEM observations of creep deformed microstructures is necessary in order to observe dislocation activity within the microstructures. Combining n and Qapp values with observed dislocation activity allows one to more confidently state the dominant secondary creep mechanism over an applied stress range at a given creep temperature. For example, if an n value of 1 and a relatively low Qapp value of approximately 125 kJ/mol were calculated, and a very low dislocation density was observed in a post creep-tested sample, then the combination of this data would provide strong evidence that Coble creep exists.

In this thesis, the n and Qapp values have been determined in an attempt to better estimate and understand the potential dominant secondary creep mechanisms active for these Ti-Al-Nb alloys. Microstructure-creep behavior relationships were also determined for Ti-15Al-33Nb and Ti-21Al-29Nb. TEM studies of dislocation activity in these microstructures and confirmation of grain boundary sliding deformation will constitute a large amount of future work that will be performed on these Ti-Al-Nb alloys.

II. OBJECTIVES

The objectives of this thesis were:

1. To understand phase evolution in the Ti-Al-Nb system and further develop the pseudobinary diagram based on TiAl and TiNb, for Ti = 50 at%
2. To understand processing-microstructure-property relationships of the Ti-Al-Nb system
3. To understand deformation mechanisms, in particular high temperature creep behavior as a function of stress, temperature, and strain rate
4. To understand what controls ductility in this intermetallic system
5. To identify the potential for two alloys that have yet to be rigorously evaluated- Ti-15Al-33Nb and Ti-21Al-29Nb

III. EXPERIMENTAL PROCEDURE

A. Processing

Titanium, aluminum, and niobium master alloys were mixed to produce nominally Ti-17Al-33Nb at% (Ti-7.7Al-51.8Nb wt%) and Ti-22Al-28Nb at% (Ti-10.8Al-48.5Nb wt%) compositions, and were cast into ingots by double vacuum arc remelting (VAR). The ingots were then unidirectionally hot forged to approximately 0.14 m wide × 0.7 cm thick × 0.58 m long (see Figure 5). Approximately 16 mm thick slabs were then cut from the transverse sections of the ingots and hot rolled to 1.65 mm thick by 70 mm wide sheets. The hot rolling eliminated cracking that occurred during forging, produced a reduction in area of 90%, and introduced a true shear strain on the order of 2. The Ti-17Al-33Nb sheets were forged and hot rolled at 899°C (1650°F) and the Ti-22Al-28Nb sheets were forged and hot rolled at 982°C (1800°F). After the hot rolling was complete, the sheets were annealed at their respective rolling temperatures for one hour and then air-cooled. A picture of an as-processed sheet is depicted in Figure 6. Photomicrographs of the as-processed microstructures are shown in Figure 7. All alloy processing was done by RMI Titanium, Inc, Niles Ohio.

B. Chemical Analysis of Rolled Sheets

The chemical composition of the Ti-17Al-33Nb and Ti-22Al-28Nb alloys was determined using Inductively Coupled Plasma Optical Emission Spectroscopy (ICP-OES) and Inert Gas Fluorescence (IGF). Titanium, aluminum, niobium, iron, chromium, molybdenum, nickel, silicon, and vanadium content were determined by ICP-OES and Hydrogen, oxygen, and nitrogen content were determined using IGF. The chemical analysis was also performed at RMI.

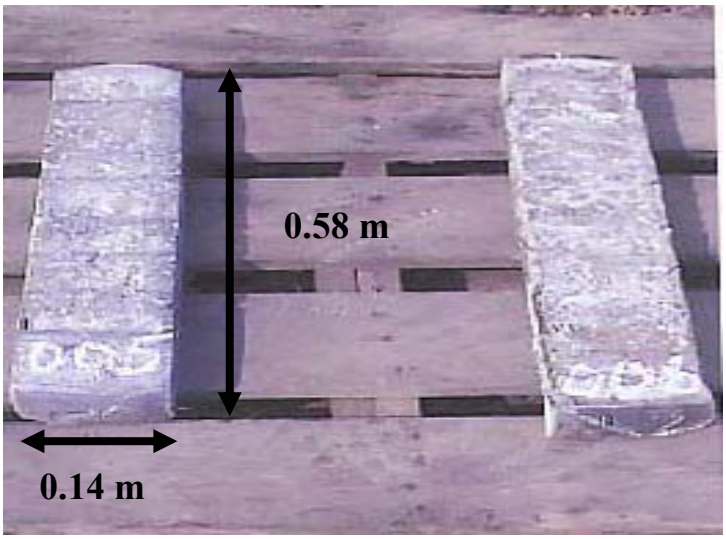

Figure 5. The as-forged Ti-17Al-33Nb and Ti-22Al-28Nb ingots. The ingot labeled 005 is Ti-17Al-33Nb and the ingot labeled 006 is Ti-22Al-28Nb. Note that Ti-22Al-28Nb exhibited more extensive cracking than Ti-17Al-33Nb.

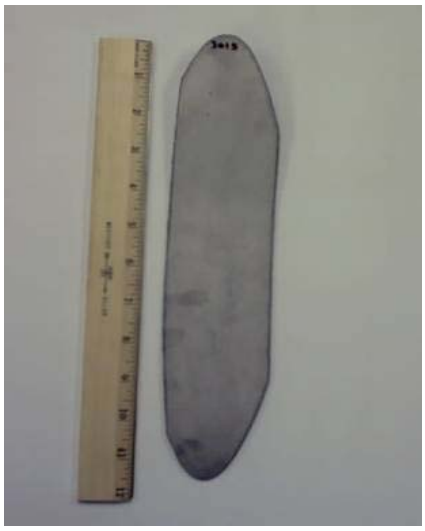

Figure 6. An as-processed Ti-22Al-28Nb sheet. Note the elimination of the cracking that occurred during forging.

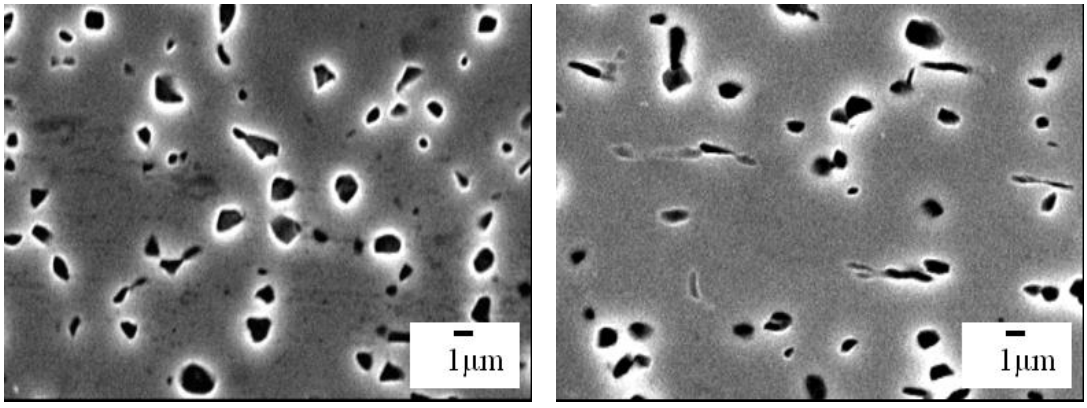

(a) (b)

Figure 7. SEM images of the as processed microstructures: (a) Ti-17Al-33Nb, (b) Ti-22Al-28Nb.

C. Microstructural Evaluation

1. Heat Treatments

Microstructures were produced for both alloys through solutionizing at either 960, 1005, or 1105°C for 10.8 ks (3 h) followed by furnace-cooling to 855°C then aging for 28.8 ks (8 h), control-cooling to 650°C and holding for 0.6 ks (0.17 h), then furnace-cooling to room temperature. Two additional aged microstructures were also produced for Ti-17Al-33Nb by solutionizing at 650°C for 360 ks (100 h) or 900 ks (250 h) followed by furnace cooling. Henceforth, all aged microstructures will be referred to by their solutionizing temperature: HT:650/100h, HT:650/250h, HT:960, HT:1005, and HT:1105. A schematic of the heat treatments using HT:1005 as an example is shown in Figure 8.

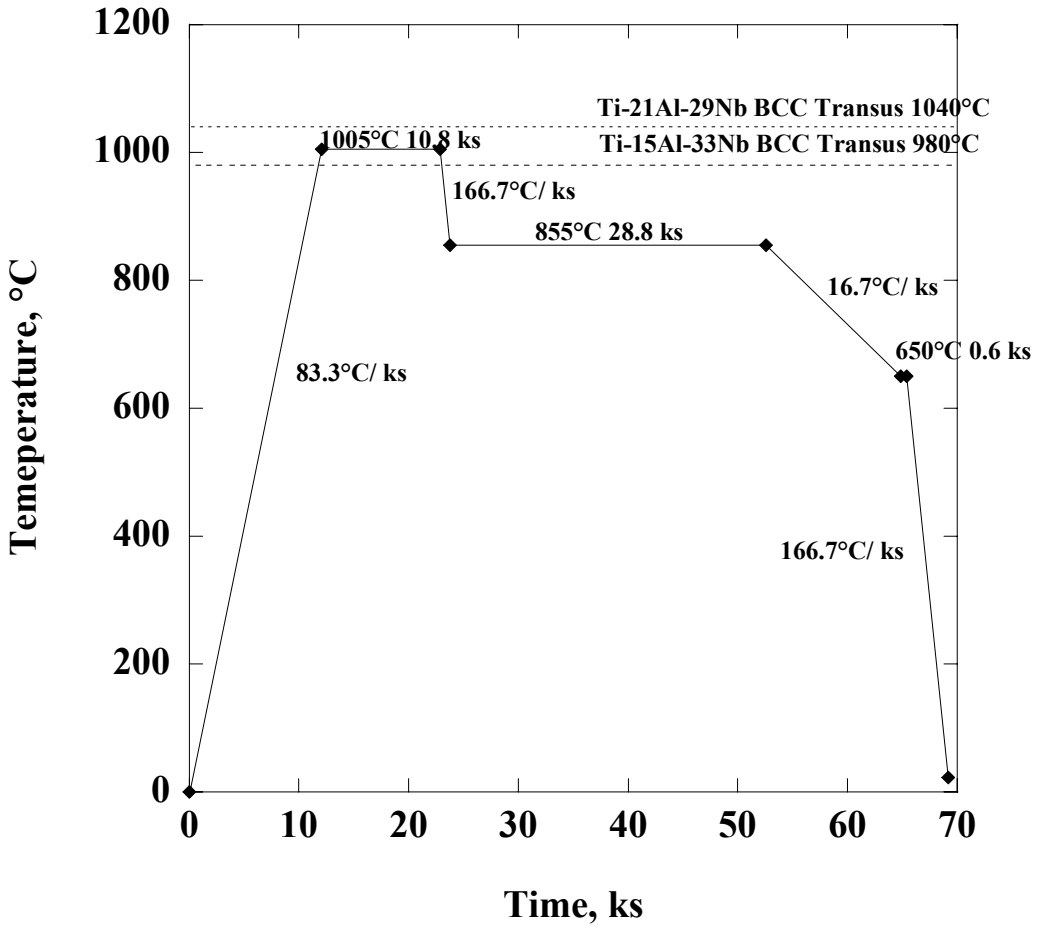

Figure 8. Schematic depicting the heat treatment schedule for a HT:1005 aged sample.

2. Sample Preparation and Metallography

Samples for the solution treatment study were cut from the three different sheet orientations (face (L-T), transverse (T), and longitudinal (L)) using either an abrasive saw with a SiC cutting blade or a low-speed saw using a diamond blade. The samples were then wrapped in tantalum foils and solutionized for three hours at the appropriate temperature followed by water-quenching. The heat-treated samples were then mounted in Konductomet™ for preparation for grinding and polishing. Grinding was accomplished by using successively finer grits of SiC paper. After grinding, the samples were polished using diamond paste, according to the following schedule: 15 μm for 0.3 ks (0.083 h), 6 μm for 0.3 ks (0.083 h), 1 μm for 1.2 ks (0.33 h). Colloidal silica with an

average particle size of 0.06 μm was used for the final polish, with polishing times ranging between 1.2 ks (0.33 h) greater than 3.6 ks (1 h).

3. Microstructures and Phase Volume Fraction Analysis

Optical Microscopy (OM) and Scanning Electron Microscopy (SEM) were both employed to evaluate the as-processed and heat-treated microstructures. High contrast, digitized, backscattered-electron (BSE) images, obtained using an AMRAY model 1810 SEM, an ETEC AUTOSCAN SEM, or a FEI Quanta 200 ESEM were used for volume fraction analysis of the BCC, O, and α_2 phases present. Approximately 20 BSE images were taken at different magnifications and from different areas of the face, transverse, and longitudinal sections of each sample. These images were then analyzed using NIH Image Analysis Software. This software allows area-fraction analysis of digitized images. This is performed by allowing the user to fill the regions of different contrast, which designate different phases in BSE images, and thereafter the software counts the number of pixels in the filled region and divides this number by the total number of pixels in the digitized image. By performing this analysis on several images from the different orientations of the rolled sheets, the average volume fraction of each phase can be determined.

4. Grain Size Analysis

Average equiaxed grain size was determined using the Mean Line Intercept Method[32] for subtransus heat-treated microstructures and ASTM Standard E112[33] for supertransus heat-treated microstructures. Samples were etched using a 75mL H_2O-20mL HF- 5mL HNO_3 etchant, which is a standard titanium etchant,[34] to reveal grain boundaries. For the subtransus heat-treated microstructures, at least six lines of known length were drawn on either optical micrographs or scanning electron micrographs and the number of grain boundary intercepts were counted for each line. The length of each line was then divided by the magnification and then divided by the number of grain boundary intercepts. This number was then multiplied by a factor of 1.74 to calculate average grain size. As with phase volume fraction determinations, several micrographs

were taken at different magnifications from different sheet orientations for the grain size calculations. It is important to note that this analysis was performed on solutionized and then water quenched samples, and thereby no lath grain boundaries were considered. Thus, the grain sizes reported are only those of the equiaxed grains present.

5. Differential Thermal Analysis (DTA)

DTA analysis was performed in order to determine the temperatures at which phase transformations were occurring at. Each alloy was ground into powder for the DTA analysis in order to provide more surface area for reactions to occur. Approximately 15 mg of the alloy powder was used, along with an equivalent amount of high purity aluminum oxide as the reference standard. The alloy powders and standard were heated in platinum crucibles. The thermal schedule included an equilibration at 600°C after which the samples were heated to 1200°C at a rate of 15°C/minute while temperature and temperature difference between the alloy powder and the reference standard were recorded. The phase transformations were revealed by noticeable exotherms or endotherms in the temperature difference versus temperature plots.

6. X-ray Diffraction (XRD)

XRD analysis was performed on the solution treatment samples using Siemens Diffractometers operating at 40kV and 30mA with Cu Kα radiation sources. Each scan was performed using a step size of 0.04° 2θ and a count time of 5 seconds for the solution treated samples. In addition, long count time scans were performed on selected samples using a step size of 0.02° 2θ and a count time of 30 seconds to determine whether the BCC phase of each alloy was ordered (B2) or disordered (β). The resulting Intensity versus 2θ plots revealed the phases present in the solution treated samples.

D. Tensile Testing

Flat, dogbone shaped samples (0.14 m long × 0.025 m wide with a 0.0127 m gage length) were machined from the rolled sheets using either a mill or an Electrodischarge Machine (EDM). The dogbones were then ground through a better than 240 grit finish to remove the oxide scale left from processing and any surface layers that may have been damaged during the machining process. Tensile tests were performed at both room temperature and 650°C using an Instron 8562 testing machine equipped with and Instron 8500 controller and a 100 kN load cell. Strain was measured with a 25.4 mm gage length Instron Extensometer attached to the gage section of each dogbone and all tests were conducted at a strain rate of 1.3×10^{-3} s^{-1}. For the elevated-temperature experiments, temperature was monitored in the same fashion as will be described for the creep tests, using the same types of furnaces, and each sample was soaked at 650°C for at least 30 minutes prior to tensile testing. The temperature was controlled within ± 5°C of the targeted test temperature. The test matrix for the tensile samples is shown in Table II. Yield Stress (0.2% offset method YS), Ultimate Tensile Stress (UTS), and Elongation-at-Failure (ε_f) values were recorded for each test. Young's Modulus (E-Mod) for each sample was determined from the slope of the elastic portion of the stress versus strain curves. The strength coefficient (K) and strain hardening exponent (n) were determined for samples that exhibited strain hardening behavior. This was accomplished by applying a power-law curve fit over the area of uniform plastic deformation of the respective stress versus strain curves.

Table II. Tensile Test Matrix

Alloy	Heat Treatment, °C	RT Tensile Tests	ET Tensile Tests
Ti-17Al-33Nb	AP	2	1
	HT:650/100h	3	1
	HT:960	2	2
	HT:1005	2	2
	HT:1105	2	1
Ti-22Al-28Nb	AP	1	2
	HT:960	1	1
	HT:1005	1	1

E. Creep Testing

Dogbone specimens used for creep testing were machined and prepared in the same manner as the tensile specimens. Constant load, tensile-creep experiments were performed on either of two Applied Test Systems, Inc. (ATS) creep frames (2410 or 2710 series) with 20:1 lever arm ratios (Figure 9). The loading direction was parallel to the rolling direction for all the creep and tensile experiments. The load was measured with a resolution of 0.01lbs using WSM 100lb (Model AB100-T) and 500lb (Model AB) load cells. Creep strain was monitored during the tests using a linear variable differential transformer (LVDT) that was connected to a 25.4 mm gage length ATS high-temperature extensometer. The extensometer was attached directly to the gage length of each sample. The resolution of the strain measuring capability of the LVDT was 0.0001. The strain rate resolution was estimated to be 2.8E-9 according to the resolution of the strain measurement technique. ATS single-zone shell furnaces (3320 series) equipped with $MoSi_2$ heating elements were used for the creep experiments. The temperature was monitored with three thermocouples for each test; one thermocouple was spot-welded directly to the gage section of the dogbone, while the other two were placed near the sample gage section but were not attached to the sample. For each test, the temperature was kept within ± 5°C of the targeted test temperature. All creep tests were conducted in air at stresses between 50-275 MPa and temperatures between 650-710°C. Each sample was soaked at the testing temperature for at least 60 minutes before loading. The steady-state strain rate was determined for each sample at each of the specific stresses and temperatures. In order to determine secondary creep stress exponents and activation energies, constant temperature/load jump tests and constant load/temperature jump tests were performed. Activation energy ranges were determined by taking into account the strain rate resolution and are available in the Appendix. This was accomplished by either changing the load or temperature after a steady state creep rate ($\dot{\varepsilon}_{ss}$) had been achieved. The load was increased by adding weights to the lever arm and temperature was controlled by increasing or decreasing the voltage output to the furnace. The creep sample test matrix is shown in Table III. Each sample in the creep test matrix involved a load and/or temperature jump experiment where creep data for more than one stress and/or temperature were obtained.

Table III. Creep Test Matrix

Alloy	Heat Treatment, °C	Creep Tests Performed
Ti-17Al-33Nb	HT:650/100h	1
Ti-17Al-33Nb	HT:650/250h	1
Ti-17Al-33Nb	HT:960	3
Ti-17Al-33Nb	HT:1005	4
Ti-17Al-33Nb	HT:1105	3
Ti-22Al-28Nb	HT:960	1
Ti-22Al-28Nb	HT:1005	2

Figure 9. The ATS 2710 creep frame used in this study.

IV. RESULTS

A. Microstructure Results

1. Chemical Composition of the As-Processed Sheets

Table IV and Table V depict the chemical composition of the as-processed Ti-17Al-33Nb and Ti-22Al-28Nb sheet material, respectively.

Table IV. Measured Chemical Composition of Ti-17Al-33Nb As-Processed Sheets

Ti-17Al-33Nb	ICP	IGF	ICP	IGF
Element	Weight %	Weight %	Atomic %	ppm
Ti	41.09		51.4	
Al	6.87		15.3	
Nb	51.66		33.3	
Cr	0.01			100
Fe	0.11			1100
Mo	<0.01			<100
Ni	0.01			100
Si	0.03			300
V	<0.01			<100
H		0.0012		12
O		0.11		1100
N		0.01		100

Table V. Measured Chemical Composition of Ti-22Al-28Nb As-Processed Sheets

Ti-22Al-28Nb	ICP	IGF	ICP	IGF
Element	Weight %	Weight %	Atomic %	ppm
Ti	42.78		50.7	
Al	9.82		20.6	
Nb	46.95		28.7	
Cr	<0.01			<100
Fe	0.2			2000
Mo	<0.01			<100
Ni	0.01			100
Si	0.07			700
V	0.01			100
H		0.0017		17
O		0.079		790
N		0.011		110

From Table IV and V it is apparent that these alloys more closely resemble Ti-15Al-33Nb at% and Ti-21Al-29Nb at% in composition; henceforth, both alloys will be referred to by these compositions. The oxygen content was 1100 ppm and 790 ppm for Ti-15Al-33Nb and Ti-21Al-29Nb, respectively. This is important because oxygen can occupy interstitial lattice sites which can be detrimental to mechanical properties, in particular ε_f. In addition oxygen raises the β-transus temperature, and stabilizes the α_2 phase, which is not desired in these alloys as it tends to lead to embrittlement.[35]

2. Differential Thermal Analysis

Figures 10 and 11 show the DTA curves for Ti-15Al-33Nb and Ti-21Al-29Nb, respectively.

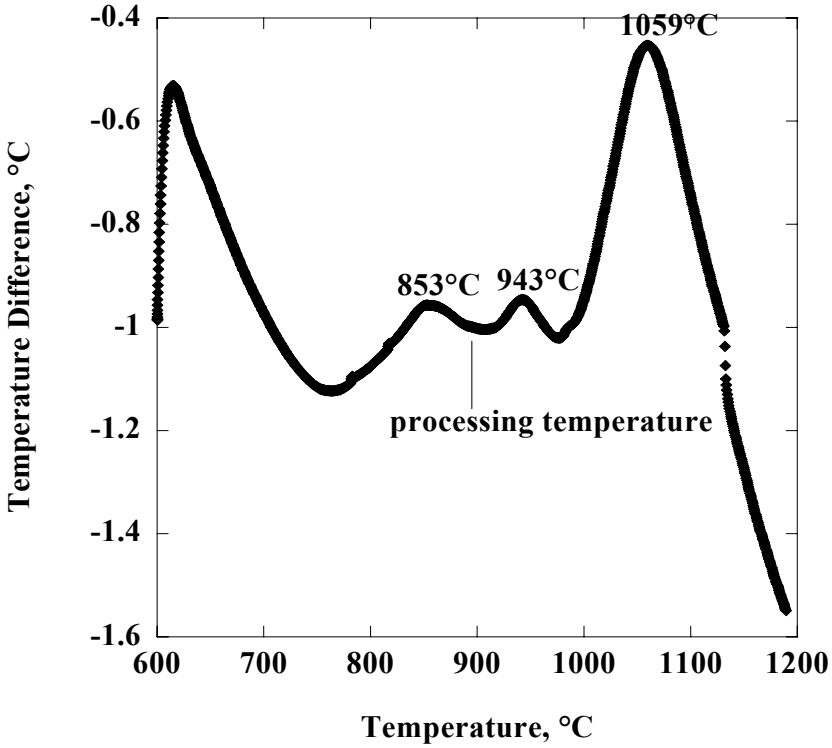

Figure 10. DTA curve for Ti-15Al-33Nb powder specimen. The sample was equilibrated at 600°C and heated to 1200°C at a rate of 15°C/min.

.

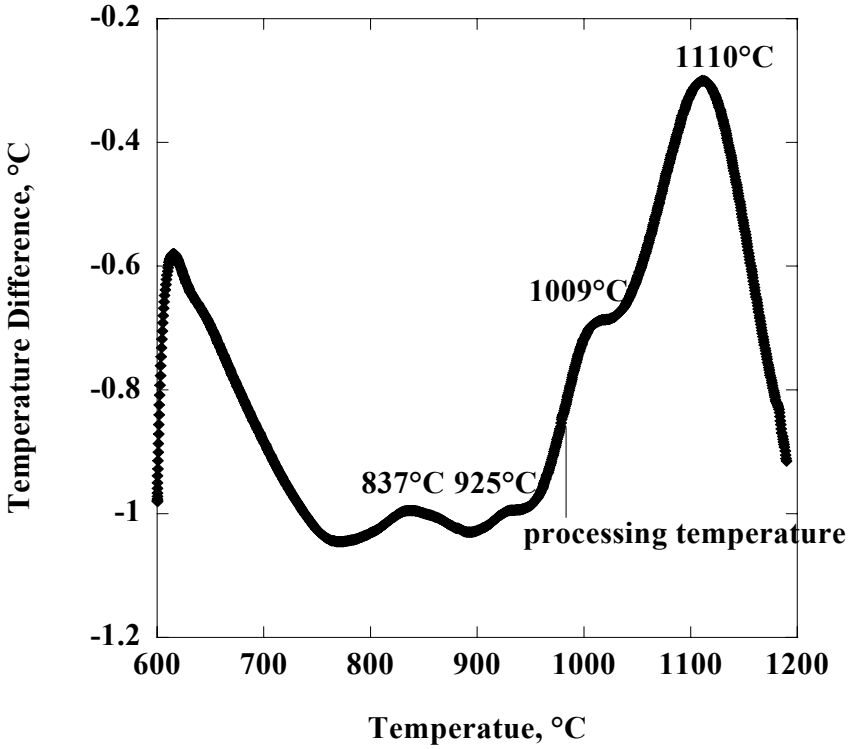

Figure 11. DTA curve for Ti-21Al-29Nb powder specimen. The sample was equilibrated at 600°C and heated to 1200°C at a rate of 15°C/min.

From Figure 10 it can qualitatively be stated that the three phase α_2+BCC+O regime lies between 853-943°C and the β-transus temperature lies between 943-1059°C for Ti-15Al-33Nb. For Ti-21Al-29Nb, the O+BCC regime lies between 837-925°C, the three phase α_2+BCC+O regime lies between 925-1009°C, and the β-transus occurs between 1009-1110°C. The temperature at which each alloy was processed is indicated on each DTA plot, which is clearly below the β-transus for each alloy.

3. Solution Treatment Study

The microstructures resulting from solutionizing at 855, 910, 960, 990, 1005, 1050, 1075, and 1105°C for 10.8 ks (3 h) followed by water-quenching are shown for Ti-15Al-33Nb and Ti-21Al-29Nb in Figure 12 and Figure 13, respectively. Microstructures developed through the heat treatments described in the experimental procedures, section C.1., are shown in Figure 14. In each BSE photomicrograph, the BCC phase appears as the lightest (white) colored phase, the α_2 phase appears as the darkest (black) colored phase, and the O phase is the medium (grey) colored phase. The BCC phase appears white because it is enriched in Nb, which is the highest molecular weight alloying element. The α_2 phase is enriched in Al (the lowest molecular weight alloying element) and depleted in Nb, and therefore appears black. Optical micrographs, some taken using the Differential Interference Contrast (DIC) mode, are shown for single phase, supertransus heat-treated microstructures. The optical micrographs were taken at much lower magnifications than the BSE micrographs in order to show the effect of heat treatment on grain size. For Ti-15Al-33Nb all microstructures are fully BCC starting at 990°C and above and for Ti-21Al-29Nb all microstructures are fully BCC starting at 1050°C. This yields the upper limit for the Ti-15Al-33Nb β-transus temperature being 990°C and the upper limit for the Ti-21Al-29Nb β-transus temperature being 1050°C.

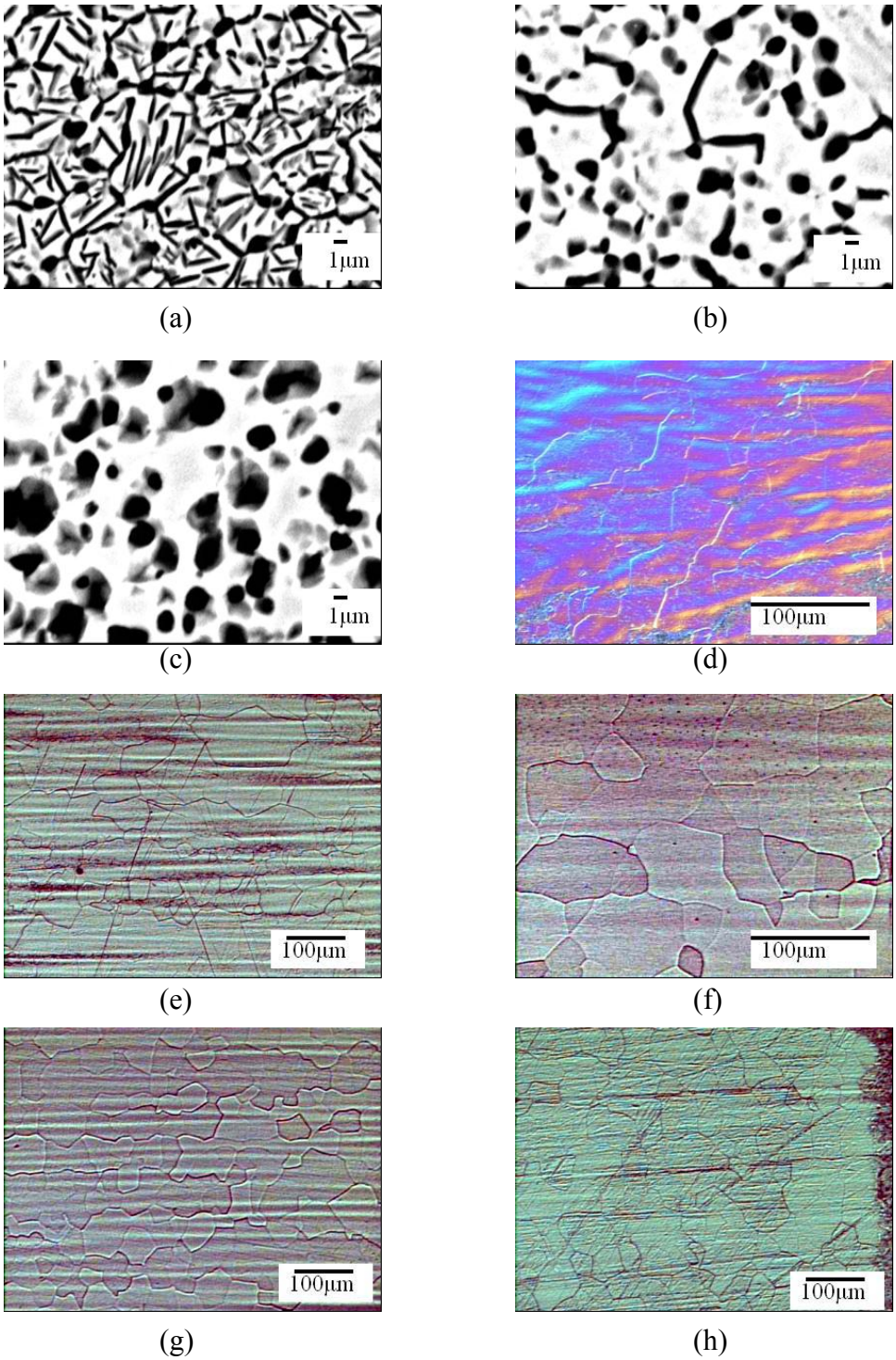

Figure 12. Ti-15Al-33Nb solutionized and water-quenched microstructures: (a) 855°C, (b) 910°C, (c) 960°C, (d) 990°C, (e) 1005°C, (f) 1050°C, (g) 1075°C, and (h) 1105°C.

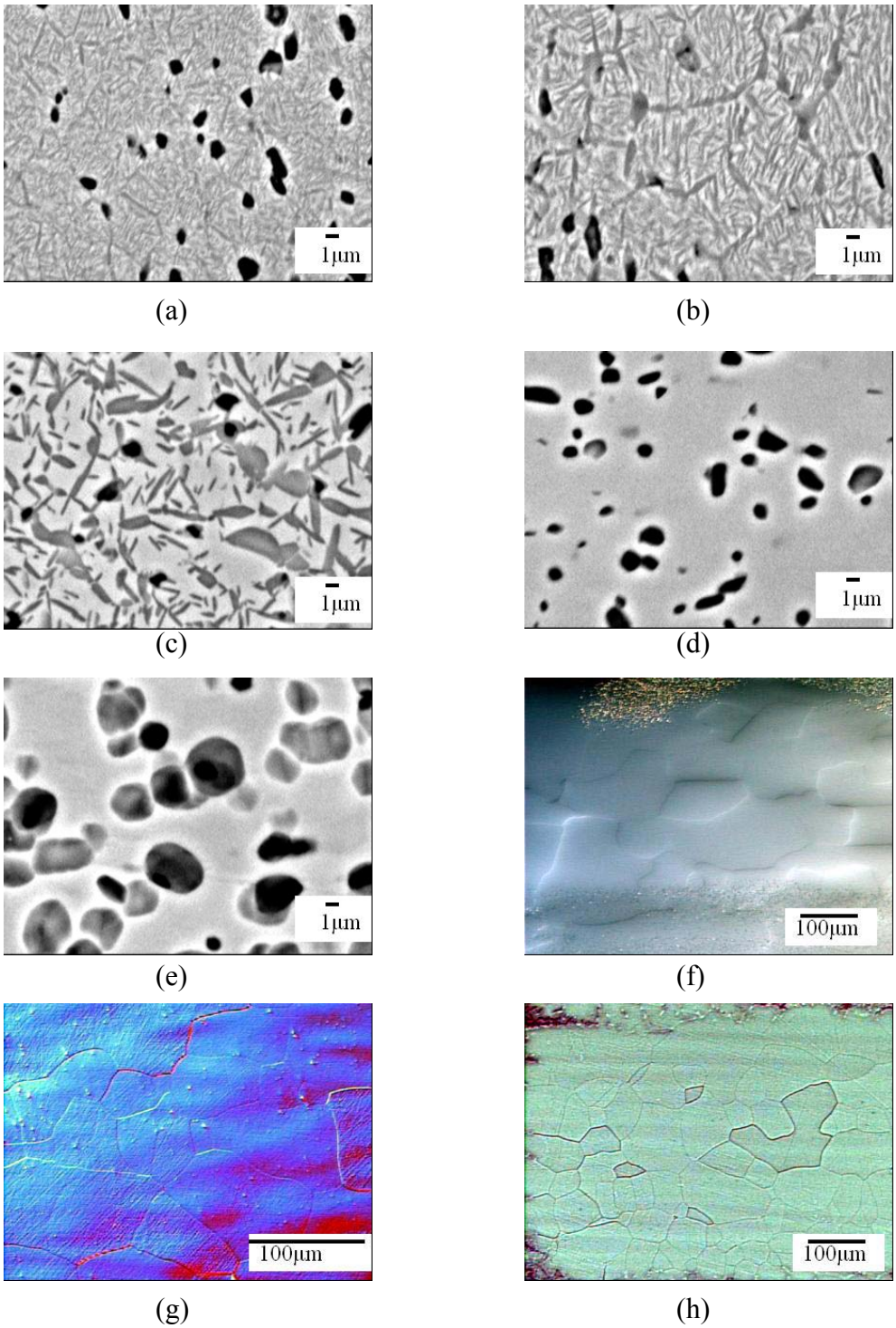

Figure 13. Ti-21Al-29Nb solutionized and water-quenched microstructures: (a) 855°C, (b) 910°C, (c) 960°C, (d) 990°C, (e) 1005°C, (f) 1050°C, (g) 1075°C, and (h) 1105°C.

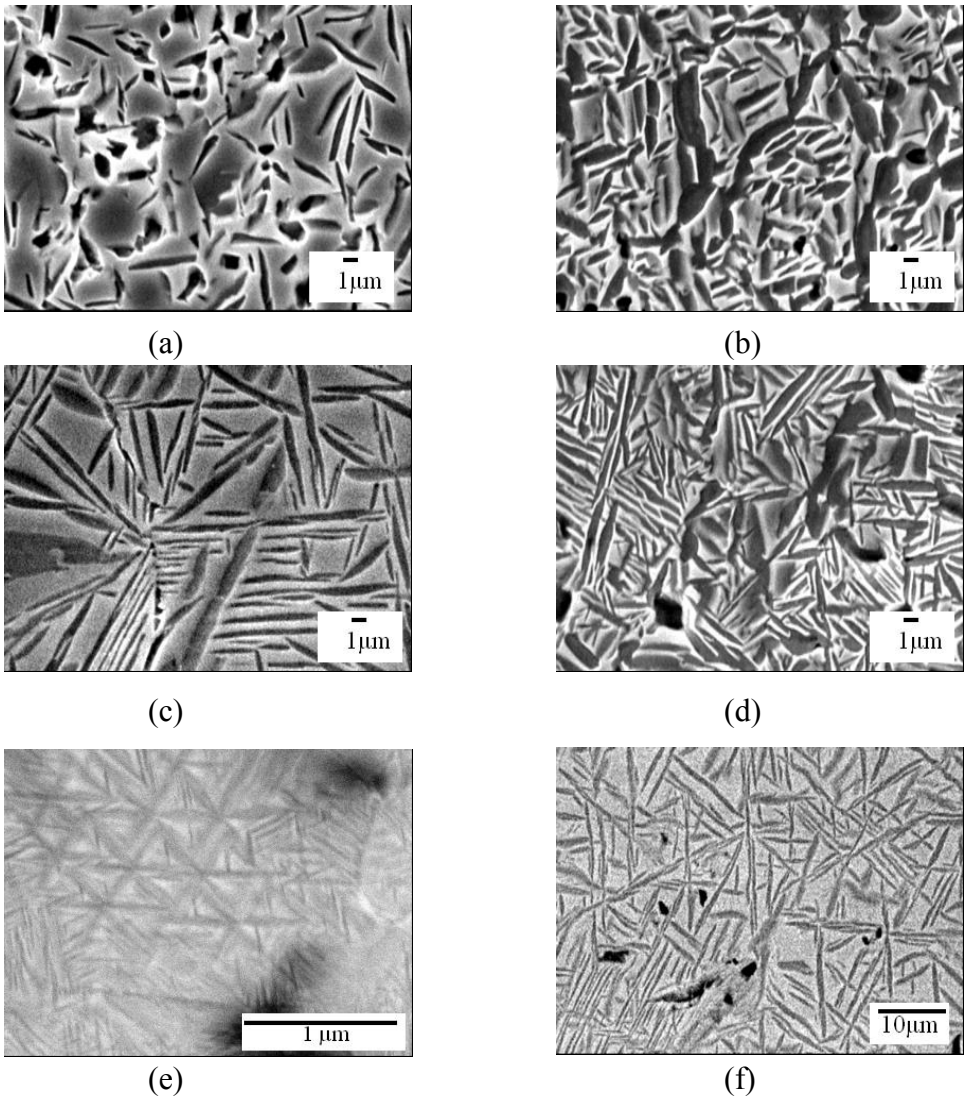

Figure 14. Photomicrographs of heat-treated microstructures: (a) Ti-15Al-33Nb HT:960°C, (b) Ti-21Al-29Nb HT:960°C, (c) Ti-15Al-33Nb HT:1005°C, (d) Ti-21Al-29Nb HT:1005°C, (e) Ti-15Al-33Nb HT:650°C, and (f) Ti-15Al-33Nb HT:1105°C.

4. Phase Volume Fractions

The phase volume fractions for the heat-treated microstructures are given in Table VI for the Ti-15Al-33Nb alloy and Table VII for the Ti-21Al-29Nb alloy. A graph of phase volume fraction versus solutionizing temperature is presented in Figure 15 for solution-treated then water-quenched samples of both alloys.

Table VI. Phase Volume Fractions for Ti-15Al-33Nb Microstructures

Heat Treatment, °C	α_2 Vp	O Vp	BCC Vp
AP	10	0	90
855/3h/WQ	5	34	61
910/3h/WQ	5	17	78
960/3h/WQ	5	0	95
990/3h/WQ	0	0	100
1005/3h/WQ	0	0	100
1050/3h/WQ	0	0	100
1075/3h/WQ	0	0	100
1105/3h/WQ	0	0	100
HT:650	11	73	16
HT:960	5	37	58
HT:1005	1	44	55
HT:1105	1	63	36

Table VII. Phase Volume Fractions for Ti-21Al-29Nb Microstructures

Heat Treatment, °C	α_2 Vp	O Vp	BCC Vp
AP	4	0	96
855/3h/WQ	4	83	13
910/3h/WQ	3	50	47
960/3h/WQ	1	38	61
990/3h/WQ	6	0	94
1005/3h/WQ	5	0	95
1050/3h/WQ	0	0	100
1075/3h/WQ	0	0	100
1105/3h/WQ	0	0	100
HT:960°C	0	72	28
HT:1005°C	5	78	17

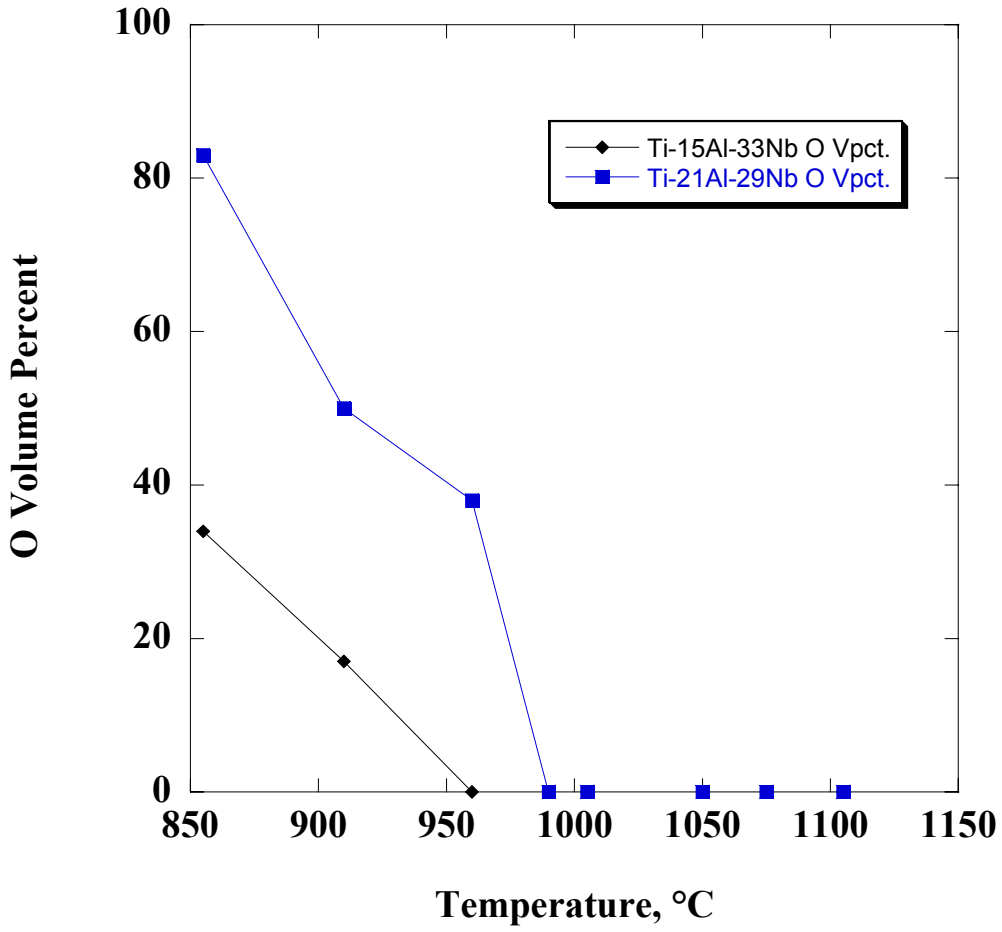

Figure 15. Orthorhombic volume fraction versus solutionizing temperature for both alloys.

The O volume fraction for each alloy decreased with increasing solutionizing temperature. For any given temperature within the O+BCC phase field, Ti-21Al-29Nb contained a larger O volume percent than Ti-15Al-33Nb. Increasing the Al content and decreasing the Nb content in these Ti-Al-Nb alloys favors the formation of more O phase and less BCC phase at a given temperature. At 910°C and above, Ti-15Al-33Nb was devoid of the O phase, while at 960°C and above Ti-21Al-29Nb was devoid of the O phase.

5. Grain Size

The average equiaxed grain size for each Ti-15Al-33Nb and Ti-21Al-29Nb microstructure is given in Table VIII and a plot of grain size versus solutionizing temperature is shown in Figure 16. There is little grain growth apparent below 990°C for Ti-15Al-33Nb and below 1050°C for Ti-21Al-29Nb.

Table VIII. Average Equiaxed Grain Size for Ti-15Al-33Nb and Ti-21Al-29Nb Microstructures

Heat Treatment, °C	Ti-15Al-33Nb Grain Size, μm	Ti-21Al-29Nb Grain Size, μm
855/3h/WQ	4	5.17
910/3h/WQ	5	5.24
960/3h/WQ	6	7.5
990/3h/WQ	100	7
1005/3h/WQ	120	12
1050/3h/WQ	144	135
1075/3h/WQ	157	150
1105/3h/WQ	173	196

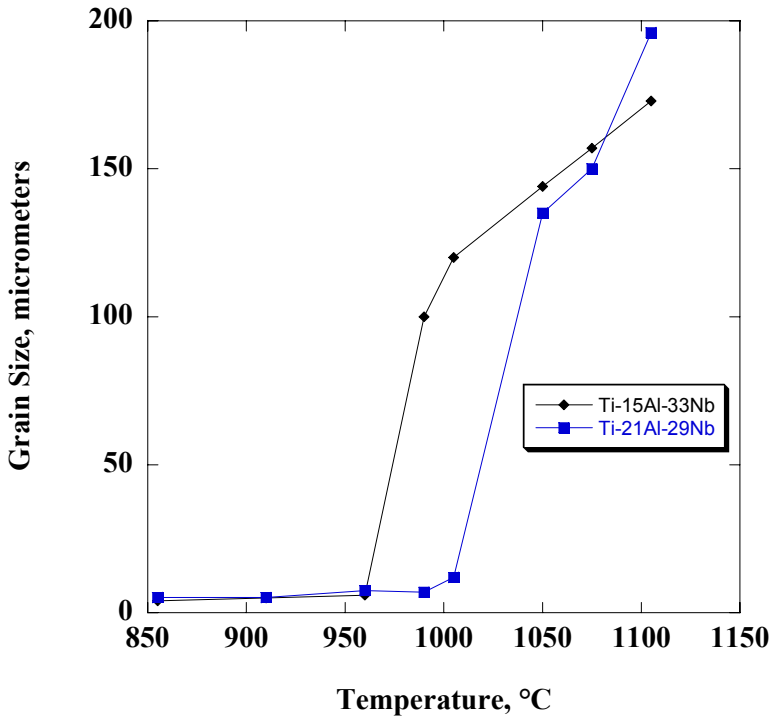

Figure 16. Grain size versus solutionizing temperature for both alloys.

6. X-ray Diffraction

Figures 17 and 18 show Intensity versus 2θ XRD patterns for the Ti-15Al-33Nb and Ti-21Al-29Nb solution treated samples, respectively. Individual XRD patterns for each sample with indexed reflections are available in the appendix. The BCC phase in Ti-Al-Nb alloys can either be the ordered B2 phase or the disordered β phase. The presence of a superlattice (210) reflection in the Intensity versus 2θ XRD pattern occurs when the BCC phase is the ordered B2 phase. This reflection occurs at ~ 64° 2θ with a very weak relative intensity (I/I_o) of 1.[36] Long count time scans were performed on both alloys along with a Ti-16Al-33Nb sample that underwent the following heat treatment: 1105°C/3h/WQ. Figure 19 depicts long count time scans performed on Ti-15Al-33Nb, Ti-16Al-33Nb, and Ti-21Al-29Nb fully BCC microstructures. The Ti-15Al-33Nb and Ti-21Al-29Nb samples underwent the following heat treatment: 1075°C/3h/WQ. The presence of the (210) superlattice peak in Figure 19 (c) confirms that the BCC phase in Ti-21Al-29Nb is in fact ordered B2 and is disordered β in both Ti-15Al-33Nb and Ti-16Al-33Nb. From this it can be concluded that Al additions of up to 16 at% in TiNb does not results in ordering of the BCC phase.

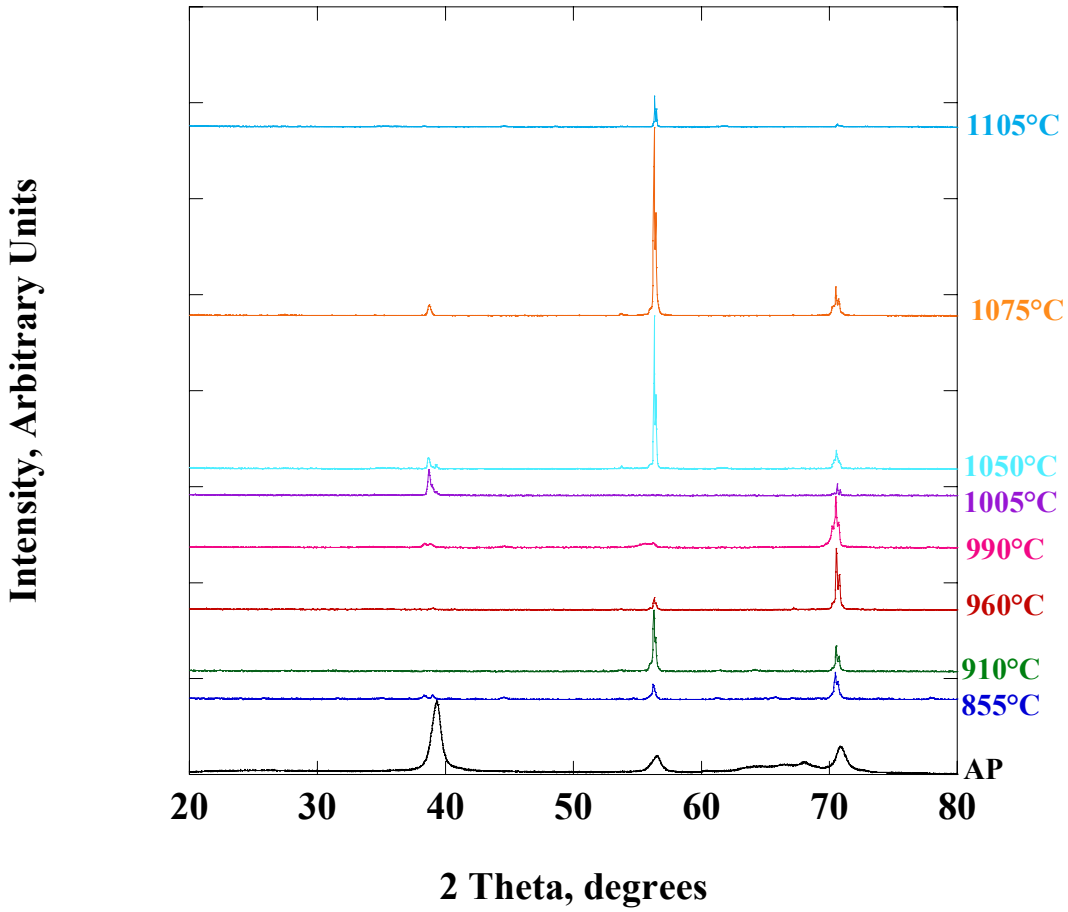

Figure 17. Intensity versus 2θ XRD patterns for all Ti-15Al-33Nb solution-treated samples.

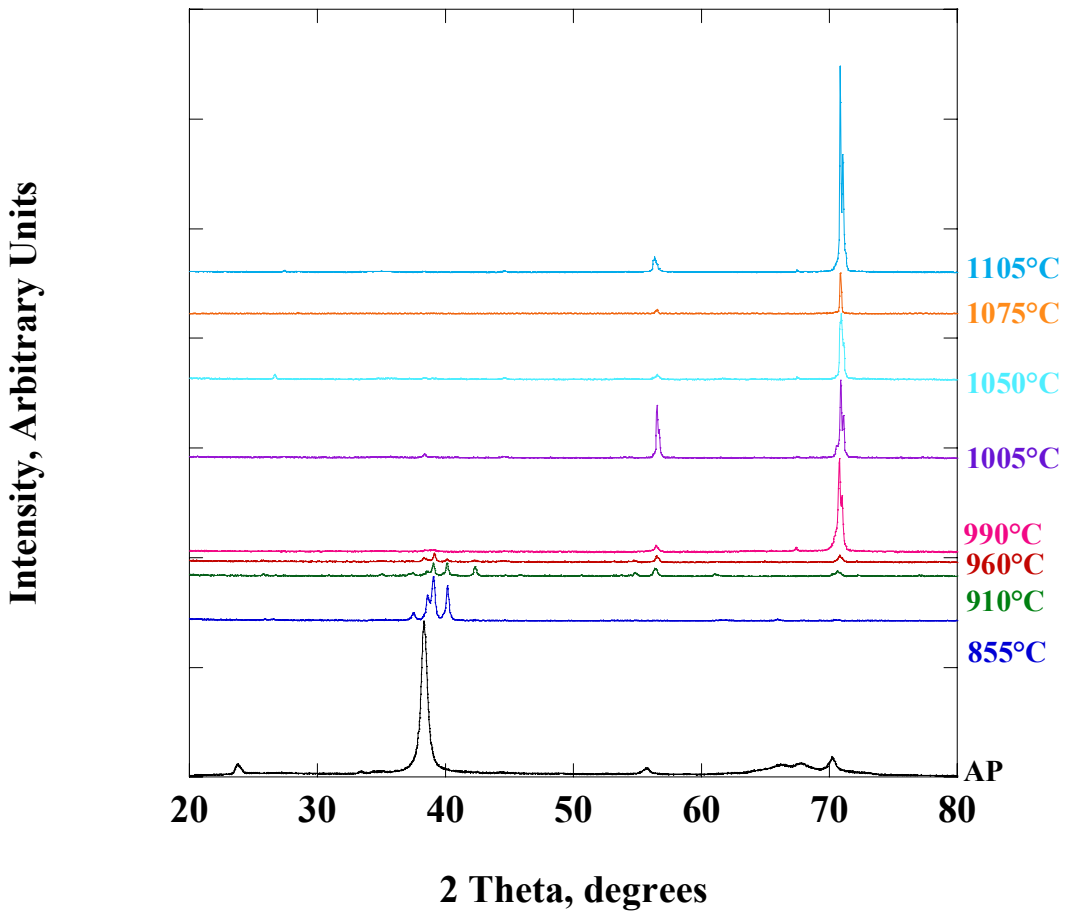

Figure 18. Intensity versus 2θ XRD patterns for all Ti-21Al-29Nb solution-treated samples.

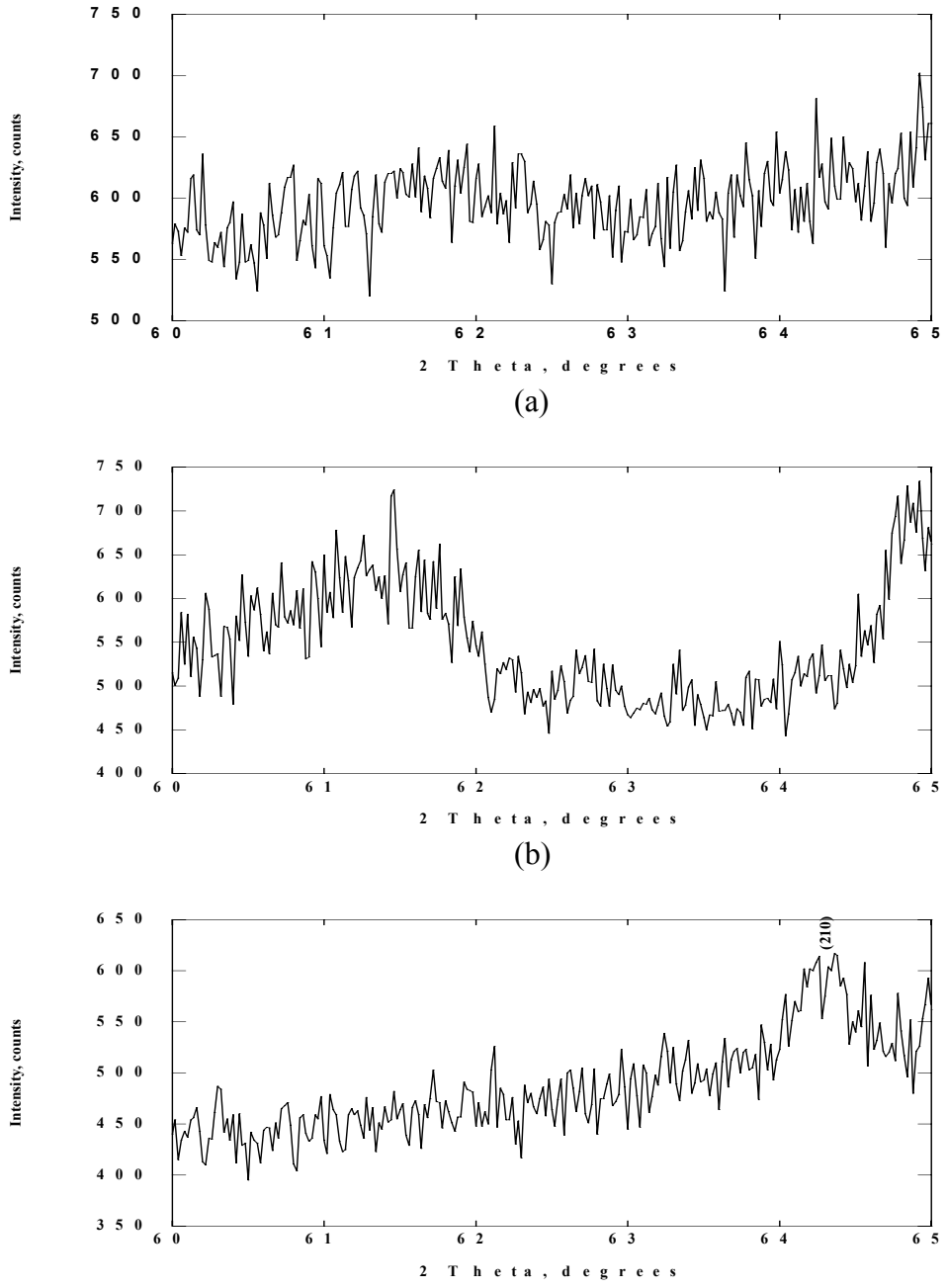

Figure 19. Long count time scans between 60-65° 2θ for (a) Ti-15Al-33Nb, (b) Ti-16Al-33Nb, and (c) Ti-21Al-29Nb. Note the presence of the superlattice (210) reflection in (c).

7. β-Transus Temperature Determination

By combining the results from the DTA, XRD, phase volume fraction analysis, and grain size analysis performed for the heat-treated samples, along with applying the disappearing phase method, the β-transus temperature was estimated for each alloy. For Ti-15Al-33Nb the β-transus was 980°C and for Ti-21Al-29Nb the β-transus was 1040°C.

8. BCC Grain Growth Kinetics

Under isothermal heat-treatment conditions, normal grain growth for single-phase materials is well described by the following empirical equation:[37,38]

$$d^n - d_o^n = k\,t \qquad (2)$$

where n is the grain growth exponent, d is the heat-treated BCC grain size, d_o is the pre-heat treated grain size and in this case the BCC grain size of the as-rolled sheet, and t is the annealing time. The variable k is estimated by the Arrhenius equation:

$$k = k_o \exp(-Qapp/RT) \qquad (3)$$

where k_o is a kinetic constant, Qapp is the activation energy for grain growth, R is the gas constant, and T is absolute temperature. For most single-phase metals, the value of n ranges between 2-10 due to the drag force exerted by solute atoms on grain boundaries.[39] Taking n=3, the corresponding values of k are represented on the ln k versus (1/T) plot depicted in Figure 20 for samples solutionized at different temperatures above the β-transus temperature followed by water-quenching. The activation energy for β grain growth in Ti-15Al-33Nb was determined to be 194 kJ/mol between 990-1105°C and the activation energy for B2 grain growth in Ti-21Al-29Nb was determined to be 311 kJ/mol between 1050-1105°C. A range of possible activation energies was determined by estimating the resolution of the optical microscope to be 1 μm, and these ranges are available in the Appendix.

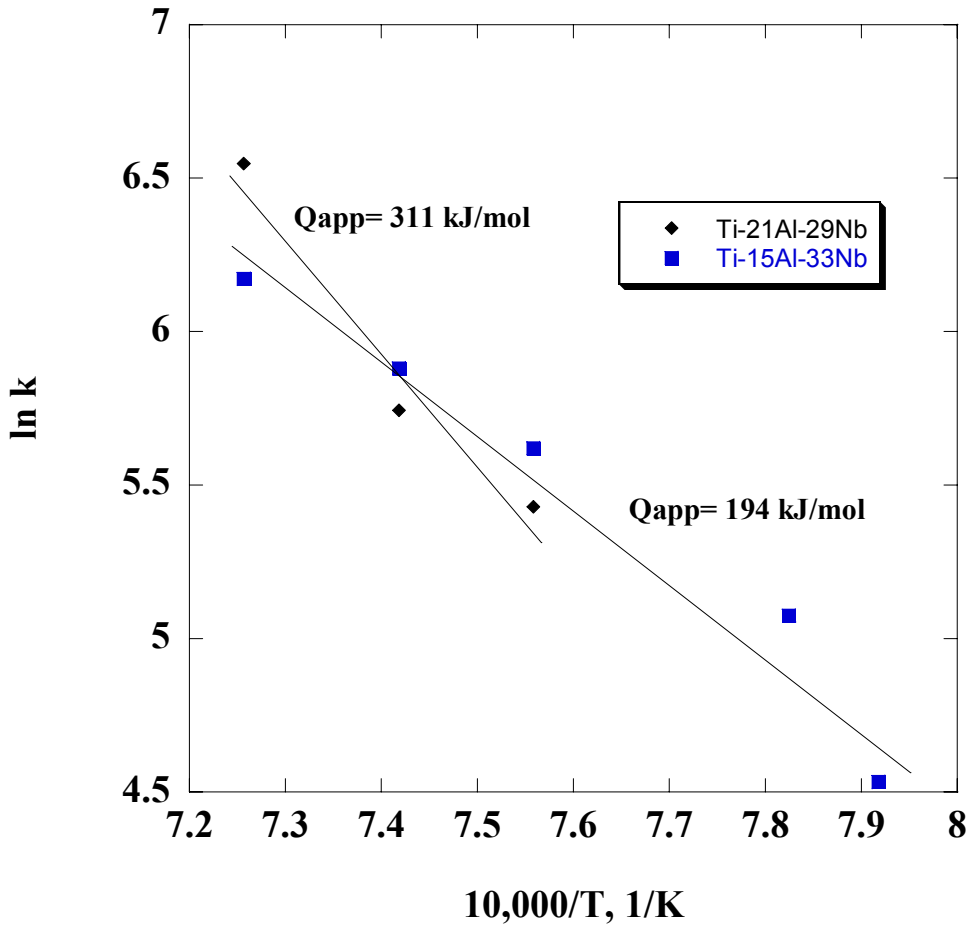

Figure 20. BCC-phase grain growth kinetics for Ti-15Al-33Nb and Ti-21Al-29Nb samples heat-treated at different temperatures above the β-transus temperature followed by water quenching.

Diffusion data on the TiNb system predicts activation energies of 180-188 kJ/mol for Ti-28Nb and 198-210 kJ/mol for Ti-33Nb.[40] The activation energy determined for β grain growth in Ti-15Al-33Nb correlates very well with that for Ti-33Nb (within 6%), but the activation energy for Ti-21Al-29Nb does not. This suggests that the addition of up to 15 at% Al in TiNb does not hinder grain growth diffusion kinetics, but the addition of 21 at% Al in TiNb significantly increases the activation energy required for grain growth.

B. Tensile Study Results

1. Room Temperature Behavior

Figure 21 depicts the stress versus strain curves for Ti-15Al-33Nb and Ti-21Al-29Nb alloys tested at room temperature and Table IX displays the room temperature tensile properties.

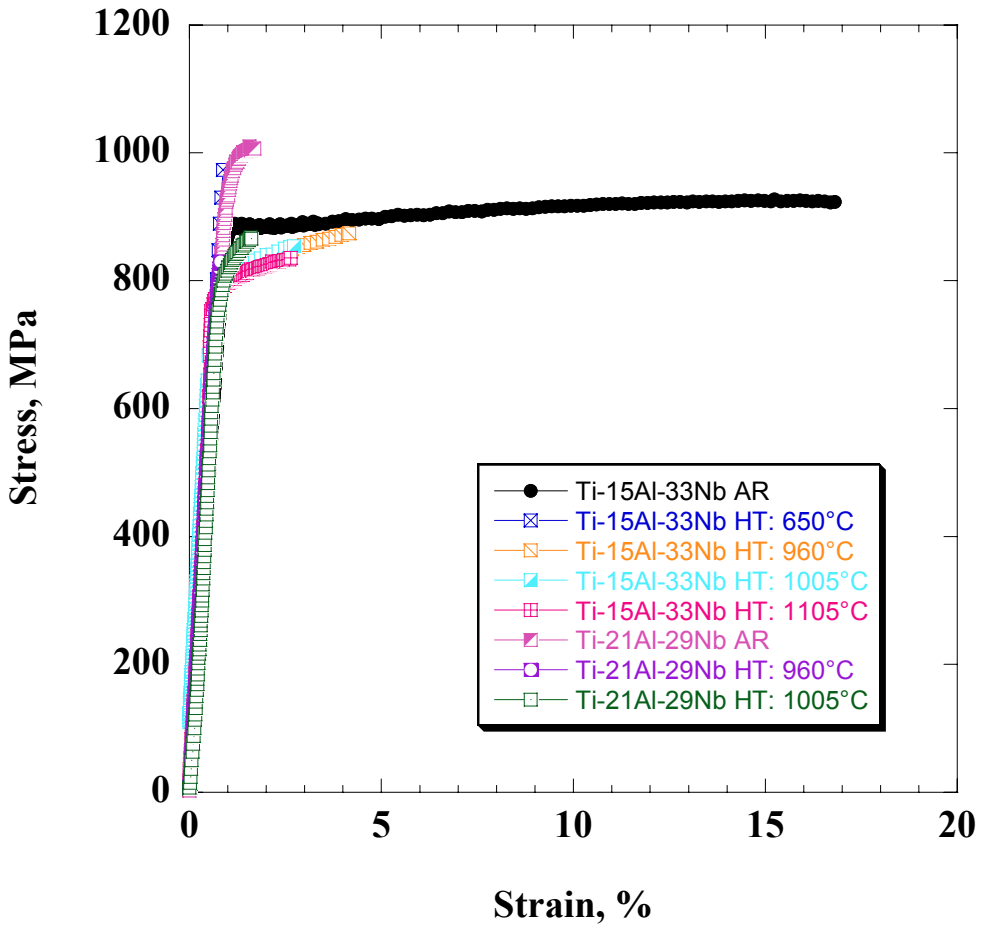

Figure 21. Room temperature tensile behavior of Ti-15Al-33Nb and Ti-21Al-29Nb microstructures.

Table IX. Room Temperature Tensile Properties of Ti-15Al-33Nb and Ti-21Al-29Nb Microstructures

Alloy	Heat Treatment, °C	E, GPa	0.2% YS, MPa	UTS, MPa	ε_f, %	Strength Coefficient, K	Strain Hardening Exponent, n
Ti-15Al-33Nb	AP	94	876	916	12.4	n/a	n/a
Ti-15Al-33Nb	HT:650	112	n/a	920	0.8	n/a	n/a
Ti-15Al-33Nb	HT:960	103	778	867	4.4	1067	0.06
Ti-15Al-33Nb	HT:1005	111	799	852	2.1	1068	0.06
Ti-15Al-33Nb	HT: 1105	113	786	836	2.7	1006	0.05
Ti-21Al-29Nb	AP	103	972	1010	1.7	1455	0.09
Ti-21Al-29Nb	HT: 960	112	n/a	830	0.8	n/a	n/a
Ti-21Al-29Nb	HT:1005	115	803	868	1.6	1509	0.13

n/a indicates 0.2% requirement was not met and/or sample did not strain harden
AP: as-processed condition

The AP condition displayed the best balance of RT properties, such as YS and ε_f, for both alloys. This is due to the fact that both of these microstructures contained a majority of BCC phase by volume, i.e. 90 Vp β for Ti-15Al-33Nb and 96 Vp B2 for Ti-21Al-29Nb. The fact that every Ti-15Al-33Nb microstructure exhibited higher RT elongations than Ti-21Al-29Nb can be attributed to two microstructural features, BCC phase structure and O volume percent. The fact that the BCC phase in Ti-15Al-33Nb is disordered, while it is an ordered intermetallic phase in the Ti-21Al-29Nb alloy, leads to higher ε_f values in Ti-15Al-33Nb.

In every identical heat treatment condition, the Ti-21Al-29Nb alloy contained a larger volume fraction of O phase than Ti-15Al-33Nb. Due to the O phase's inherently lower number of available slip systems compared to the BCC phase, a larger volume fraction of O phase will in general provide strengthening at the expense of ductility. Comparing both alloys in the subtransus HT:960 condition (37 Vp O for Ti-15Al-33Nb versus 72 Vp O for Ti-21Al-29Nb), Ti-15Al-33Nb displayed an ε_f of 4.4% compared to 0.8% for Ti-21Al-29Nb. In the HT:960 condition, the Ti-21Al-29Nb alloy did not meet the proportional requirement for a 0.2% offset YS while Ti-15Al-33Nb displayed at YS of 778 MPa. The HT:650 Ti-15Al-33Nb microstructure also illustrates the effect of O

Vp on RT tensile properties. This microstructure contained 73 Vp O phase and had the highest UTS of the Ti-15Al-33Nb microstructures, but also had the lowest ε_f of 0.8%.

Increasing grain size did not appear to have a deleterious effect on UTS for either alloys, but it did significantly reduce the ε_f values. The effect on grain size on RT tensile properties is illustrated by supertransus heat-treated microstructures. The two Ti-15Al-33Nb supertransus heat-treated microstructures, HT:1005 (d=120 μm) and HT:1105 (d=173 μm) had UTS values 1.5-3.5% less than that of the subtransus HT:960 microstructure. Their ε_f values were 39-53% less than the subtransus HT:960 microstructure, which exhibited an ε_f value of 4.4%.

Photomicrographs of the fracture surfaces of all microstructures tested at room temperature are shown in Figure 22. The fracture surface morphologies of the Ti-15Al-33Nb microstructures display more ductile fracture characteristics than those of the Ti-21Al-29Nb microstructures in all conditions. The Ti-21Al-29Nb fracture surfaces have a flat, cleaved morphology with sparsely dimpled regions while the Ti-15Al-33Nb fractures surfaces appear more fibrous and torn, and contain larger areas of dimpling. Note the very extensive ductile dimpling exhibited by the AP Ti-15Al-33Nb microstructure in Figure 22 (a). As the O phase volume fraction increases and the β volume fraction decreases in the Ti-15Al-33Nb microstructures, the fracture surface morphology contains less dimpling and more cleavage. In all cases, the Ti-21Al-29Nb fracture surfaces exhibited brittle features.

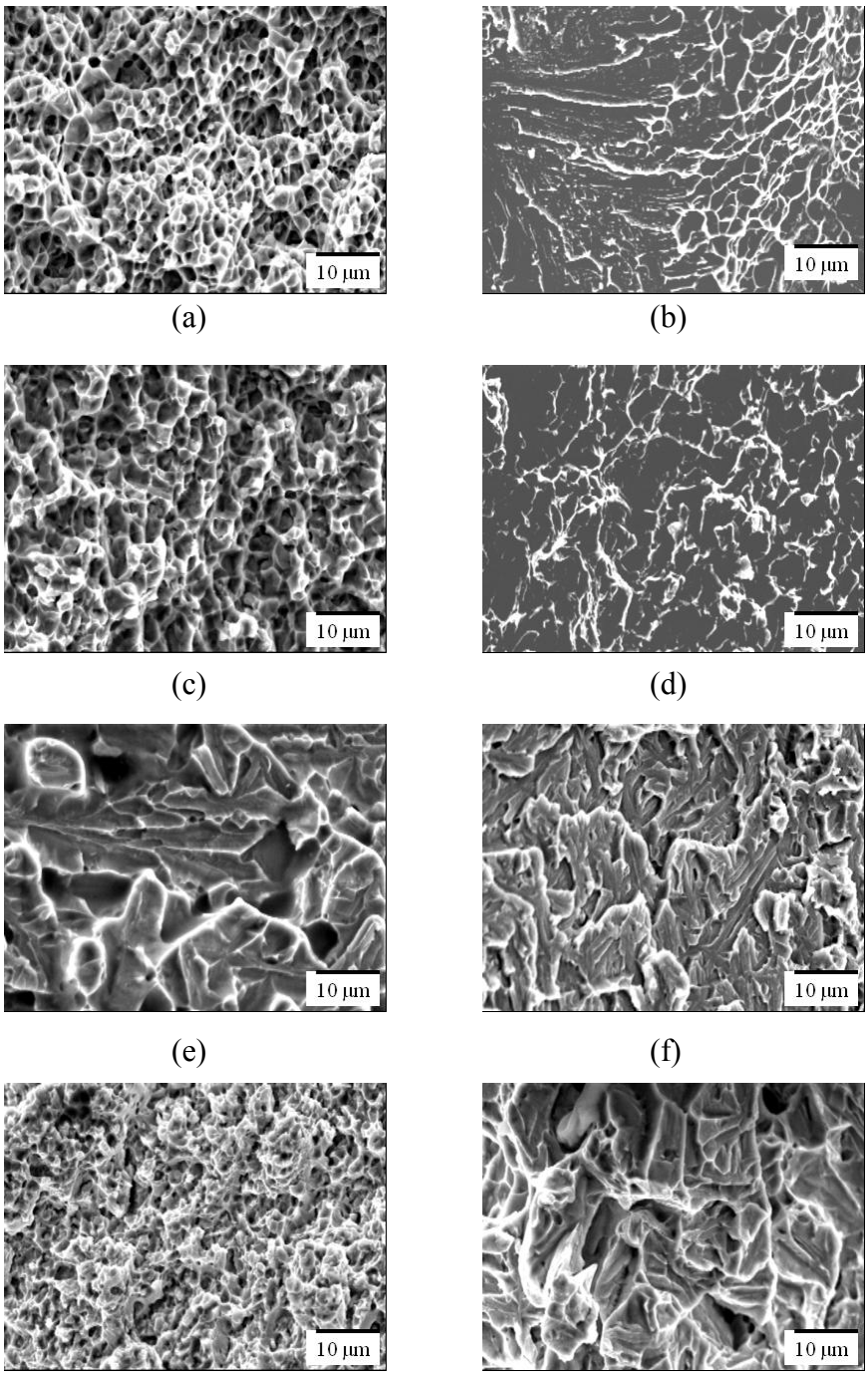

Figure 22. Photomicrographs of RT tensile fracture surfaces: (a) Ti-15Al-33Nb AP, (b) Ti-21Al-29Nb AP, (c) Ti-15Al-33Nb HT:960, (d) Ti-21Al29Nb HT:960, (e) Ti-15Al-33Nb HT:1005, (f) Ti-21Al-29Nb HT:1005, (g) Ti-15Al-33Nb HT:650, and (h) Ti-15Al-33Nb HT:1105.

2. Elevated Temperature Behavior

Figure 23 depicts the stress versus strain curves for Ti-15Al-33Nb and Ti-21Al-29Nb alloys tensile tested at 650°C, and Table X displays the corresponding tensile properties. Table XI shows the change in tensile properties for each microstructure when tested at 650°C compared to room temperature. At 650°C, all alloys had lower E, YS, and UTS values and increased ε_f values which follows the expected trends. The increase in ε_f values for all microstructures can be attributed the thermally assisted activation of a larger number of slip systems at 650°C. In Ti-26Al-21Nb, it has been shown that above 450°C, 'c' component dislocations become active along with the 'a' and 'a*' component dislocations that are active in the O phase at RT.[41] The microstructures that exhibited the most dramatic increase in ε_f were the heat-treated microstructures, which contained a larger O Vp (see Table X). The most striking example of this was the Ti-15Al-33Nb HT:650°C microstructure. This microstructure displayed only a 6% decrease in UTS compared to room temperature and a dramatic increase in ε_f. This is attributable to its large volume fraction of O phase (73 Vp) and fine grain size of 4 μm. Heat-treated samples that did not exhibit a 0.2% YS at room temperature, due to their low ε_f values, did at 650°C. All microstructures strain hardened at 650°C. The elastic modulus of all the microstructures decreased by ~30% at 650°C. Photomicrographs of the fracture surfaces of all microstructures tested at 650°C are shown in Figure 24. These fracture surface observations correlate well with the increased ε_f values obtained.

Table X. 650°C Tensile Properties of Ti-15Al-33Nb and Ti-21Al-29Nb Microstructures

Alloy	Heat Treatment, °C	E, GPa	0.2% YS, MPa	UTS, MPa	ε_f, %	Strength Coefficient, K	Strain Hardening Exponent, n
Ti-15Al-33Nb	AP	66	592	601	12.8	658	0.02
Ti-15Al-33Nb	HT:650	77	770	865	7.9	767	0.13
Ti-15Al-33Nb	HT:960	66	522	561	8.0	515	0.09
Ti-15Al-33Nb	HT:1005	76	546	588	5.9	546	0.09
Ti-15Al-33Nb	HT: 1105	94	531	609	9.5	562	0.11
Ti-21Al-29Nb	AP	71	810	825	2.0	795	0.05
Ti-21Al-29Nb	HT: 960	82	656	664	1.6	670	0.10
Ti-21Al-29Nb	HT:1005	77	537	657	5.2	558	0.12

AP: as-processed condition

Table XI. Difference In Tensile Properties at 650°C Compared to Room Temperature

Alloy	Heat Treatment, °C	% Decrease in E-mod, GPa	% Decrease in 0.2% YS, MPa	% Decrease in UTS, MPa	% Increase in ε_f, %
Ti-15Al-33Nb	AP	30	32	34	2.5
Ti-15Al-33Nb	HT:650	31	n/a	6	969
Ti-15Al-33Nb	HT:960	36	33	35	184
Ti-15Al-33Nb	HT:1005	32	32	31	283
Ti-15Al-33Nb	HT: 1105	17	32	27	353
Ti-21Al-29Nb	AP	31	17	18	15
Ti-21Al-29Nb	HT: 960	27	n/a	20	196
Ti-21Al-29Nb	HT:1005	33	33	24	320

n/a indicates no 0.2% YS at RT

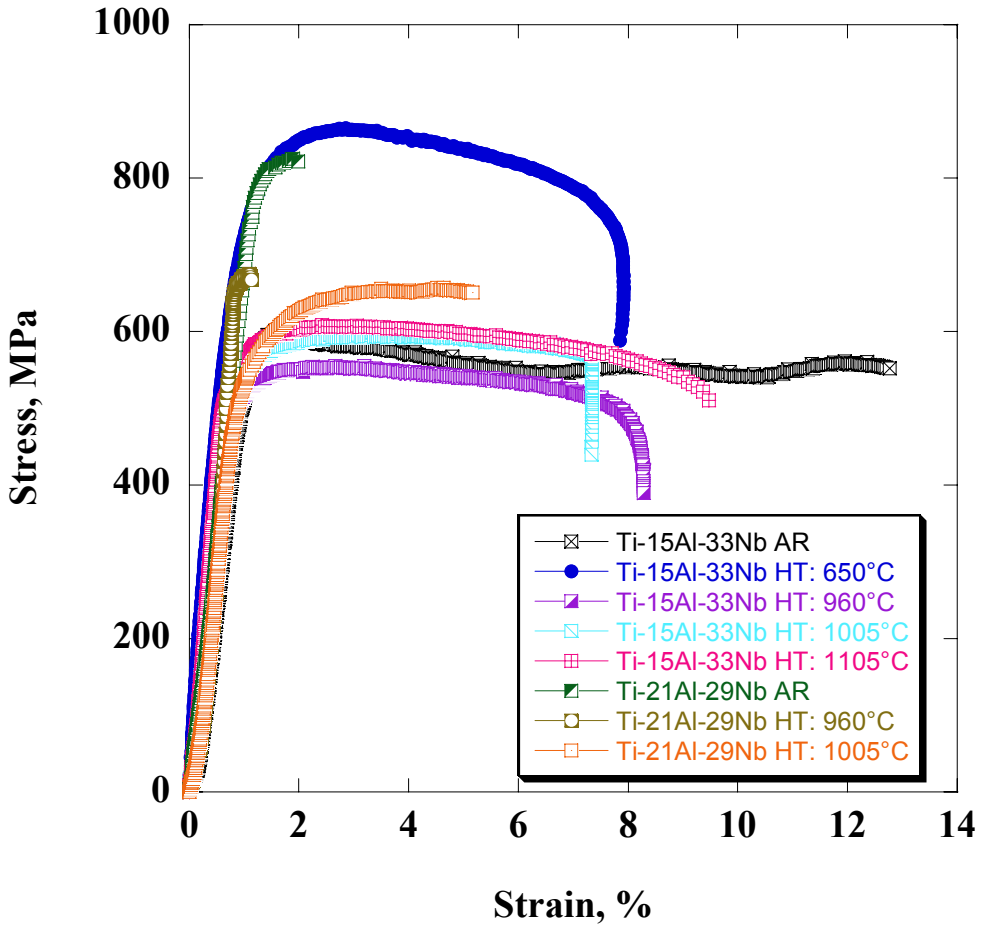

Figure 23. 650°C tensile behavior of Ti-15Al-33Nb and Ti-21Al-29Nb microstructures.

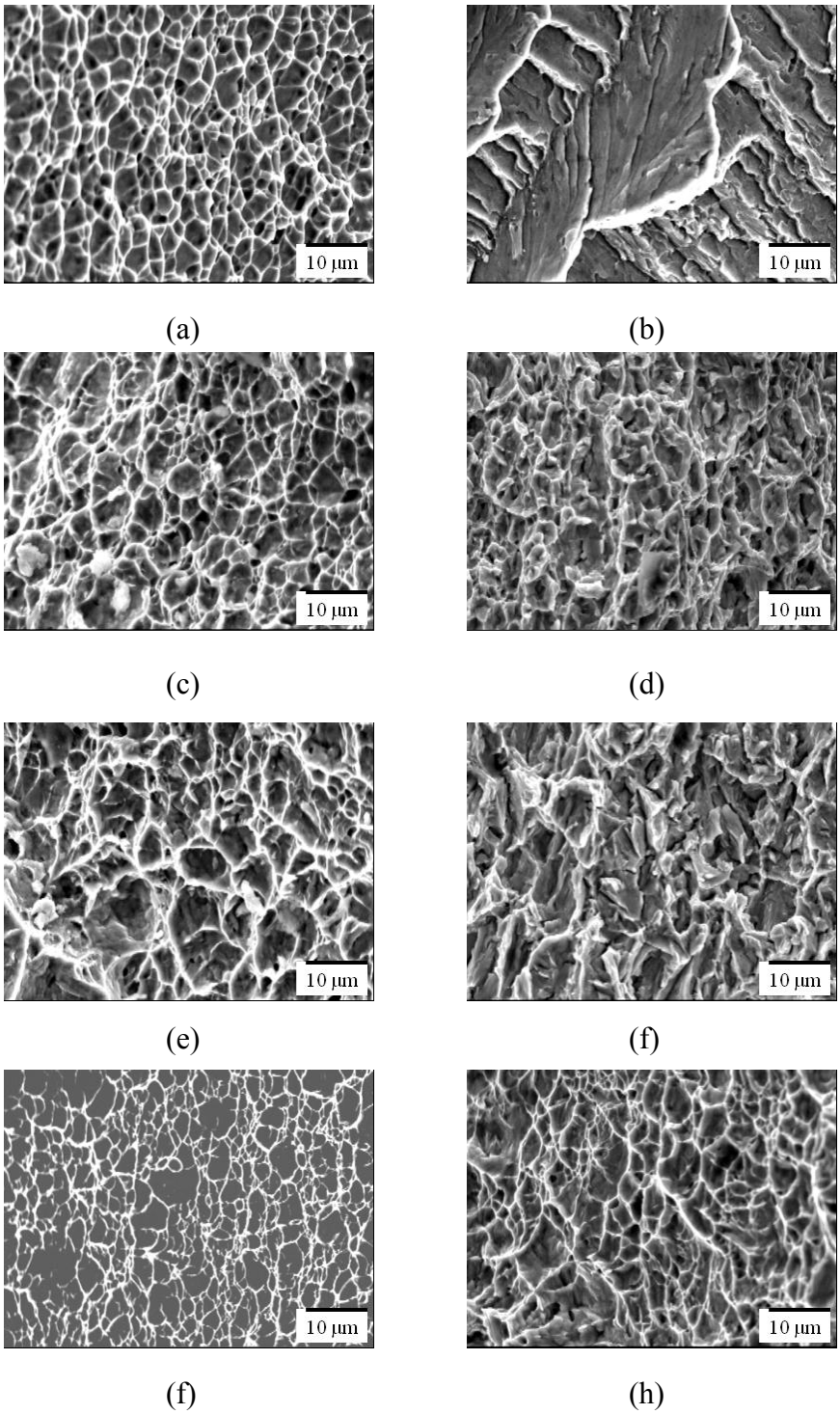

Figure 24. Photomicrographs of 650°C tensile fracture surfaces: (a) Ti-15Al-33Nb AP, (b) Ti-21Al-29Nb AP, (c) Ti-15Al-33Nb HT:960, (d) Ti-21Al-29Nb HT:960, (e) Ti-15Al-33Nb HT:1005, (f) Ti-21Al-29Nb HT:1005, (g) Ti-15Al-33Nb HT:650, and (h) Ti-15Al-33Nb HT:1105.

C. Creep Study Results

1. Steady State Strain Rates, Creep Stress Exponents, and Apparent Activation Energies

The creep behavior of the Ti-15Al-33Nb and Ti-21Al-29Nb samples resembled that for most pure metals and alloys, exhibiting the primary, secondary, and tertiary stages of creep.[28] In order to determine secondary creep stress exponents and activation energies, constant temperature/load jump tests and constant load/temperature jump tests were performed. This was accomplished by either changing the load or temperature after a steady state creep rate ($\dot{\varepsilon}_{ss}$) had been achieved. Data obtained from a typical load-jump experiment conducted at 650/670°C in shown in Figure 25 and data obtained from a typical temperature-jump experiment conducted at 150 MPa is shown in Figure 26.

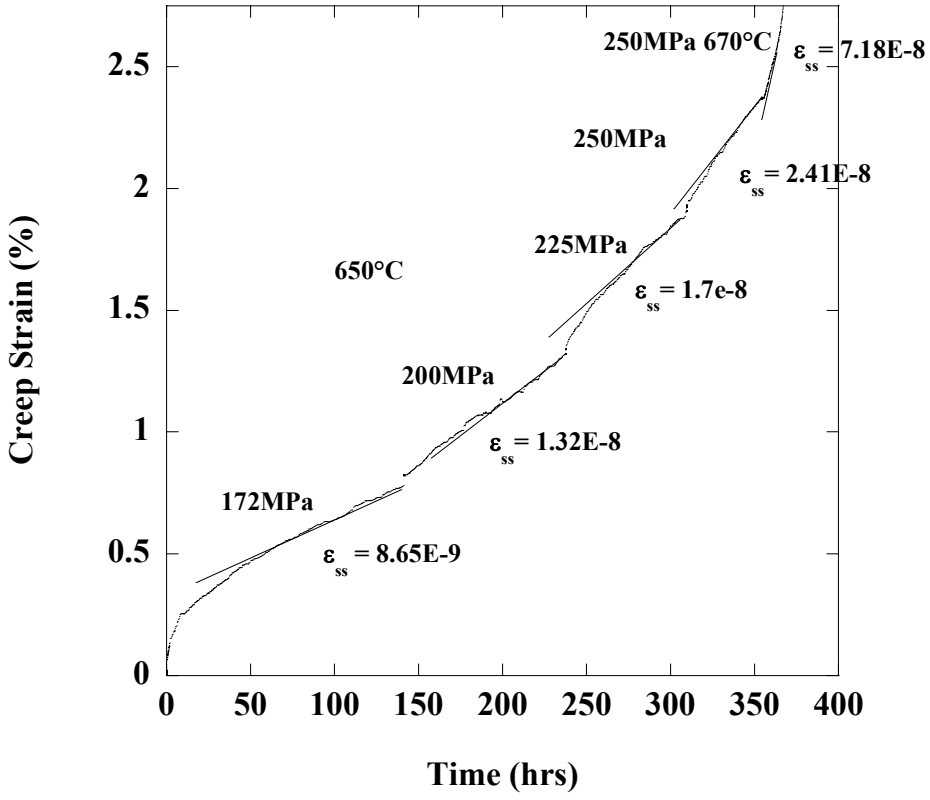

Figure 25. Creep strain versus time data obtained from a Ti-15Al-33Nb HT:1105 sample during a load-jump experiment.

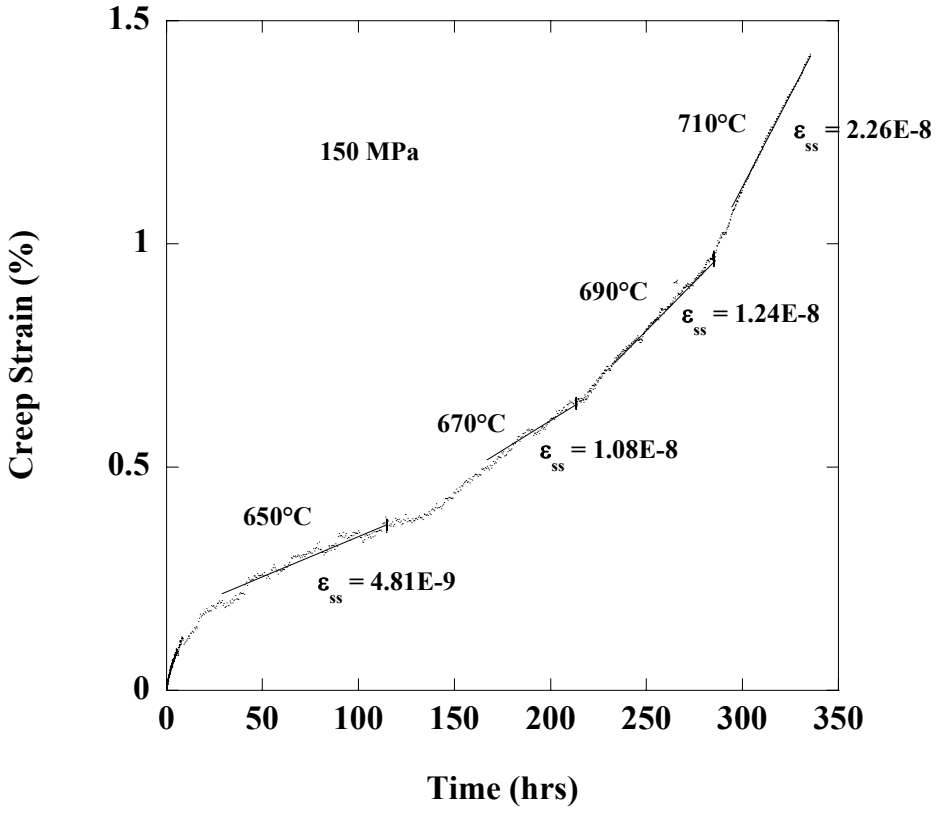

Figure 26. Creep strain versus time data obtained from a Ti-15Al-33Nb HT:1105 sample during a temperature-jump experiment.

The measured steady-state strain rates and average equiaxed grain sizes of creep tested samples are given in Table XII for subtransus heat-treated Ti-15Al-33Nb microstructures, Table XIII for supertransus heat-treated Ti-15Al-33Nb microstructures, and Table XIV for Ti-21Al-29Nb microstructures. Table XV presents the measured creep exponents and apparent activation energies for Ti-15Al-33Nb and Ti-21Al-29Nb microstructures.

Figure 27 illustrates the log $\dot{\varepsilon}_{ss}$ versus log σ behavior for all Ti-15Al-33Nb microstructures creep tested at 650°C, and Figure 28 illustrates the same behavior for all Ti-21Al-29Nb microstructures tested at 650°C. Both plots are combined in Figure 29 in order to rank the creep resistance of all the microstructures. From Figure 29 it can clearly be seen that the Ti-15Al-33Nb HT:1005 and HT:1105 microstructures were the most creep resistant microstructures produced in this study, while both HT:650 microstructures

displayed the worst creep resistance. The creep resistance of the microstructures produced in this study can be ranked as follows: Ti-15Al-33Nb HT:1005>Ti-15Al-33Nb HT:1105>Ti-21Al-29Nb HT:1005>Ti-21Al-29Nb HT:960>Ti-15Al-33Nb HT:960>Ti-15Al-33Nb HT:650/250h>Ti-15Al-33Nb HT:650/100h. Activation energies determined at 50, 150, and 275 MPa are presented in Figures 30, 31, and 32, respectively.

Table XII. Measured Steady State Strain Rates and Grain Size for Subtransus Heat-Treated Ti-15Al-33Nb Microstructures

Heat Treatment, °C	Stress/ Temperature, MPa/°C	Steady State Strain Rate, s^{-1}	Grain Size, μm
HT:650/100h	99/650	1.35E-07	4
HT:650/100h	124/650	1.63E-07	4
HT:650/100h	136/650	1.73E-07	4
HT:650/100h	150/650	1.91E-07	4
HT:650/100h	172/650	2.60E-07	4
HT:650/250h	49/650	1.07E-08	4
HT:650/250h	75/650	1.43E-08	4
HT:650/250h	99/650	3.11E-08	4
HT:650/250h	126/650	1.19E-07	4
HT:650/250h	149/650	2.07E-07	4
HT:650/250h	170/650	4.46E-07	4
HT:960	49/650	7.87E-09	6
HT:960	49/670	9.27E-09	6
HT:960	49/690	1.14E-08	6
HT:960	49/710	2.12E-08	6
HT:960	74/650	1.26E-08	6
HT:960	74/710	5.51E-08	6
HT:960	99/650	2.46E-08	6
HT:960	100/710	1.31E-07	6
HT:960	124/650	3.03E-08	6
HT:960	135/650	4.18E-08	6
HT:960	147/650	6.70E-08	6
HT:960	172/650	1.41E-07	6

* the steady state strain rate resolution was estimated to be ± 2.8E-9 s^{-1}

Table XIII. Measured Steady State Strain Rates and Grain Size for Supertransus Heat-Treated Ti-15Al-33Nb Microstructures

Heat Treatment, °C	Stress/ Temperature, MPa/°C	Steady State Strain Rate, s^{-1}	Grain Size, μm
HT:1005	150/650	5.78E-09	120
HT:1005	150/670	8.36E-09	120
HT:1005	150/690	1.51E-08	120
HT:1005	150/710	2.01E-08	120
HT:1005	171/650	7.60E-09	120
HT:1005	201/650	1.07E-08	120
HT:1005	226/650	1.53E-08	120
HT:1005	251/650	2.08E-08	120
HT:1005	273/650	5.19E-08	120
HT:1005	273/670	1.06E-07	120
HT:1005	273/690	2.47E-07	120
HT:1105	151/650	4.81E-09	173
HT:1105	151/670	1.08E-08	173
HT:1105	151/690	1.24E-08	173
HT:1105	151/710	2.26E-08	173
HT:1105	172/650	8.65E-09	173
HT:1105	200/650	1.32E-08	173
HT:1105	225/650	1.70E-08	173
HT:1105	249/650	2.41E-08	173
HT:1105	249/670	7.18E-08	173
HT:1105	275/650	3.39E-08	173
HT:1105	275/670	7.04E-08	173
HT:1105	275/683	1.44E-07	173
HT:1105	275/690	1.82E-07	173

* the steady state strain rate resolution was estimated to be ± 2.8E-9 s^{-1}

Table XIV. Measured Steady State Strain Rates and Grain Size for Heat-Treated Ti-21Al-29Nb Microstructures

Heat Treatment, °C	Stress/ Temperature, MPa/°C	Steady State Strain Rate, s^{-1}	Grain Size, μm
HT:960	48/650	9.35E-10	7.5
HT:960	48/690	3.64E-09	7.5
HT:960	48/710	1.01E-08	7.5
HT:960	77/650	2.11E-09	7.5
HT:960	77/710	1.49E-08	7.5
HT:960	101/650	3.98E-09	7.5
HT:960	126/650	1.06E-08	7.5
HT:960	136/650	1.42E-08	7.5
HT:960	151/650	2.79E-08	7.5
HT:960	171/650	5.32E-08	7.5
HT:1005	48/650	3.63E-10	12
HT:1005	73/650	6.31E-10	12
HT:1005	100/650	3.18E-09	12
HT:1005	126/650	3.74E-09	12
HT:1005	148/650	6.54E-09	12
HT:1005	148/670	8.93E-09	12
HT:1005	148/690	1.65E-08	12
HT:1005	148/710	3.60E-08	12
HT:1005	172/650	1.10E-08	12

* the steady state strain rate resolution was estimated to be ± 2.8E-9 s^{-1}

Table XV. Measured Creep Exponents and Apparent Activation Energies for Ti-15Al-33Nb and Ti-21Al-29Nb Heat-Treated Microstructures

Alloy	Heat Treatment, °C	Stress/Temperature, MPa/°C	n	Stress/Temperature, MPa/°C	Qapp, kJ/mol
Ti-15Al-33Nb	HT:650/100h	99-172/650	1.1		
Ti-15Al-33Nb	HT:650/250h	49-99/650	1.5		
		99-170/650	4.7		
Ti-15Al-33Nb	HT:960	49-124/650	1.6	48/650-710	115
		124-172/650	4.8		
Ti-15Al-33Nb	HT:1005	148-226/650	2.4	150/650-710	163
		226-273/650	6	273/650-690	288
Ti-15Al-33Nb	HT:1105	151-275/650	3.1	151/650-710	181
				275/650-690	317
Ti-21Al-29Nb	HT:960	48-101/650	2.1	48/650-710	292
		101-171/650	4.8		
Ti-21Al-29Nb	HT:1005	48-126	2.8	148/650-710	215
		126-250	4.1		

* using the estimated strain rate resolution, the calculated range of Qapp values is given in Table A-I in the Appendix

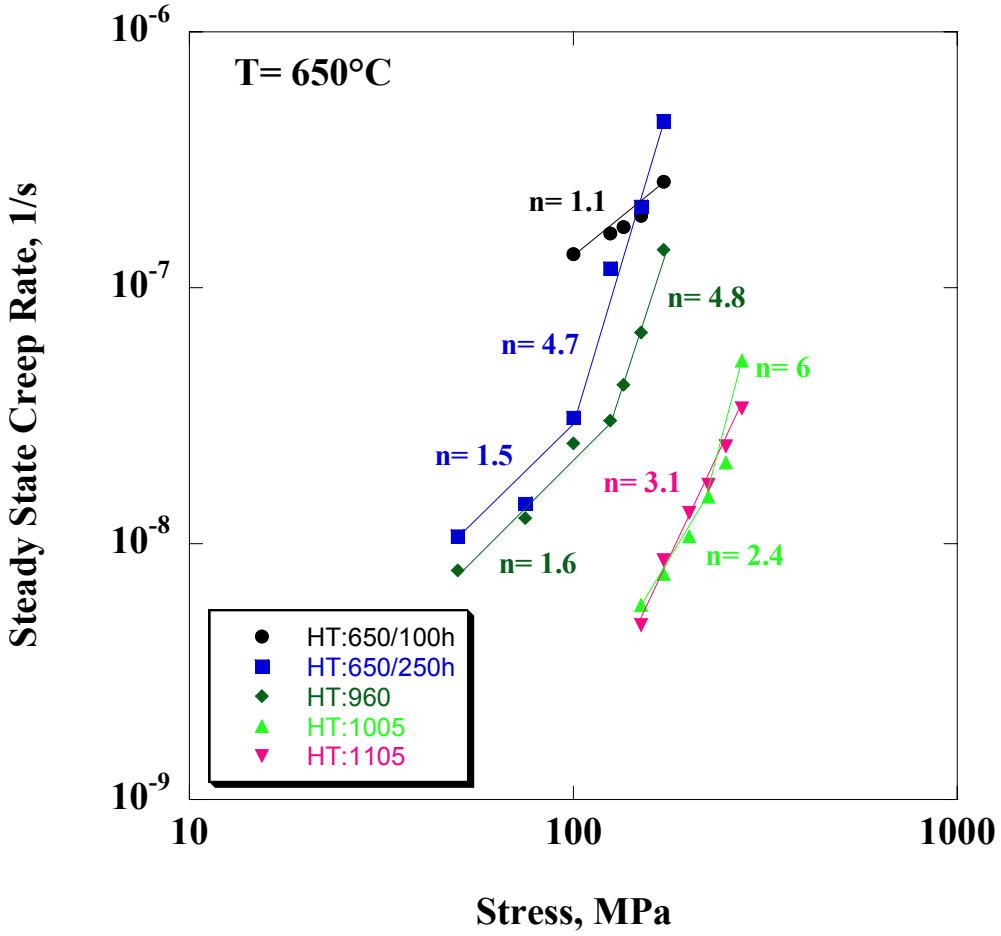

Figure 27. Plot of log $\dot{\varepsilon}_{ss}$ versus log σ for Ti-15Al-33Nb creep tested microstructures at T = 650°C.

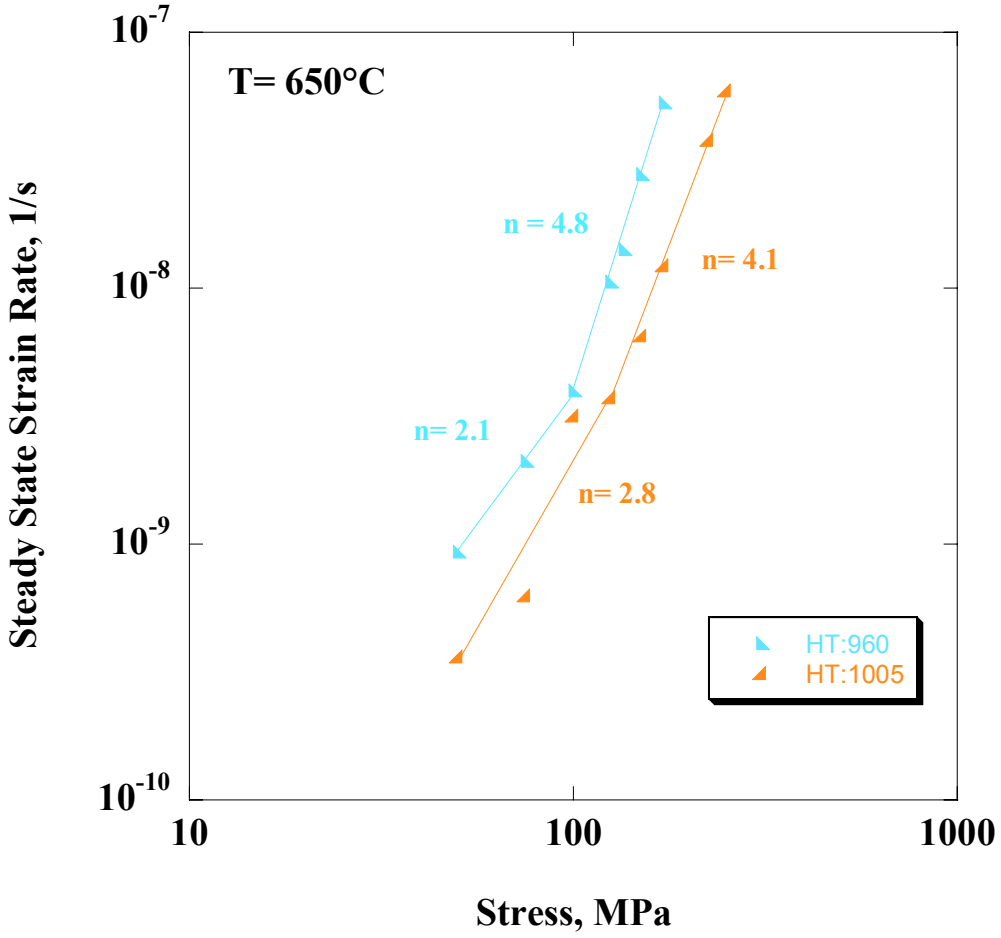

Figure 28. Plot of log $\dot{\varepsilon}_{ss}$ versus log σ for Ti-21Al-29Nb creep tested microstructures at T = 650°C.

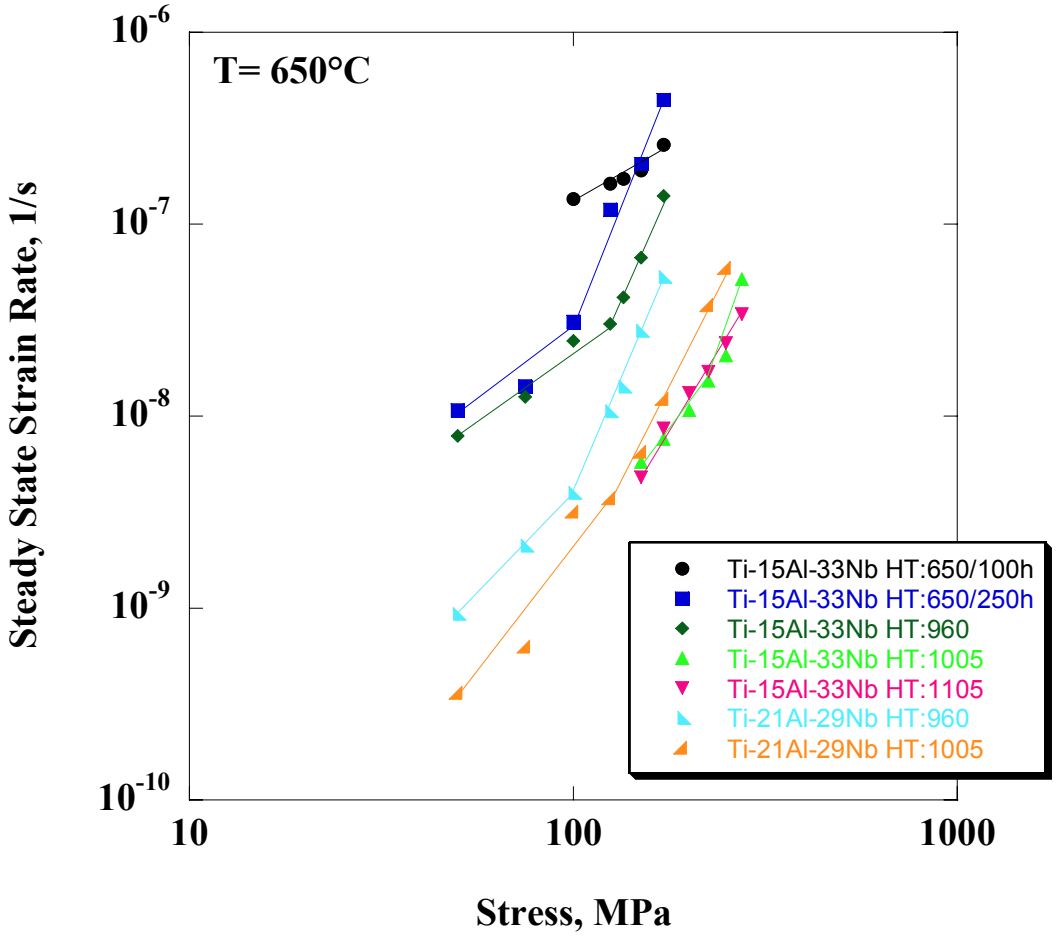

Figure 29. Plot of log $\dot{\varepsilon}_{ss}$ versus log σ for all microstructures creep tested in this study at T = 650°C.

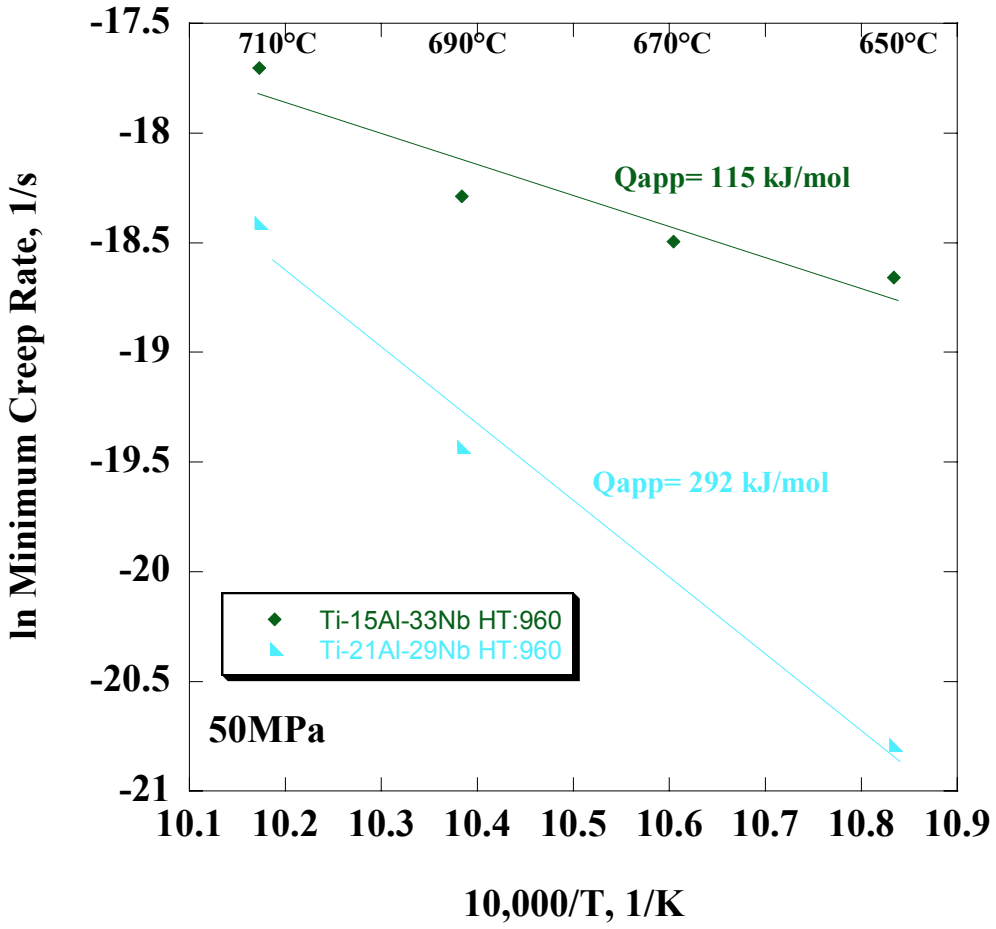

Figure 30. Activation Energies determined at σ = 50 MPa.

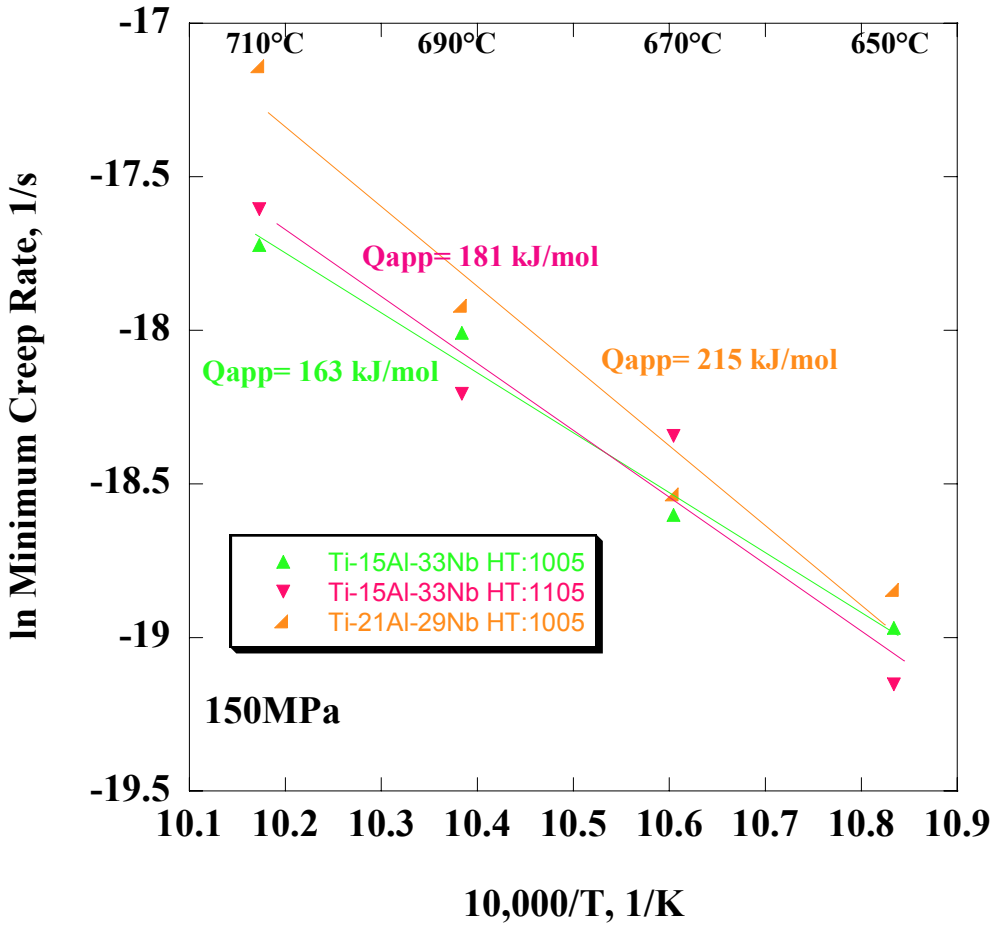

Figure 31. Activation Energies determined at σ = 150 MPa.

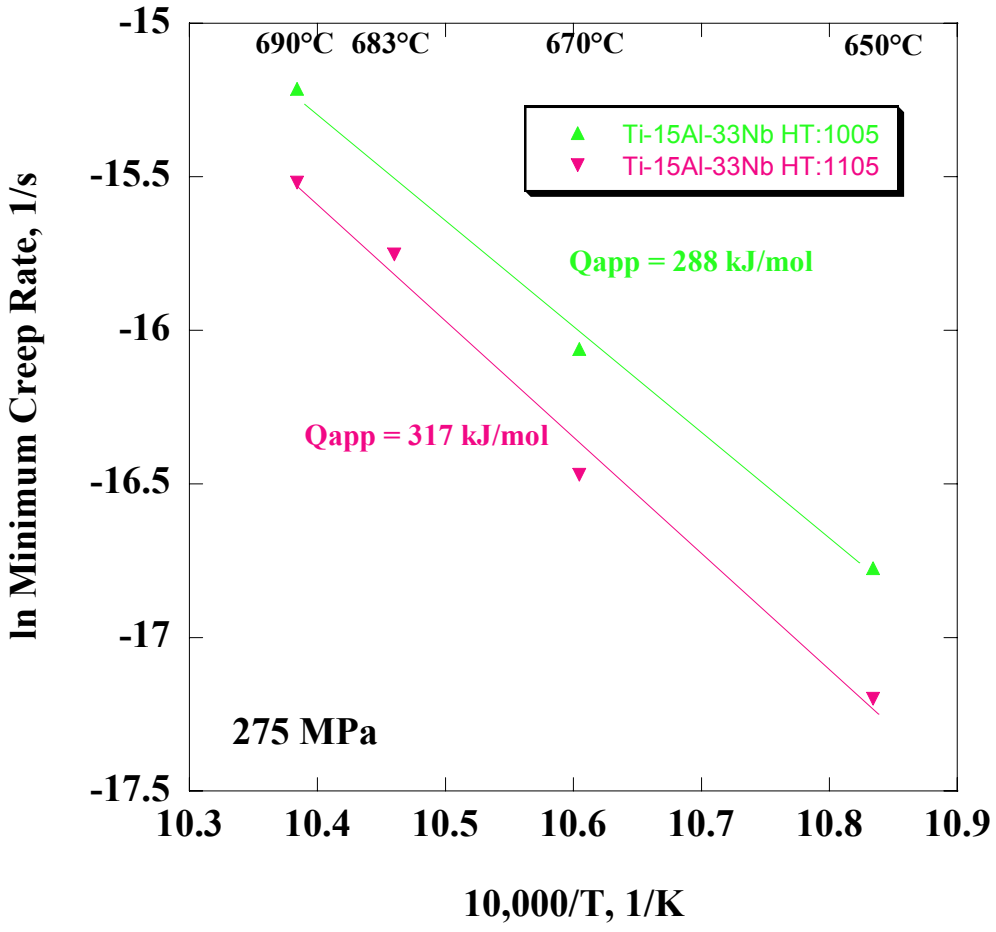

Figure 32. Activation Energies determined at σ = 275 MPa.

2. Proposed Deformation Mechanisms

The two supertransus heat-treated microstructures, Ti-15Al-33Nb HT:1005, and HT:1105 displayed the greatest creep resistance at of all the microstructures tested. Over the stress range of 150-225 MPa for HT:1005 and 150-275 MPa for HT:1105, both microstructures had constant n values which implies that a single deformation mechanism was dominant over this stress range. The n value was 2.4 for HT:1005 and 3.1 for HT:1105. The Qapp's determined at 150 MPa were 163 kJ/mol and 181 kJ/mol for HT:1005 and HT:1105, respectively. At 275 MPa the Qapp values were 288 kJ/mol and 317 kJ/mol for HT:1005 and HT:1105, respectively. For the stress range of 150-225 MPa, the HT:1005 microstructure is proposed to be deforming by grain boundary sliding and above 225 MPa dislocation climb is the suggested deformation mechanism. The n value for the HT:1105 microstructure suggests a single deformation mechanism is operating from 150-275 MPa, but the different Qapp values at 150 MPa and 275 MPa suggests different mechanisms. Due to the extremely similar creep strain versus life behavior of both microstructures, it can be concluded that the same deformation mechanisms operating for the HT:1005 microstructure are operating for the HT:1105 microstructure.

The subtransus microstructures exhibited worse creep resistance than the supertransus microstructures. The Ti-15Al-33Nb HT:960 microstructure had an n value of 1.6 from 50 to 125 MPa, with a Qapp of 115 kJ/mol at 50 MPa, and an n value of 4.8 from 125 to 172 MPa. The n and Qapp values suggest Coble creep or grain boundary sliding deformation in the applied stress range of 50-125 MPa and then a transition to dislocation climb creep deformation at stresses greater than or equal to 125MPa.

The HT:650/100h microstructure had an n value of 1.1 from 100-172 MPa. With an absence of Qapp data, this microstructure is showing either N-H or Coble creep deformation behavior from 100-172MPa, based on the n value determined. The HT:650/200h microstructure display different creep behavior than the HT:650/100h microstructure. From 50-100 MPa an n value of 1.5 was determined, suggesting either N-H or Coble creep to be active. However, for the HT:650/250h microstructure a transition to dislocation climb controlled creep is thought to have occurred from 100-172MPa (n = 4.7 for this stress range).

The Ti-21Al-29Nb microstructures creep tested in this study displayed similar creep deformation behavior. The HT:960 microstructure had a n value of 2.1 over the stress range of 50-100 MPa and an n value of 4.8 above 100 MPa. At 50 MPa this microstructure had a Qapp of 292 kJ/mol. In the low stress regime, creep deformation is probably occurring by either grain boundary sliding or N-H creep due to its activation energy being closer to that for lattice bulk diffusion and the n value of ~ 2. The HT:1005 microstructure had a n value of 2.8 from 50 to 125 MPa, then transitioned to an n value of 4.1 from 125-250MPa. An activation energy of 215 kJ/mol at 150 MPa was determined, which is in the high stress regime for this microstructure. From 150-250 MPa at 650°C, deformation by dislocation climb is the most probable mechanism.

The effect of increasing temperature on creep behavior is shown in Figure 33 for a Ti-15Al-33Nb HT:960 sample. As the temperature is increased from 650°C to 710°C the n value increases between 50-100 MPa. This suggests that the active deformation mechanism at this stress range (proposed to be Coble creep or grain boundary sliding) is moving more towards a dislocation climb mechanism as temperature is increased from 650°C to 710°C.

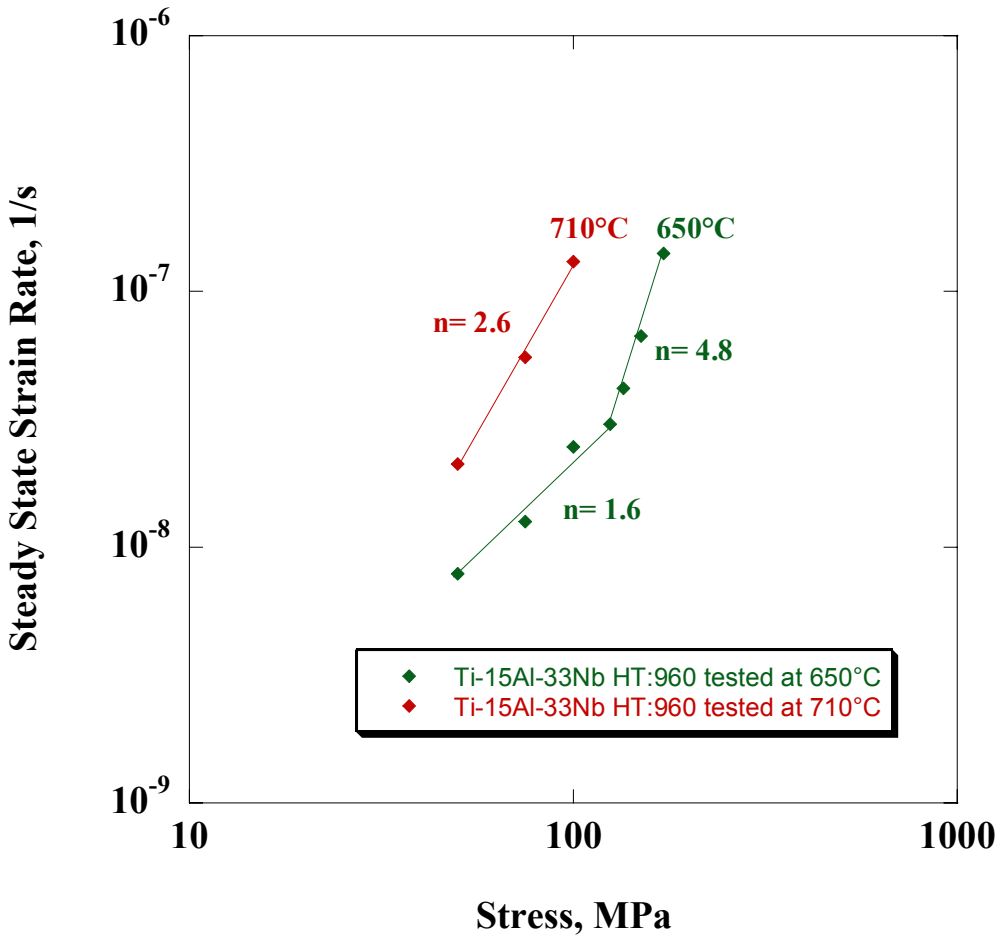

Figure 33. Plot of log $\dot{\varepsilon}_{ss}$ versus log σ for the Ti-15Al-33Nb HT:960 microstructure tested at 650°C and 710°C.

V. DISCUSSION

A. Microstructure Discussion

The goal of the phase evolution work performed in this study was three-fold. First, to quantify microstructural features such as grain size, phase volume fractions, and phase morphology then relate these features to mechanical properties and deformation behavior. The quantification of microstructural features has been presented in the microstructure results section, and the correlation to mechanical properties will be presented in the subsequent tensile and creep discussion sections. Second, to determine phase equilibria, and further modify the pseudobinary phase diagram based on TiAl and TiNb, for Ti = 50 at%, that was created by Bendersky *et al.*[10] and later modified by Boehlert *et al.*[12]. Third, to determine phase transformation mechanisms.

1. Phase Equilibria

The pseudobinary diagram first constructed by Bendersky *et al.*[10] and later modified by Boehlert *et al.*[12] is presented in Figure 34. From Figure 34 is it is evident that phase equilibria data is lacking between the compositions of Ti-23Al-27Nb and Ti-12Al-38Nb. The deficiencies in understanding that arise in this region of compositions are:

1. What is the Al concentration needed to induce ordering in the BCC phase, i.e. where does the β phase field end and where does the B2 phase field begin?
2. Do $\beta+\alpha_2$ and $\beta+\alpha_2+O$ phase fields exist?
3. What composition do the $B2+\alpha_2$ and the $B2+\alpha_2+O$ phase fields extend to?

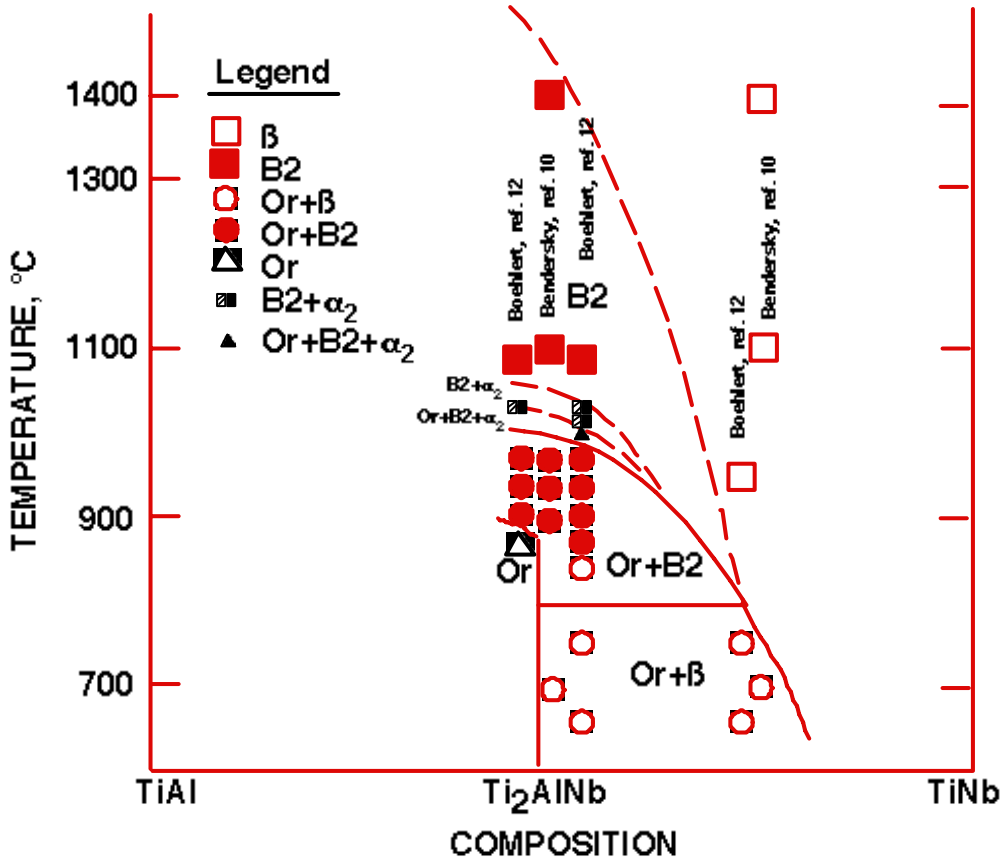

Figure 34. Pseudobinary diagram based on TiAl and TiNb, for Ti = 50 at%, first developed by Bendersky *et al.*[10] and further modified by Boehlert *et al.*[12].

One of the major motives in alloy selection for this work was to further develop the phase equilibria in this region of the diagram, so nominally Ti-17Al-33Nb and Ti-22Al-28Nb alloys were chosen. While the alloy compositions more closely resembled Ti-15Al-33Nb and Ti-21Al-29Nb from ICP-OES and IGF analysis, the results of this phase evolution study were still extremely beneficial in determining the phase equilibria between Ti-23Al-27Nb and Ti-12Al-38Nb. Figure 35 displays the pseudobinary diagram constructed with the results from the phase evolution study performed in this work added to the original pseudobinary diagram originally developed by Bendersky *et al.*[10]. From

Figure 35 it is evident that the proposed questions on the phase equilibria between Ti-23Al-27Nb and Ti-12Al-38Nb have been answered.

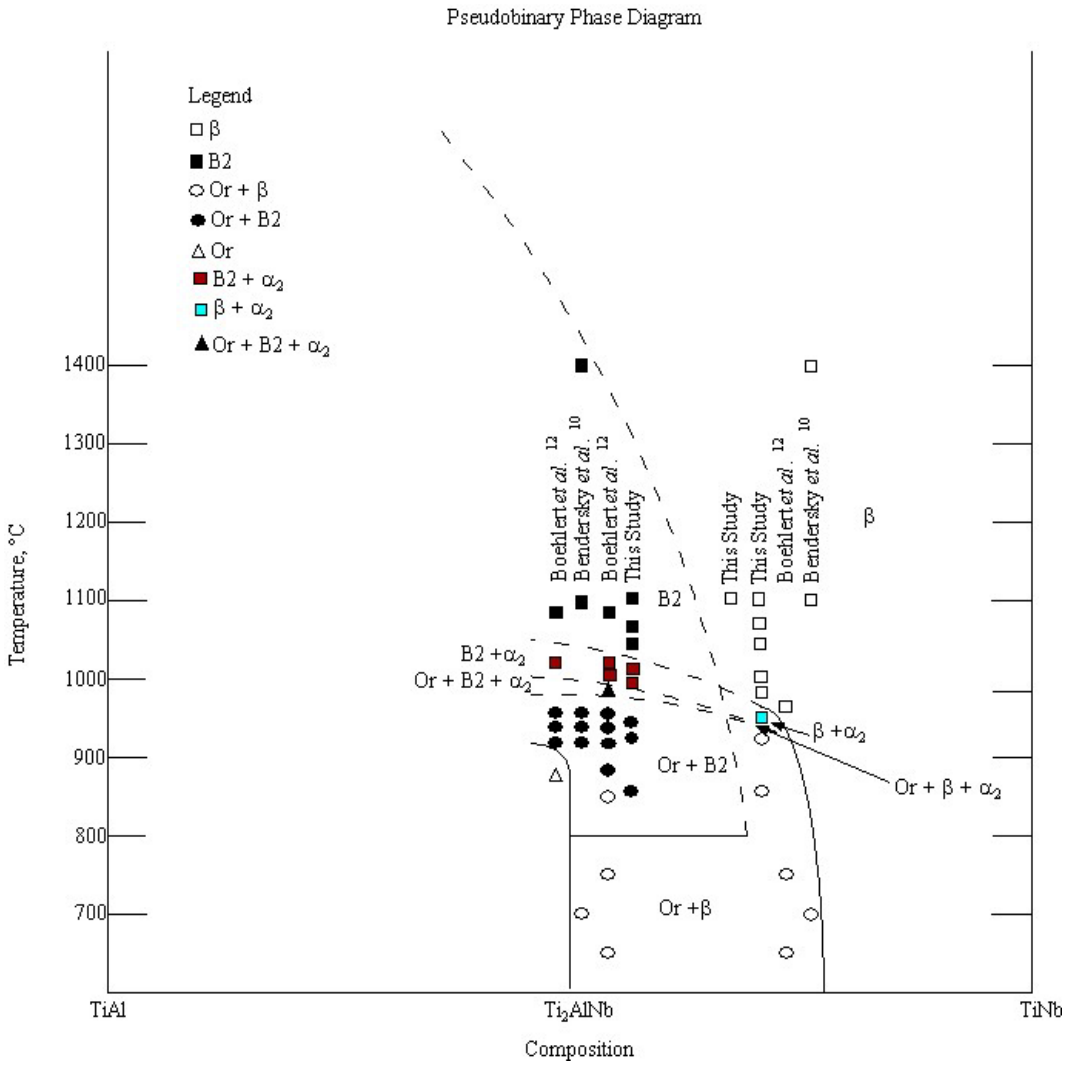

Figure 35. Pseudobinary phase diagram constructed by combining the results of this study with those of Bendersky *et al.*[10] and Boehlert *et al.*[12].

From XRD results, it was determined that the BCC phase of the Ti-21Al-29Nb HT:1075°C/3h/WQ microstructure is in fact ordered B2 due to the (210) superlattice reflection present in the diffraction pattern obtained for this microstructure. XRD results also revealed that BCC phase of the Ti-15Al-33Nb HT:1075°C/3h/WQ and Ti-16Al-33Nb HT:1105°C/3h/WQ microstructures was disordered β due to the lack of the superlattice (210) reflection in both diffraction patterns. From this it can be concluded that the B2 phase field border extends to at least 16 at% Al on the pseudobinary diagram, and the exact composition for which ordering of the BCC phase occurs lies between 16-21 at% Al.

From the phases present in BSE micrographs and the XRD pattern of the Ti-15Al-33Nb HT:960°C/3h/WQ microstructure, the existence of the $\beta+\alpha_2$ phase field has been confirmed. This phase field encompasses a narrow temperature range spanning ~960-980°C for Ti-15Al-33Nb. The temperature range for the $B2+\alpha_2$ phase field was determined to be ~ 980-1005°C for Ti-21Al-29Nb.

The temperature range for the $B2+\alpha_2+O$ phase field for Ti-23Al-27Nb was found to be 975-1000°C.[12] The 990°C/3h/WQ microstructures produced in this study, with the solutionizing temperature lying in the $B2+\alpha_2+O$ phase field for Ti-23Al-27Nb, produced a $B2+\alpha_2$ for Ti-21Al-29Nb and a fully β microstructure for Ti-15Al-33Nb. The existence of the $B2+\alpha_2+O$ and $\beta+\alpha_2+O$ phase fields has been included on the pseudobinary diagram but their existence for compositions below Ti-23Al-27Nb can only be speculated due to the fact that all subtransus solution treated and water-quenched microstructures possessed small volumes of the α_2 phase. Microstructures free of the α_2 phase were only produced through solution treatment above the β-transus. This is due to the sluggish diffusion kinetics of the α_2 phase, and the fact that the O phase will form a "rim" around the α_2 phase, further trapping it within the microstructure at temperatures below the β-transus. An example of "rim O phase" is depicted in Figure 36.

The presence of the α_2 phase in every subtransus microstructure is due to alloy processing. When the master alloys were melted and cast into ingot form, the ingot contained every constituent phase because the ingot was slow cooled from the melt through every phase field. Since both alloys were worked at subtransus temperatures, the

α_2 phase present in the ingot still remained after processing into sheet form. In addition, the Ti-21Al-29Nb ingot and sheets were processed at 982°C, which lies in the B2+α_2 phase field for this composition. If the B2+α_2+O and β+α_2+O phase fields do exist beyond 23 at% Al, their respective temperature ranges are extremely narrow. An important result of this work is that the α_2 phase is present in Ti-15Al-33Nb. To the author's knowledge this is the lowest Al containing Ti-Al-Nb alloy, for Ti ~50 at%, that contains the α_2 phase. In phase evolution work performed by Boehlert on a Ti-12Al-38Nb alloy, it was found that all thermomechanically processed Ti-12Al-38Nb microstructures contained no α_2 phase whatsoever.[12] Therefore, the Al concentration required to form the α_2 phase in Ti-Al-Nb alloys, for Ti ~ 50 at%, lies between 13-15 at% Al.

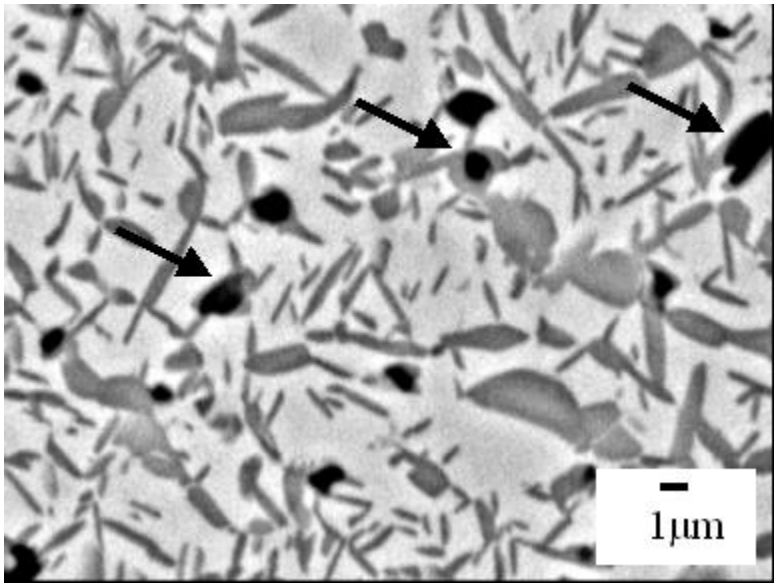

Figure 36. A Ti-21Al-29Nb HT:960/3h/WQ microstructure. The arrows depict the "rim O phase"(grey) surrounding the α_2 phase (black).

2. Phase Transformation Mechanisms

Only one phase transformation mechanism was observed for the microstructures produced in this study. This mechanism was conventional Widmanstatten precipitation of the α_2 and O phases from either the B2 or β BCC phases. Widmanstatten precipitation occurs when plate, or even needle-shaped precipitates grow in such a manner that they are aligned along specific crystallographic planes or directions of the matrix crystals. [2(p. 535)] The orientation relationship (OR) in which the α_2 phase grows from the parent B2 phase is the same OR found between the α and β phases in pure titanium which was described by Burgers.[42] This OR is $[11\text{-}20]\alpha_2//[1\text{-}11]B2$; $(0001)\alpha_2//(110)B2$. The OR between the O and B2 phases is $[1\text{-}11]B2//[110]O$; $(110)B2//(001)O$.[8] The α_2 phase had an equiaxed morphology in every heat treatment condition for both alloys. For Ti-15Al-33Nb, the O phase always occurred in a lath morphology, with the size and coarseness of the O laths increasing with increasing solutionizing temperature. This is apparent when comparing photomicrographs of the Ti-15Al-33Nb microstructures found in Figures 12 and 14 in the microstructure results section. For the HT:650/100h microstructure, the O lath width is estimated to be on the order of 50-100 nm and was only resolvable at magnifications on the order of 50,000x. For heat treatments performed at 855°C and above, O lath width is typically in the range of a few microns. For the Ti-21Al-29Nb microstructures, the O phase occurred in both lath and equiaxed morphologies. For solutionizing temperatures between 910-960°C the O phase occurs in both morphologies. For the 855°C/3h/WQ microstructure the O phase occurred only in a lath morphology. The temperature where this morphology change occurs lies somewhere between 855-910°C in the O+B2 phase field. An important point is that all aging heat treatments were performed at 855°C after furnace cooling from the solutionizing temperature. Had the samples been water-quenched from the solutionizing temperature and subsequently aged at lower temperatures, such as at 650°C, different phase transformation mechanisms would likely have occurred. These include a composition invariant transformation, found to occur below 800°C, and discontinuous precipitation of the α_2 and O phases which replaces fine intergranular matrix precipitation.[12]

B. Tensile Behavior Discussion

The focus of the tensile discussion section will be to draw insight into microstructure-tensile property relationships and where applicable, compare the tensile properties of the two Ti-Al-Nb alloys from this study with those of other studies.

1. Room Temperature Ductility

Table XVI presents the RT tensile properties of several orthorhombic Ti-Al-Nb alloys.

Table XVI. RT Tensile Properties of O + BCC Ti-Al-Nb Alloys

Alloy Composition [reference]	Heat Treatment	0.2%YS (MPa)	UTS (MPa)	ε_f (%)
Ti-15Al-45Nb[43]	1050/4h + 800°C/24h	865	924	15.1
Ti-22Al-23Nb[21]	1050°C/2h + 815°C/8h/FC	836	1111	14.8
Ti-22Al-24Nb[44]	815°C/4h	1257	1350	3.6
Ti-22Al-25Nb[45]	1000°C/1h/Ar + 815°C/2h/Ar	1245	1415	4.6
Ti-22Al-25Nb[45]	1125°C/1h/BC + 815°C/2h/Ar	1134	1175	0.9
Ti-22Al-27Nb[45]	815°C/1h/Ar	1294	1415	3.6
Ti-23Al-16Nb[19]	1050°C/1h/WQ + 850°C/2h/FC	691	906	14
Ti-23Al-23Nb[46]	760°C/100h	472	638	4
Ti-25Al-21Nb[3]	1050°C/1h/Ar + 815°C/2h/Ar	847	881	0.4
Ti-22Al-20Nb-5V[44]	815°C/24h + 760°C/100h	900	1161	18.8

WQ: water quench; FC: furnace cool; Ar: cooling performed in static argon gas; BC: brick cooled (1.5°C/sec); na: not available.

In general, the alloys in Table XV exhibit higher ε_f values with higher Nb contents and lower Al contents, which is consistent with the results of this study. For identical heat treatment conditions, the Ti-21Al-29Nb microstructures always exhibited lower ε_f values than the Ti-15Al-33Nb microstructures. This is due to the fact that the Ti-21Al-29Nb microstructures always contained less BCC phase by volume than the Ti-15Al-33Nb microstructures. Another important factor effecting ductility is that increasing the Al contents favors the formation of the O phase and induces the ordered B2 structure. Increasing the Nb content favors the formation of the disordered β structure (see Figure 35). Even if both alloys possessed equal volume fractions of each constituent phase, the same morphologies, and the same grain size, Ti-21Al-29Nb would still show lower ε_f values due to the fact the BCC phase in this alloy is the ordered B2 intermetallic phase. The highest RT ε_f value was shown by the AP Ti-15Al-33Nb microstructure which contained 90 Vp β. From this study, it can be concluded that most important microstructural factors that control room temperature ductility in this intermetallic system are BCC volume percent, and most importantly BCC structure. This is evidenced by the fact that the both as-processed microstructures contained only the BCC and α_2 phases and both had the same grain sizes; the AP Ti-21Al-29Nb microstructure contained 96 Vp B2 (ε_f = 1.7%), compared to 90 Vp β for AP Ti-15Al-33Nb (ε_f = 12.4%). In order for either of the alloys in this study to display adequate RT ductility, a sufficient volume of BCC phase in the microstructure is imperative with the β phase imparting significantly higher ductility to the microstructure than the B2 phase.

2. Grain Size Effects

Increasing the grain size significantly decreased the RT ε_f values of the supertransus heat-treated Ti-15Al-33Nb microstructures as shown in Table VIII in the tensile results section. Supertransus, large grained Ti-21Al-29Nb microstructures were not produced through heat-treatment due to the already poor ductility exhibited by the subtransus Ti-21Al-29Nb microstructures. At 650°C, increasing the grain size did not have any clearly deleterious effect on tensile properties

3. Orthorhombic Phase Strengthening

The effect of O volume fraction and morphology is shown for Ti-12Al-38Nb,[20] Ti-15Al-33Nb, Ti-21Al-29Nb, and Ti-25Al-24Nb[20] microstructures. Figure 37 depicts the RT tensile stress versus strain curves for the lower Al containing alloys and the RT tensile stress versus strain curves for the higher Al containing alloys is presented in Figure 38.

The Ti-15Al-33Nb microstructures all have higher strengths than the Ti-12Al-38Nb microstructures. The BCC phase for both compositions is disordered β and the O phase has a lath morphology. An important difference in these alloys is that the Ti-15Al-33Nb alloys contain small volumes of the α_2 phase, while the Ti-12Al-38Nb alloys only contain the O and β phases. The fully β Ti-12Al-38Nb microstructure exhibited greater ductility than the AP 0% O phase Ti-15Al-33Nb microstructure, but much lower strength. The increase in strength and loss of ductility of the Ti-15Al-33Nb microstructures is directed attributed to the larger O volume fraction of these microstructures. Bao has developed a finite element model that predicts the yield strength for a two-phase microstructure to be approximately 1.5 times larger than that of the single-phase β microstructure, assuming the O phase acts as rigid needles and taking into account their volume fraction and random orientation within the β grains.[48] This is in excellent agreement with the Ti-12Al-38Nb microstructures, as the fully β microstructure had a YS of 553MPa and the 28 Vp O + 72 Vp β microstructure had a YS of 809MPa. This model does not fit well for the Ti-15Al-33Nb microstructures, possibly due to the aging heat-treatments used to precipitate the O phase. The Ti-12Al-38Nb O + β microstructure was produced by solutionizing and water-quenching, followed by aging at 650°C and water-quenching. If an identical type of heat treatment was performed on the Ti-15Al-33Nb microstructures, similar trends may have been exhibited if the volume fraction of O phase was less than that of the β phase after this heat treatment.

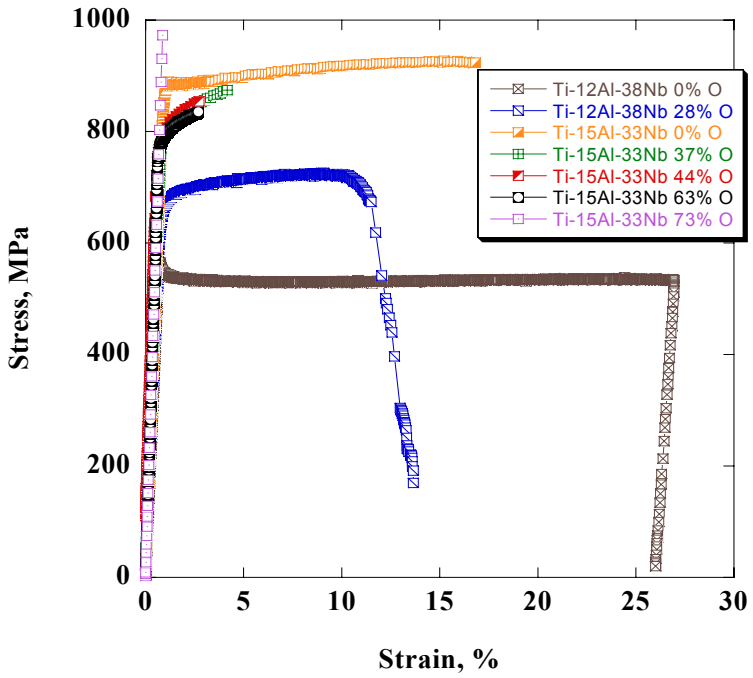

Figure 37. RT stress versus strain curves for Ti-12Al-38Nb and Ti-15Al-33Nb microstructures.

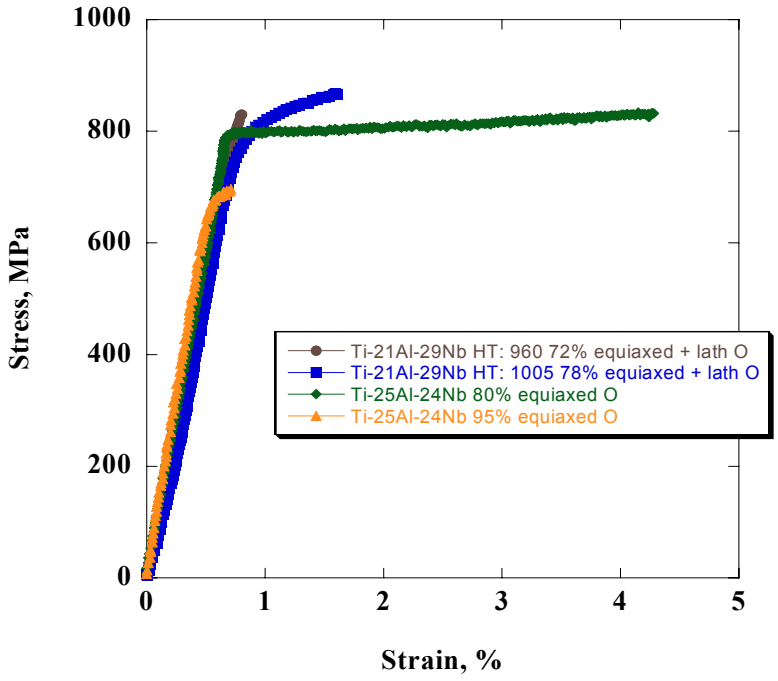

Figure 38. RT stress versus strain curves for Ti-21Al-29Nb and Ti-25Al-24Nb microstructures.

For almost equal O volume fractions, the Ti-25Al-24Nb microstructure displayed higher ε_f values and lower strength than the Ti-21Al-29Nb microstructure. This may be attributed to the difference in morphologies. An interesting point is that decreasing the O volume fraction in Ti-25Al-24Nb increased the strength and ε_f values, while the opposite occurred for Ti-21Al-29Nb.

4. Temperature Dependence of Yield Strength

BCC metals of commercial purity are characterized by a very strong temperature dependent component of the flow stress; the yield stress increases rapidly with decreasing temperature.[2(p.841)] All of the microstructures in this study displayed the behavior of yield stress decreasing with increasing temperature. In addition, the microstructures that did not have a yield stress at room temperature did at 650°C. Figure 39 is a plot of yield strength versus temperature for AP Ti-15Al-33Nb, AP Ti-21Al-29Nb, and several other Ti-Al-Nb O alloys.[20,45] The AP Ti-21Al-29Nb microstructure had the highest yield strength retention from RT to 650°C.

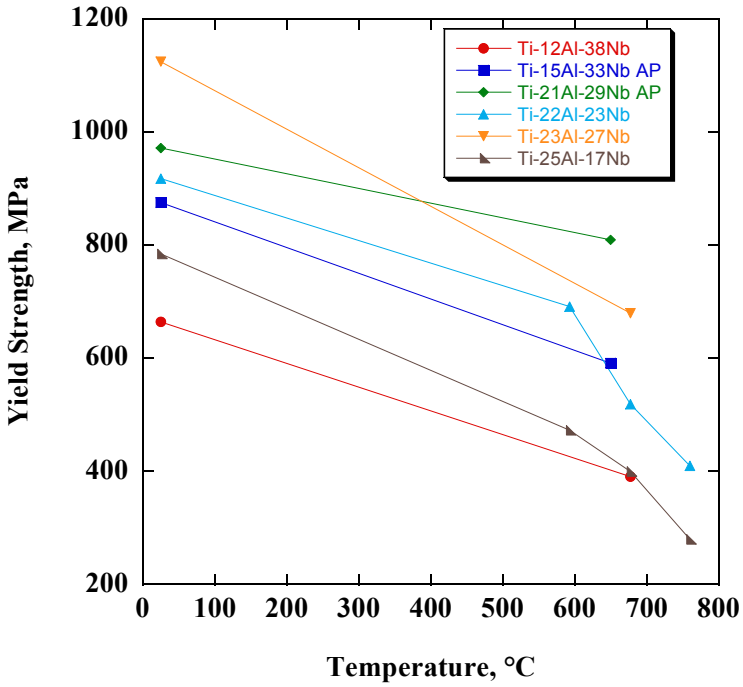

Figure 39. Yield strength versus temperature comparisons for Ti-Al-Nb alloys.

C. Creep Behavior Discussion

As with the tensile discussion section, the creep discussion section will focus on microstructure-creep property relationships of Ti-15Al-33Nb and Ti-21Al-29Nb, with applicable comparisons to the literature.

1. Phase Volume Fraction and Grain Size Effects

Increasing the O volume fraction within each alloy led to lower secondary creep rates for all microstructures, with the exception of the Ti-15Al-33Nb HT:650 microstructures. The poor creep resistance of the two HT:650 microstructures is attributed to the extremely fine grain size of these microstructures, which leads to increased area for grain boundary diffusion and accommodates the ease in which grain boundary sliding occurs.

The Ti-21Al-29Nb microstructures contained larger O phase volume fractions than all the identically heat-treated Ti-15Al-33Nb microstructures. This led to superior creep resistance of the Ti-21Al-29Nb HT:960 and HT:1005 microstructures over the Ti-15Al-33Nb HT:960 microstructure. However, both the supertransus heat-treated Ti-15Al-33Nb microstructures, HT:1005 and HT:1105, had superior creep resistance to the Ti-21Al-29Nb microstructures, although they contained less O phase by volume. It is speculated that supertransus Ti-21Al-29Nb microstructures would have superior creep resistance to all the microstructures tested in this study, due to increased grain size and increased O volume fractions. These microstructures were not pursued in this study due to the effort to produce microstructures with a balance of room temperature and elevated temperature properties. If produced, these microstructures would surely have lower RT ε_f values than the subtransus heat-treated microstructures, which already exhibit poor RT elongations. This statement is supported by the fact that the supertransus heat-treated Ti-15Al-33Nb microstructures displayed drastically lower RT elongations than the subtransus heat-treated Ti-15Al-33Nb microstructures.

From the log $\dot{\varepsilon}_{ss}$ versus log σ behavior it is apparent that grain size appears to be the dominant microstructural parameter governing the creep resistance of the microstructures studied. The two supertransus heat-treated microstructures, which had

the largest grain sizes, exhibited the best creep resistance. Both of these microstructures contained less O phase by volume than the Ti-15Al-33Nb HT:650 microstructure and both Ti-21Al-29Nb microstructures which is an important point, because larger O phase volumes tend to impart greater creep resistance. A key point emphasizing the effect of grain size on creep resistance is shown in the HT:650/100h microstructure. This microstructure contained 73 Vp O phase and exhibited the best 650°C tensile strength, which would lead to the assumption that this microstructure would have excellent creep resistance. Contrary to this first assumption, this microstructure had the worst creep resistance of all the microstructures creep tested, and is most likely due to the fact that the grain size for this microstructure was 4 μm. A graph of creep strain versus time for microstructures initially loaded at 172 MPa at 650°C is presented in Figure 40. Average equiaxed grain size is also displayed for each microstructure. From this plot it is evident that under the same testing conditions, increasing the average equiaxed grain size up to 120 μm is increasing the creep resistance of these microstructures. Evidence of increasing the grain size above 120 μm having a beneficial effect on creep resistance for the Ti-15Al-33Nb microstructures was shown at 275 MPa for temperatures between 650-690°C. At this stress and temperature range, the HT:1105 microstructure had lower steady-state strain rates than the HT:1005 microstructure.

From the results obtained, grain size is the microstructural parameter overwhelming influencing the creep behavior of these alloys. The Ti-15Al-33Nb HT:1005 (d = 120μm, 37Vp O) microstructure had a steady state creep rate of 7.6E-9 s^{-1} at 172 MPa/650°C. The Ti-15Al-33Nb HT:960 (d = 6 μm, 44 Vp O) microstructure had a steady state creep rate of 7.87E-9 s^{-1} at 50 MPa/650°C. It is proposed that the subtransus heat-treated microstructures transitioned to the dislocation climb controlled high stress creep regime at 100 MPa, 125 MPa, 100 MPa, and 125 MPa for Ti-15Al-33Nb HT:650/250h, Ti-15Al-33Nb HT:960, Ti-21Al-29Nb HT:960, and Ti-21Al-29Nb HT:1005 microstructures at 650°C, respectively. At 650°C, the proposed transition to the dislocation climb regime did not occur until a stress level of 225 MPa for the Ti-15Al-33Nb HT:1005 microstructure.

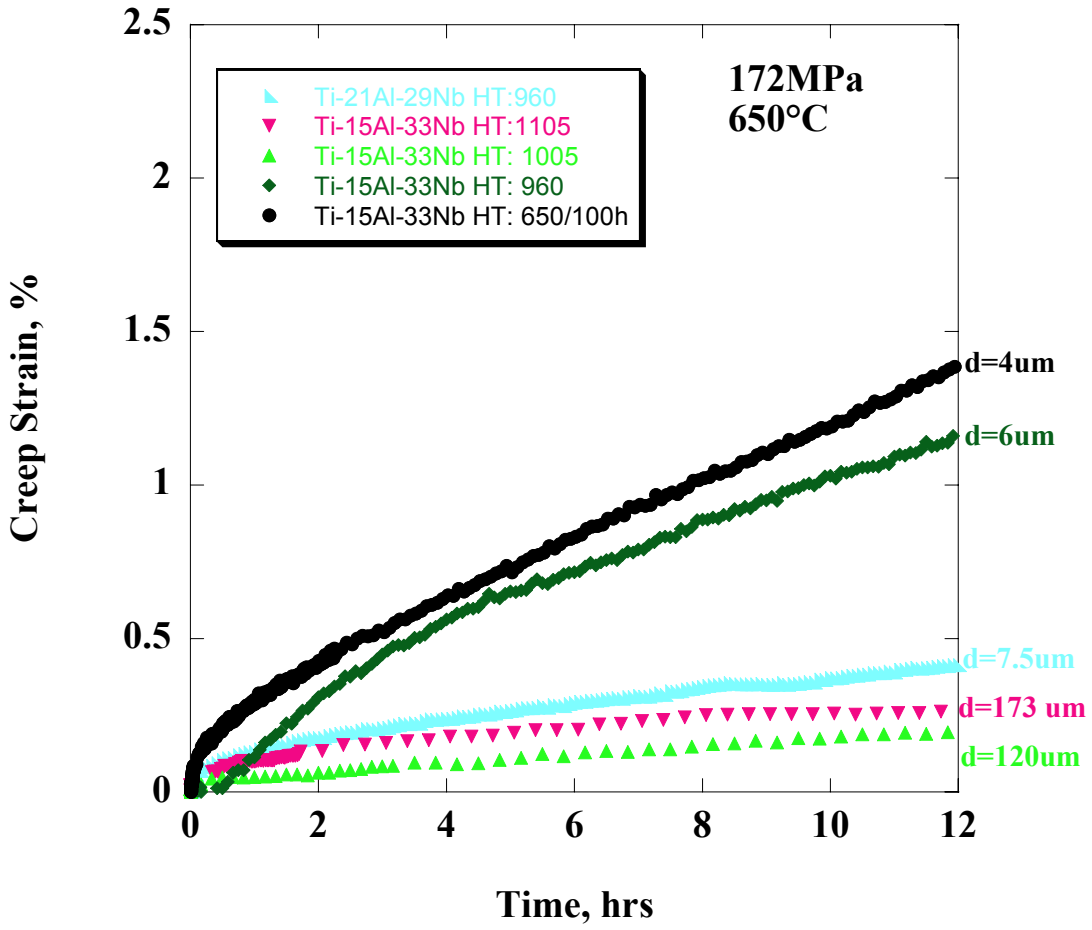

Figure 40. Creep strain versus time for microstructures initially loaded at σ = 172 MPa and T = 650°C.

2. Alloy Comparisons and Deformation Mechanism Map Construction

Table XVII lists creep properties for several α, α_2, and O based titanium alloys along with the alloys from this study. In the low-stress regime, both Ti-21Al-29Nb microstructures had significantly higher activation energies than the comparison alloys, and higher activation energies typically indicate greater secondary creep resistance. It is important to note that the comparison alloys had lower n values, and activation energies typically observed for Coble creep, while the Ti-21Al-29Nb microstructures had n values and activation energies that are suggesting grain boundary sliding or N-H deformation.

In the low-stress regime, the alloys in this study are exhibiting different deformation characteristics than other titanium alloys.

In the intermediate stress regime, the Ti-15Al-33Nb alloys have n values of the same order as the comparison alloys, but much lower activation energies. If grain boundary sliding is the dominant deformation mechanism in this stress regime, the alloys in this study illustrate worse resistance to grain boundary sliding than the referenced alloys.

With the exception of the Ti-15Al-33Nb HT:1005 microstructure, the n values determined in the high stress regime are in the same range as the reference alloys. The high-stress regime for the alloys in this study initiates at approximately the same stress level as the Ti_3Al, Ti-24Al-11Nb, Ti-24Al-16Nb, and the Ti-12Al-38Nb alloys. The Ti-27Al-21Nb, Ti-27Al-16Nb, Ti-22Al-27Nb, and Ti_2AlNb alloys transition to dislocation climb controlled creep at higher stresses than those suggested for the Ti-15Al-33Nb and Ti-21Al-29Nb alloys. In the high-stress regime, the alloys in this study are showing superior creep resistance to the α_2-based alloys and a higher activation energy.

The log $\dot{\varepsilon}_{ss}$ versus log σ behavior at 650°C of the most creep resistant O alloys is depicted in Figure 41 and includes the data from the most creep resistant microstructures in this study.[49,50,51] From this graph it is evident that the Ti-26Al-27Nb alloy has superior creep resistance to the Ti-15Al-33Nb, Ti-22Al-27Nb, and Ti-25Al-23Nb alloys. This alloy was processed using Induction Float Zone Melting (IFZM) to produce a highly textured microstructure with large O lath crystals. The effect of IFZM processing on the creep behavior of Ti-15Al-33Nb and Ti-21Al-29Nb would constitute very interesting future work.

Table XVII. Comparison of Creep Parameters for α, α2 and O-based Ti-Alloys

Alloy Composition [reference]	Heat Treatment	Test Conditions σ(MPa)/Temp(°C)	n	Qapp, kJ/mol
Low-Stress Regime				
Ti[51] α	various	1-2/550-865	1	104-121
Ti-24Al-11Nb[25] α_2	various	50-100/575-725, air	1	107-120
Ti-21Al-22Nb[52]	na	30-90/650-760, air	1.4	na
Ti-22Al-23Nb[53]	na	69-110/650, air+vacuum	1.3	187
Ti_2AlNb[54]	1090°C/0.5h/WQ +650°C/112h/WQ	50-172/650-760, air	1.2	171
Ti-12Al-38Nb[55]	various	50-135/650-705, air	1.6-1.9	127-178
Ti-15Al-33Nb [present study]	HT:960	50-125/650-710, air	1.6	115
Ti-21Al-29Nb [present study]	HT:960	50-100/650-710, air	2.1	292
Ti-21Al-29Nb [present study]	HT:1005	50-125/650-710, air	2.8	215
Intermediate-Stress Regime				
Ti-22Al-23Nb[56]	996°C/1hr/AQ 815°C/1hr	69-172/650-760, air+argon	2.8	327
Ti-25Al-23Nb[49]		175-310/650, argon	2.8	na
Ti_2AlNb[54]	various	50-352/650-760, air+vacuum	1.8-2.3	265
Ti-12Al-38Nb[55]	1200°C/5h/WQ + 650°C/53h/WQ	50-135/650-705 air+vacuum	1.9	256
Ti-15Al-33Nb [present study]	HT:1005	150-250/650-710, air	2.5	163
Ti-15Al-33Nb [present study]	HT:1105	150-250/650-710, air	3.1	181
High-Stress Regime				
Ti[51] α	various	1-2/550-865	4.3	241
Ti_3Al[40] α_2	1000°C/4h/FC	138-312/650-800	4.3	206
Ti-24Al-11Nb[25] α_2	various	100-400/575-725, air	5	260
Ti-27Al-21Nb[48]	1170°C/OQ + 900°C/AQ	240-500/650-750, air	5-6	340
Ti-24Al-16Nb[57]	1150°C/2.5°C/s + 750°C/AQ	150-540/700-750, air	4.2-4.3	371
Ti-27Al-16Nb[57]	1170°C/2.5°C/s + 750°C/AQ	240-660/700-750, air	4.2-4.3	376
Ti-22Al-27Nb[49]	815°C/1hr	310-380/650, argon	5.3	na
Ti_2AlNb[54]	various	317-442/650-760, air	3.7-5.1	346
Ti-12Al-38Nb[55]	various	135-172/650-705, air	3.5-7.2	na
Ti-15Al-33Nb [present study]	HT:960	125-172/650-710, air	4.8	na
Ti-15Al-33Nb [present study]	HT:1005	225-275, 650-710, air	6.0	288
Ti-21Al-29Nb [present study]	HT:960	100-172, 650-710 air	4.8	na
Ti-21Al-29Nb [present study]	HT:1005	125-250, 650-710, air	4.1	na

AQ: air quench; OQ: oil quench; FC: furnace cooled; Ar: cooling performed in static argon gas; na: not available

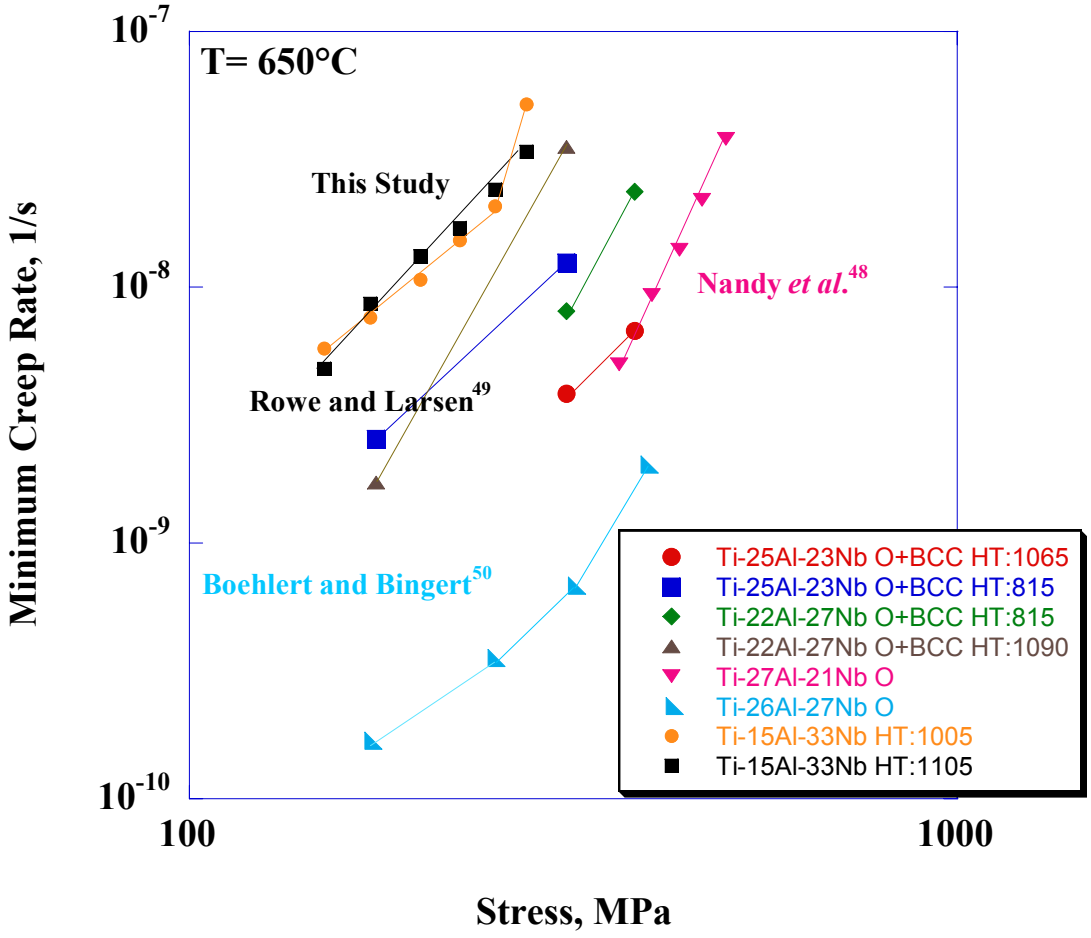

Figure 41. The log $\dot{\varepsilon}_{ss}$ versus log σ behavior of the most creep resistant Ti-Al-Nb alloys.

Deformation mechanism maps are extremely useful tools for determining the active deformation mechanism at a given stress, temperature, and grain size. Several examples of well developed deformation mechanism maps are available in the literature.[31] These maps are very useful for component designers that want to know how their material will deform for a given stress, temperature, and grain size.

A deformation mechanism map has been constructed by Ruano *et al.*[58] based on a constant homologous temperature and varying grain size.[58] The microstructures studied in this work have been superimposed onto this map in Figure 43. This map was constructed from creep data on pure metals with an assumed dislocation density of 10^8 m^{-2} and the subscripts L and P denote lattice and pipe diffusion, respectively. The burger's vector used for the data from this study was 0.299 nm[54] and the elastic moduli used were determined from the 650°C stress versus strain curves.

The Ti-15Al-33Nb HT:960 microstructure and both Ti-21Al-29Nb microstructures have stress and d values lying in the grain boundary sliding regime, which fits predicted low stress regime deformation mechanisms for the Ti-21Al-29Nb microstructures. The supertransus heat-treated microstructures exhibited data points lying in the slip due to pipe diffusion regime, which does not fit the predicted deformation mechanisms over the stress range of 150-275 MPa. The boundaries for the regimes on this map were constructed from data obtained for pure metals and equations that model specific types of deformation behavior, which accounts for the discrepancies. As a first approximation at modeling the creep deformation behavior, the experimental results obtained from this study appear to follow some of the same trends as those of pure metals. A main goal of the continuation of this research will be to fully define the boundaries of the deformation mechanism regimes and construct a full deformation mechanism map for these Ti-Al-Nb alloys.

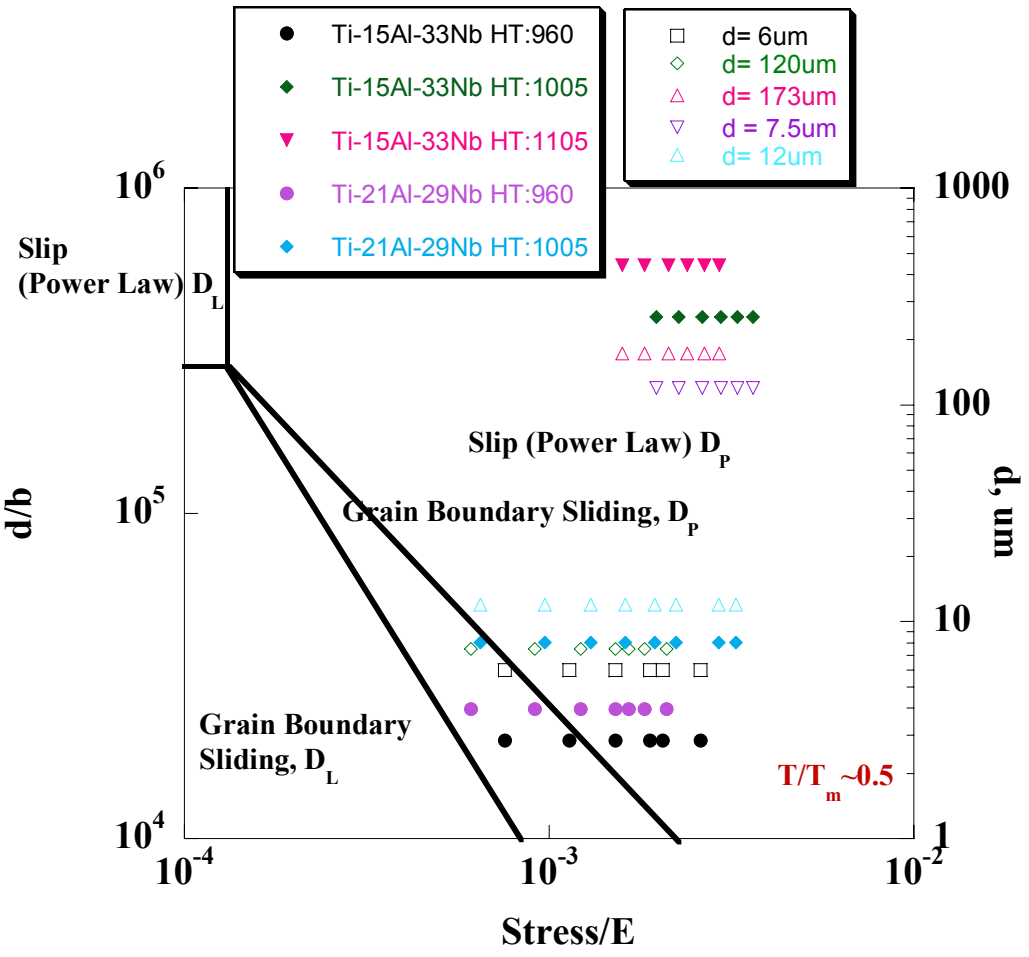

Figure 42. Deformation map developed by Ruano *et al*.[58] with data from this study overlaid.

VI. SUMMARY AND CONCLUSIONS

This section is comprised of a summary of the work performed in this study and the most important conclusions for the microstructural evolution, tensile, and creep behavior of Ti-15Al-33Nb and Ti-21Al-29Nb alloys.

A. Summary

This work was a systematic study of the physical metallurgy of Ti-15Al-33Nb and Ti-21Al-29Nb orthorhombic Ti-Al-Nb alloys. The focus was to determine processing-microstructure-property relationships for these yet-to-be characterized alloys and evaluate what potential either has for use as monolithic structural materials, and also as matrix materials in metal-matrix composites.

The subtransus processing of both alloys allowed a wide variety of microstructures to be produced via post-processing heat treatment. In particular, subtransus processing provided the ability to control grain size, and produce both fine-grained and course-grained microstructures. Ti-15Al-33Nb was easier to hot forge and hot roll below the β-transus due to the lower Al content and lower yield stress compared to Ti-21Al-29Nb. The Ti-21Al-29Nb cracked extensively during hot forging, but these cracks were eliminated after hot rolling and annealing.

The solution treatment study and XRD analysis results provided significant insight into the phase equilibria between the compositions of Ti-23Al-27Nb and Ti-12Al-38Nb and the pseudobinary diagram was modified accordingly. Each alloy was found to contain all three of the constituent phases (α_2, O, and BCC), and Ti-15Al-33Nb is the lowest Al concentration Ti-Al-Nb alloy to contain the α_2 phase for a Ti concentration of ~ 50 at%. Phase volume fractions in each alloy can be widely varied through heat treatment to obtain desired properties. The BCC phase in Ti-15Al-33Nb was confirmed to be disordered β and intermetallic ordered B2 in Ti-21Al-29Nb. The existence of the $\beta+\alpha_2$ phase field was confirmed. Grain size varied widely with heat treatment and did not rapidly increase until temperatures above the β-transus.

The room temperature and 650°C tensile properties of both alloys were determined. The AP Ti-15Al-33Nb microstructure displayed the best balance of RT

tensile properties and the HT:650/100h Ti-15Al-33Nb microstructure displayed the best 650°C tensile properties. At RT, all Ti-21Al-29Nb microstructures displayed poor ductility ($2.0\% < \varepsilon_f < 0.8\%$). Increasing grain size tended to decrease RT ε_f values, but had little effect on RT strength for the heat-treated microstructures. At 650°C, the yield strength of all microstructures decreased, and the microstructures that did not yield or strain harden at RT did at 650°C. The ductility of all microstructures increased at 650°C, with the largest increase occurring in microstructures possessing a high O volume fraction. A significant volume of BCC phase is necessary for RT ductility in both alloys.

The creep behavior in the stress range of 50-275 MPa and temperature range of 650-710°C was evaluated. Coble creep, grain boundary sliding, and dislocation climb were suggested to be the potentially dominant deformation mechanisms for the stresses and temperatures examined. The supertransus solutionized and aged microstructures provided the best creep resistance due to large grain size and a high O volume fraction, with grain size being the microstructural feature dominating the secondary creep behavior of these microstructures. Considerable further work is needed in confirming the deformation mechanisms predicted by n and Qapp values determined in this study. In particular, TEM investigations of the dislocation structures is necessary for specimens subjected to creep in the stress and temperature ranges were these deformation mechanisms are predicted to occur. In order to confirm grain boundary sliding, creep tests need to be performed in an inert or vacuum atmosphere on metallographically polished specimens marked with fiducial scratches. This will allow surface observations of grain boundary sliding and any accompanying cracking and/or cavitation.

B. Conclusions

1. Processing

- Subtransus processing allows control of microstructural features such as morphology and grain size that cannot be achieved with supertransus processing
- Ti-15Al-33Nb possesses higher workability and machinability than Ti-21Al-29Nb due to a lower Al content and lower yield stress

2. Microstructural Evolution

- The BCC phase was confirmed to be disordered β in Ti-15Al-33Nb and Ti-16Al-33Nb and ordered intermetallic B2 in Ti-21Al-29Nb from XRD
- A higher Al content and lower Nb content causes the formation of more O phase by volume and induces the ordering of β to B2. The composition where the order/disorder transition occurs lies between 16-21 at% Al
- The β-transus was 980°C for Ti-15Al-33Nb and 1040°C for Ti-21Al-29Nb
- For all solution treated and quenched microstructures, Ti-21Al-29Nb contained a larger O volume fraction that Ti-15Al-33Nb due to the higher Al content
- The $\beta+\alpha_2$ phase field exists for a temperature range of ~ 960-980°C
- Ti-15Al-33Nb is the Ti-Al-Nb alloy, containing Ti ~ 50 at%, with the lowest Al concentration that the α_2 phase has been observed in. The Al concentration needed to form the α_2 phase lies between 13-15 at% Al
- If the three phase $B2+\alpha_2+O$ and $\beta+\alpha_2+O$ phase fields exist between 23-15 at% Al, they encompass an extremely narrow temperature range
- Widmanstatten precipitation of the α_2 and O phases from parent B2 or β was the only phase transformation mechanism observed for these alloys
- The O phase can occur in lath or equiaxed morphology in Ti-21Al-29Nb, depending on temperature, but only lath O phase was observed in Ti-15Al-33Nb
- Rapid grain growth only occurs for microstructures solutionized above the β-transus

- The activation energy for B2 grain growth in Ti-21Al-29Nb is 311 kJ/mol and the activation energy for β grain growth in Ti-15Al-33Nb is 194 kJ/mol
- The addition of up to 15 at% Al in TiNb does not hinder grain growth kinetics

3. Tensile Behavior

- The AP Ti-15Al-33Nb microstructure displayed the best balance of RT tensile properties due to a high β volume fraction and fine grain size
- The HT:650/100h Ti-15Al-33Nb microstructure had the best 650°C tensile properties due to its high O volume fraction and fine grain size
- Large grained heat-treated microstructures had significantly lower ductility at RT than fine grained heat-treated microstructures
- Yield strength decreased and ductility increased for all microstructures with increasing temperature
- BCC volume fraction and structure are the microstructural features that control ductility in this intermetallic system at RT

4. Creep Behavior

- All microstructures exhibit the primary, secondary, and tertiary stages of creep
- The supertransus solutionized and aged Ti-15Al-33Nb microstructures exhibited the best creep resistance for the stress and temperature range studied
- Coble creep and grain boundary sliding were suggested to be the deformation mechanisms in the low and intermediate stress regime at 650°C
- Dislocation climb was suggested to be the deformation mechanism in the high stress regime at 650°C
- Grain size appears to be the dominant microstructural parameter influencing the secondary creep behavior of these alloys. Increasing the grain size increases the creep resistance

5. Evaluation

- Ti-15Al-33Nb HT:1005 and HT:1105 microstructures show the best balance of room temperature and elevated temperature properties
- Ti-15Al-33Nb and Ti-21Al-29Nb merit further evaluation for high temperature aerospace applications
- Ti-15Al-33Nb merits further evaluation for both RT and ET applications as a monolithic structural material and as a matrix material in metal matrix composites

REFERENCES

1. M. Peters, J. Hemptenmacher, J. Kumpfert, and C. Leyens, "Structure and Properties of Titanium and its Alloys," pp. 1-8 in *Titanium and Titanium Alloys*. Edited by C. Leyens and M. Peters. Wiley-VCH Verlag, Weinheim, Germany, 2003.

2. R.E. Reed-Hill and R. Abbaschian, *Physical Metallurgy Principles*, 3rd ed. PWS Publishing Company, Boston, MA, 1994.

3. D. Banerjee, A.K. Gogia, T.K. Nandy, and V.A. Joshi, "A New Ordered Orthorhombic Phase in a Ti_3Al-Nb Alloy," *Acta Metall.*, **36** [4] 871-82 (1988).

4. B. Mozer, L.A. Bendersky, W.J. Boettinger, and R.G. Rowe, "Neutron Powder Diffraction Study of the Orthorhombic Ti_2AlNb Phase," *Scr., Metall. Mater.*, **24** [12] 2363-68 (1990).

5. K. Muraleedharan, D. Banerjee, S. Banerjee, and S. Lele, "The α_2-to-O Transformation in Ti-Al-Nb Alloys," *Philos. Mag. A,* **71** [5] 1011-36 (1995).

6. K. Muraleedharan, S.V. Nagender, and D. Banerjee, "Orthorhombic Distortions of the α_2 Phase in Ti_3Al-Nb Alloys: Artifacts and Facts," *Scr. Metall. Mater.*, **24** [1] 27-32 (1990).

7. K. Muraleedharan, A.K. Gogia, T.K. Nandy, D. Banerjee, and S. Lele, "Transformations in a Ti-24Al-15Nb Alloy: Part I. Phase Equilibria and Microstructure," *Metall. Trans. A*, **23** [2], 401-15 (1992).

8. K. Muraleedharan, T.K. Nandy, D. Banerjee, and S. Lele, "Transformations in a Ti-24Al-15Nb Alloy: Part II. A Composition Invariant $\beta_o \rightarrow$O Transformation," *Metall. Trans. A.*, **23** [2] 417-31 (1992).

9. K. Muraleedharan, T.K. Nandy, D. Banerjee, "Phase Stability and Ordering Behaviour of the O Phase in Ti-Al-Nb Alloys," *Intermetallics*, **3** [3] 187-99 (1995).

10. L.A. Bendersky, W.J. Boettinger, and A. Roytburd, "Coherent Precipitates in the BCC/Orthorhombic Two-Phase Field of the Ti-Al-Nb System," *Acta Metall. Mater.,* **39** [8] 1959-69 (1991).

11. L.A. Bendersky and W.J. Boettinger, "Transformation of BCC and B2 High Temperature Phases to HCP and Orthorhombic Structures in the Ti-Al-Nb System. Part II. Experimental TEM Study of Microstructures," *J. Res. Natl. Inst. Stand. Technol.*, **98** [5] 585-606 (1993).

12. C.J. Boehlert, B.S. Majumdar, V. Seetharaman, and D.B. Miracle, "Part I. The Microstructural Evolution in Ti-Al-Nb O+BCC Orthorhombic Alloys," *Metall. Trans. A*, **30** [9] 2305-23 (1999).

13. J. Peng, Y. Mao, S. Li, and X. Sun, "Microstructure Controlling by Heat Treatment and Complex Processing for Ti_2AlNb Based Alloys," *Mater. Sci. Eng., A*, **299** [1-2] 75-80 (2001).

14. H. Garmestani and G.C. Branco, "Polycrystal Plasticity Theory" (2004) Carnegie Mellon University. Accessed on: October 2004. Available at (http://neon.mems.cmu.edu/rollett/27750.old.Spg02/Polycrystal_plasticity_rev3 ppt).

15. A.K. Gogia, T.K. Nandy, K. Muraleedharan, and D. Banerjee, "The Effect of Heat Treatment and Niobium Content on the Room Temperature Tensile Properties and Microstructure of Ti_3Al-Nb Alloys," *Mater. Sci. Eng., A*, **159** [1] 73-86 (1992).

16. C.J. Boehlert, B.S. Majumdar, and D. Eylon, "Properties and Damage Mechanisms in Three Classes Titanium Composite Matrices," *Key Eng. Mater.*, **127-131** [1] 843-50 (1997).

17. D. Banerjee, "Deformation of the O and α_2 Phases in the Ti-Al-Nb System," *Philos. Mag. A*, **72** [6] 1559-87 (1995).

18. B.S. Majumdar, C.J. Boehlert, A.K. Rai, and D.B. Miracle, *High Temperature Ordered Intermetallic Alloys-VI*, Vol. 364, pp.1259-1265, Edited by J. Horton, I. Baker, S. Hanada, R. D. Noebe, and D. S. Schwartz, Materials Research Society, Pittsburgh, PA 1995.

19. C.J. Boehlert, B.S. Majumdar, S. Krishnamurthy, and D. B. Miracle, "Role of Matrix Microstructure on RT Tensile Properties and Fiber-Strength Utilization of an Orthorhombic Ti-alloy Based Composite," *Metall. Trans. A*, **28** [2] 309-23 (1997).

20. C.J. Boehlert, "Part III. The Tensile Behavior of Ti-Al-Nb O+BCC Orthorhombic Alloys," *Metall. Trans. A*, **32** [8] 1977-88 (2001).

21. P.R. Smith, J.A. Graves, and C.G. Rhodes, "Comparison of Orthorhombic and Alpha-Two Titanium Aluminides as Matrices for Continuous SiC-Reinforced Composites," *Metall. Trans. A*, **25** [6] 1267-83 (1994).

22. G.E. Dieter, *Mechanical Metallurgy*, 3rd ed; p. 448. McGraw-Hill, Boston, MA, 1986.

23. D. Eylon, J.A. Hall, C.M. Pierce, and D.L. Ruckle, "Microstructure and Mechanical Properties Relationships in the Ti-11 Alloy at Room and Elevated Temperatures," *Metall. Trans. A*, **7** [12] 1817-26 (1976).

24. W.H. Miller, R.T. Chen, and E.A. Starke, "Microstructure, Creep, and Tensile Deformation in Ti-6Al-2Nb-1Ta-0.8Mo," *Metall. Trans. A*, **18** [8] 1451-68 (1987).

25. R.S. Mishra and D. Banerjee, "Microstructure and Steady State Creep in Ti-24Al-11Nb," *Mater. Sci. Eng., A*, **130** [2] 151-64 (1990).

26. R.S. Mishra, D. Banerjee, and A.K. Mukherjee, "Primary Creep in a Ti-25Al-11Nb Alloy," *Mater. Sci. Eng., A*, **192-193** [2] 756-62 (1995).

27. B.D. Worth, W. Jones, and J.E. Allison, "Creep Deformation in Near-γ TiAl: II. Influence of Carbon on Creep Deformation in Ti-48Al-1V-0.3C," *Metall. Trans. A*, **26** [11] 2947-59 (1995).

28. R.W. Evans and B. Wilshire, *Creep of Metals and Alloys*. The Institute of Metals, New York, NY, 1985.

29. C. Herring, "Diffusional Viscosity of a Polycrystalline Solid," *J. Appl. Phys.*, **21** [5] 437-45 (1950).

30. R.L. Coble, "A Model for Boundary Diffusion Controlled Creep in Polycrystalline Materials," *J. Appl. Phys.*, **34** [6] 1679-82 (1963).

31. R.W. Hertzberg, *Deformation and Fracture Mechanics of Engineering Materials*, 4th ed; pp. 181-201. John Wiley and Sons, New York, NY 1996.

32. J.E. Hilliard, "Estimating Grain Size by the Intercept Method," *Met. Prog.,* **78** [5] 99-100 (1964).

33. "Standard Test Methods for Determining Average Grain Size," ASTM Designation E112-96e3. American Society for Testing and Materials, West Conshohocken, PA.

34. R.R. Boyer, "Titanium and Titanium Alloys," pp. 460 in ASM Handbook, Vol. 9, *Metallography and Microstructures*. Edited by K. Mills, J.R. Davis, J.D. Destfani, D.A. Dieterich, G.M. Crankovic, H.J. Frissell, D.M. Jenkins, W.H. Cubberly, and R.L. Stedfeld. ASM International, Materials Park, OH, 1985.

35. A.K. Gogia, T.K. Nandy, D. Banerjee, T. Carisey, J.L. Strudel, and J.M. Franchet, "Microstructure and Mechanical Properties of Orthorhombic Alloys in the Ti-Al-Nb System," *Intermetallics*, **6** [7-8] 741-48 (1998).

36. M. James, Data Sheet, Ti-22Al-23Nb Diffraction Peaks. Rockwell Science Center, Thousand Oaks, CA, 1994.

37. H. Hu and B.B. Rath, "On the Time Exponent in Isothermal Grain Growth," *Metall. Trans.*, **1** [11] 3181-84 (1970).

38. V. Seetharaman and S.L. Semiatin, "Plastic Flow and Microstructure Evolution During Hot Deformation of a Gamma Titanium Aluminide Alloy," *Metall. Trans. A*, **28** [11] 947-54 (1997).

39. G.T. Higgins, S. Wiryolukito, and P. Nash, *Grain Growth in Polycrystalline Materials*. Edited by G. Abbruzzese and P. Brozzo. Trans Tech Publications, Aedermannsdorf, Switzerland, 1992.

40. P.G. Shewmon, *Diffusion in Solids*; pp. 61-94. McGraw-Hill, New York, NY 1963.

41. F. Popille and J. Douin, "The Dislocation Microstructure in Orthorhombic Ti_2AlNb Deformed Between Room Temperature and 800°C," *Philos. Mag. A*, **73** [5] 1401-18 (1996).

42. W.G. Burgers, "On the Process of Transition of the Cubic-Body-Centered Modification into the Hexagonal-Close-Packed Modification of Zirconium," *Physica* (Amsterdam), **1** [7] 561-86 (1934).

43. C.M. Austin, J.R. Dobbs, H.L. Fraser, D.G. Konitzer, D.J. Miller, M.J. Parks, J.C. Schaeffer, and J.W. Sears, "Rapidly Solidified Oxidation Resistant Niobium Base Alloys," WL-TR-93-4059, GE Aircraft Engines, Cincinnati, OH, 1992.

44. R.G. Rowe, *Titanium '92 Science and Technology*, Vol. 1, pp. 343-350. Edited by F.H. Froes and I. Caplan. The Minerals, Metals, and Materials Society, Warrendale, PA, 1993.

45. R.G. Rowe, D.G. Konitzer, A.P. Woodfield, and J.C. Chesnutt, *High Temperature Ordered Intermetallic Alloys-IV*, Vol. 231, pp. 703-708, Edited by L.A. Johnson, D.P. Pope, and J.O. Stiegler, Materials Research Society, Pittsburgh, PA, 1991.

46. F.C. Dary and T.M. Pollock, "Effects of High Temperature Air and Vacuum Exposures on the Room Temperature Tensile Behavior of the (O+B2) Titanium Aluminide Ti-22Al-23Nb," *Mater. Sci. Eng., A*, **208** [2] 188-202 (1996).

47. G. Bao, J.W. Hutchinson, and R.M. McMeeking, "Particle Reinforcement of Ductile Matrices Against Plastic Flow and Creep," *Acta Metall. Mater.*, **39** [8] 1871-82 (1991).

48. T.K. Nandy, R.S. Mishra, and D. Banerjee, "Creep Behaviour of an Orthorhombic Phase in a Ti-Al-Nb Alloy," *Scr. Metall. Mater.*, **28** [5] 569-74 (1993).

49. R.G. Rowe and M. Larsen, *Titanium 1995*, Vol. 1, pp. 364-371. Edited by P.A. Blenkinsop, W.J. Evans, and H.M. Flowers. The University Press, Cambridge, UK, 1996.

50. C.J. Boehlert and J.F. Bingert, "Microstructure, Tensile, and Creep Behavior of O+BCC Ti_2AlNb Alloys Processed Using Induction-Float-Zone Melting," *J. Mater. Process. Technol.*, **117** [3] 401-9 (2001).

51. G. Malakondaiah and P.R. Rao, "Creep of Alpha-Titanium at Low Stresses," *Acta Metall.*, **29** [7] 1263-75 (1981).

52. P.R. Smith, M. Khobaib, and J.A. Graves, "Creep Behavior of an Alpha-2 and an Orthorhombic Ti-Based Matrix," *Scr. Metall. Mater.*, **29** [10] 1313-18 (1993).

53. S.R. Woodard and T.M. Pollock, "Transverse Creep in Ti-22Al-23Nb/ SiC-reinforced Composites," pp. 265-276 in *Proceedings from Orthorhombic Titanium Matrix Composite Workshop*, *1996*, Tech. Rept. # WL-TR-97-4082. Edited by P.R. Smith. Wright Laboratory, Dayton, OH, 1997.

54. C.J. Boehlert and D.B. Miracle, "Part II. The Creep Behavior of Ti-Al-Nb O+BCC Orthorhombic Alloys," *Metall. Trans. A*, **30** [9] 2349-67 (1999).

55. C.J. Boehlert, "Microstructure, Creep, and Tensile Behavior of a Ti-12Al-38Nb(at.%) Beta + Orthorhombic Alloy," *Mater. Sci. Eng., A*, **267** [1] 82-98 (1999).

56. R.W. Hayes, "Minimum Strain Rate and Primary Transient Creep Analysis of a Fine Structure Orthorhombic Titanium Aluminide," *Scr. Mater.*, **34** [6] 1005-12 (1996).

57. T.K. Nandy, R.S. Mishra, A.K. Gogia, and D. Banerjee, "The Effect of Aluminum on the Creep Behavior of Titanium Aluminide Alloys," *Scr. Metall. Mater.*, **32** [6] 851-56 (1995).

58. O.A. Ruano, J. Wadsworth, and O.D. Sherby, "Harper-Dorn Creep in Pure Metals," *Acta Metall.*, **36** [4] 1117-28 (1988).

APPENDIX

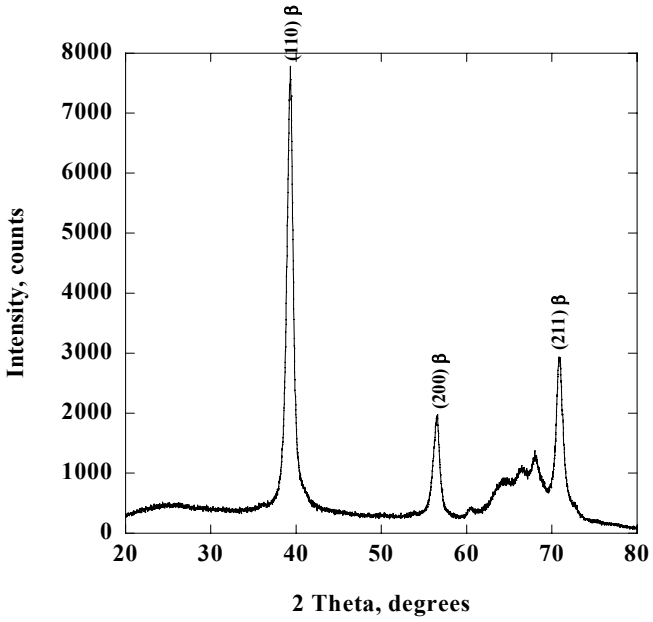

Figure A-1. AP Ti-15Al-33Nb XRD pattern.

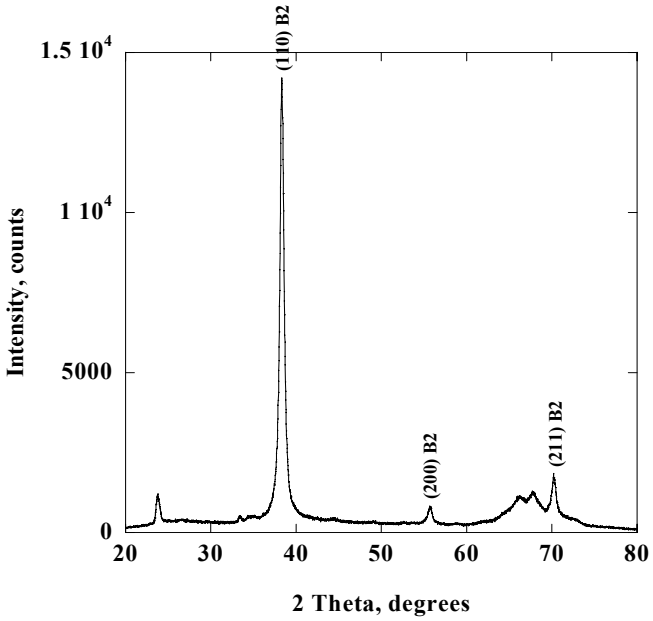

Figure A-2. AP Ti-21Al-29Nb XRD pattern.

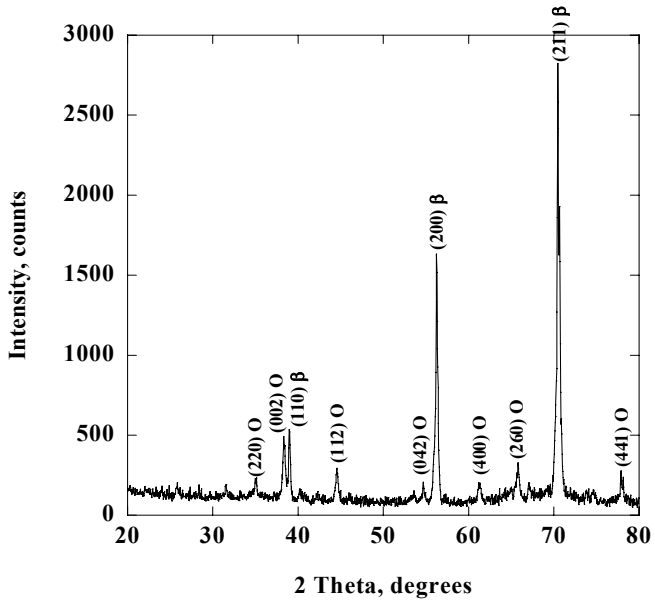

Figure A-3. Ti-15Al-33Nb HT:855°C/3h/WQ XRD pattern.

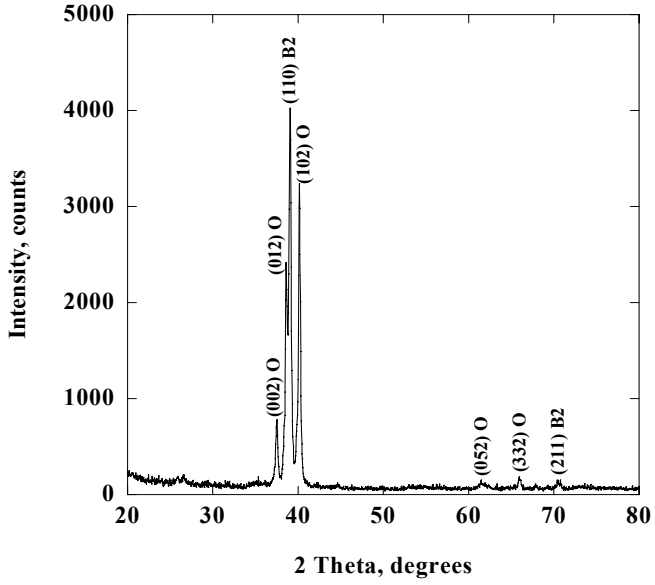

Figure A-4. Ti-21Al-29Nb HT:855°C/3h/WQ XRD pattern.

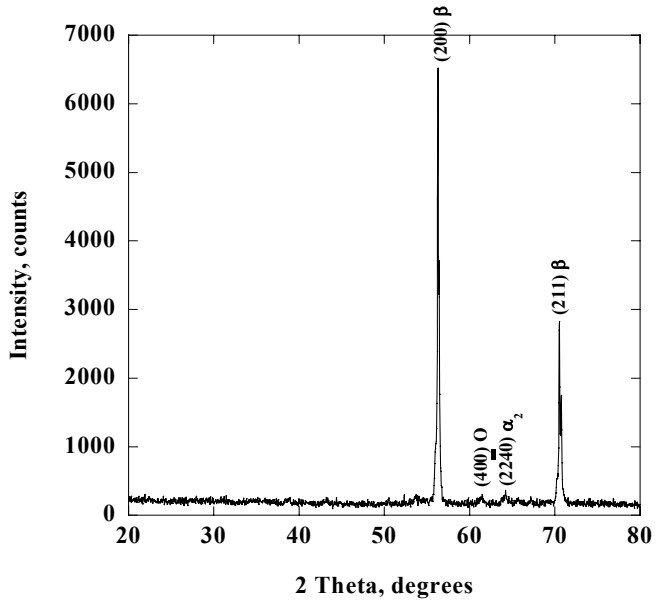

Figure A-5. Ti-15Al-33Nb HT:910°C/3h/WQ XRD pattern.

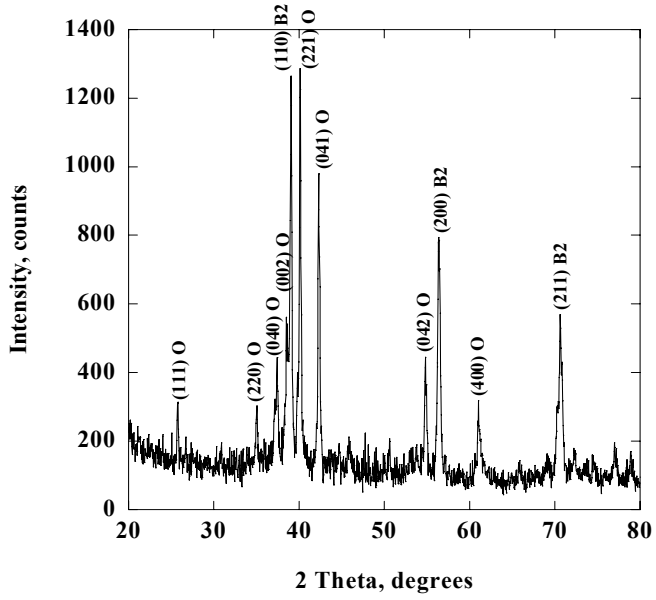

Figure A-6. Ti-21Al-29Nb HT:910°C/3h/WQ XRD pattern.

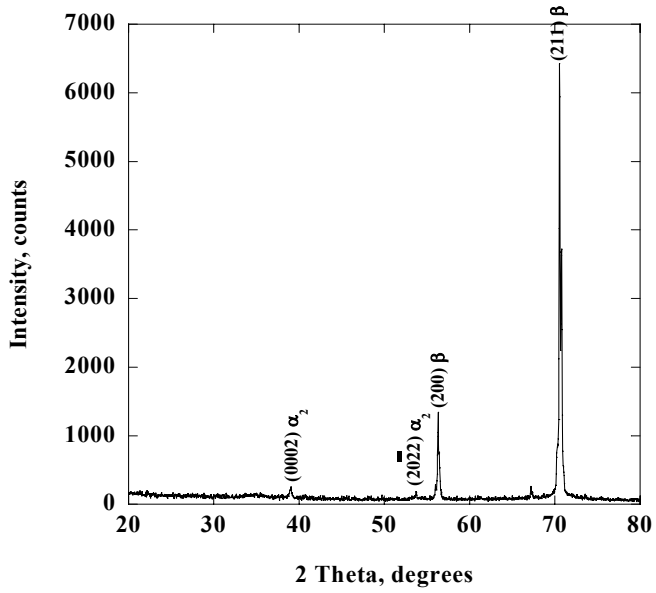

Figure A-7. Ti-15Al-33Nb HT:960°C/3h/WQ XRD pattern.

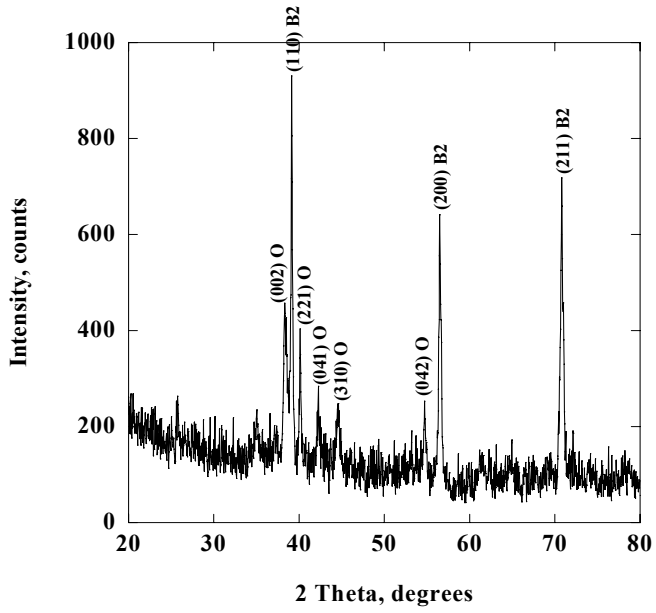

Figure A-8. Ti-21Al-29Nb HT:960°C/3h/WQ XRD pattern.

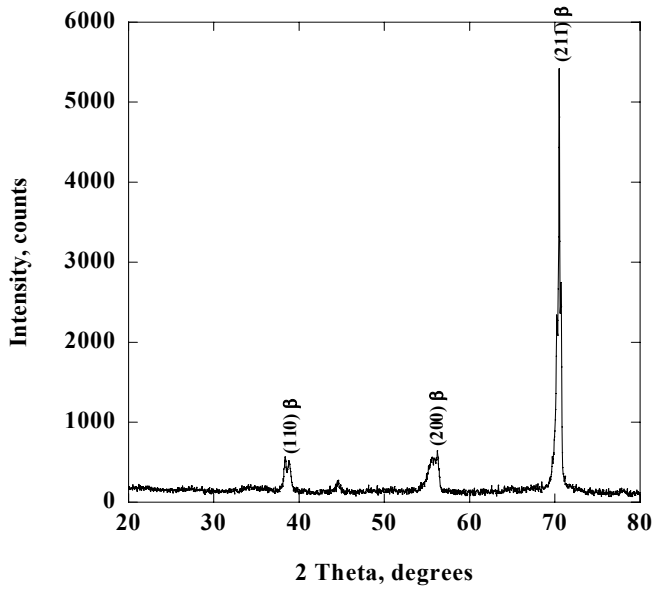

Figure A-9. Ti-15Al-33Nb HT:990°C/3h/WQ XRD pattern.

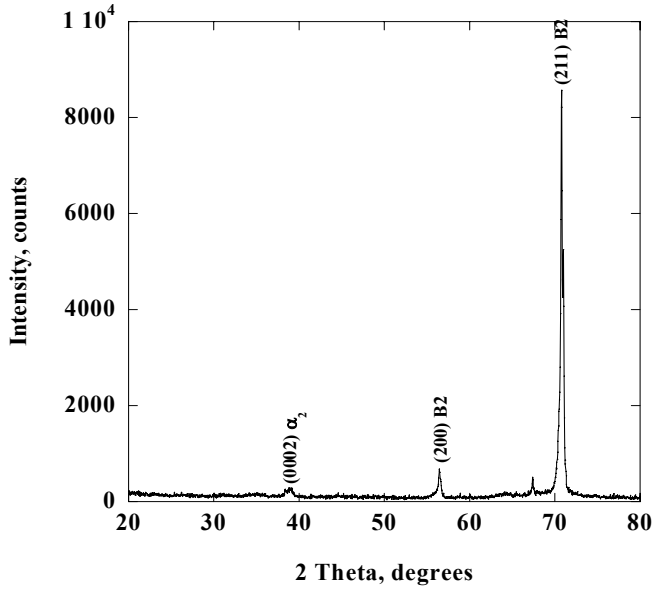

Figure A-10. Ti-21Al-29Nb HT:990°C/3h/WQ XRD pattern.

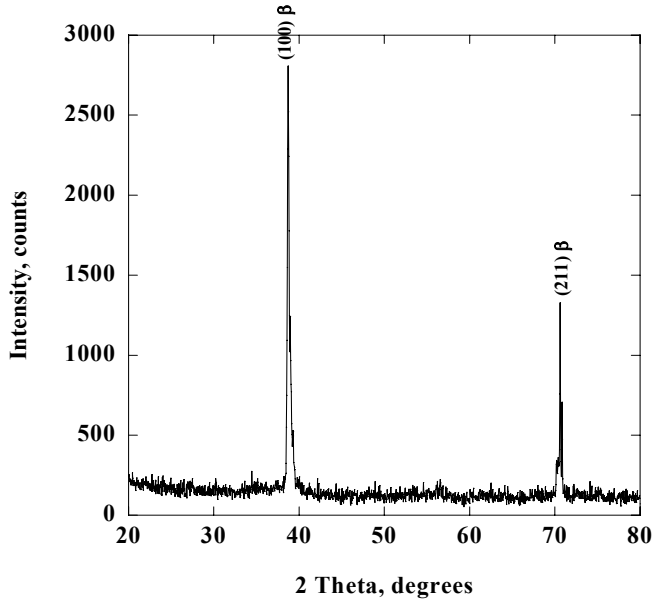

Figure A-11. Ti-15Al-33Nb HT:1005°C/3h/WQ XRD pattern.

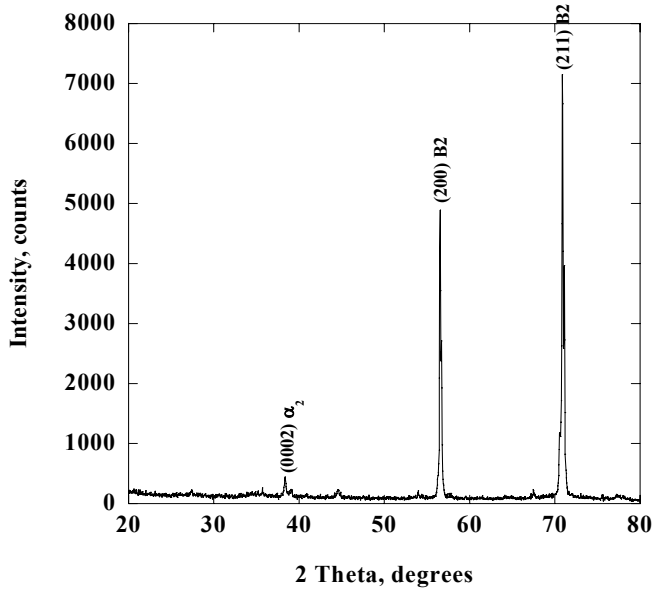

Figure A-12. Ti-21Al-29Nb HT:1005°C/3h/WQ XRD pattern.

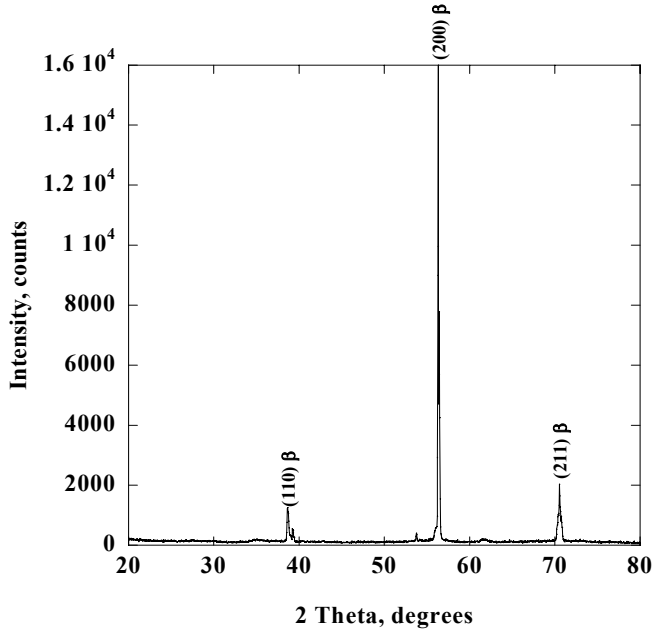

Figure A-13. Ti-15Al-33Nb HT:1050°C/3h/WQ XRD pattern.

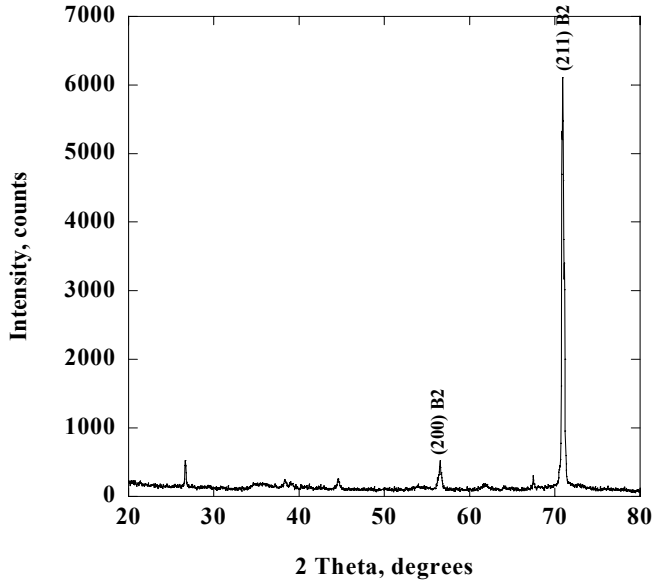

Figure A-14. Ti-21Al-29Nb HT:1050°C/3h/WQ XRD pattern.

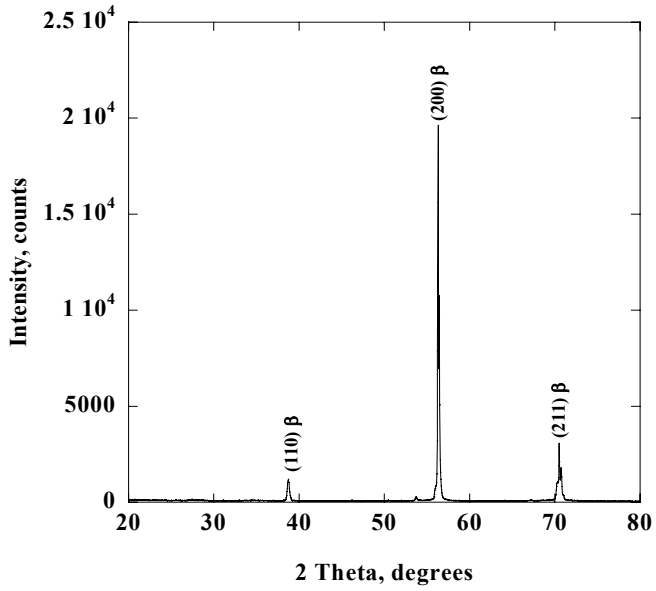

Figure A-15. Ti-15Al-33Nb HT:1075°C/3h/WQ XRD pattern.

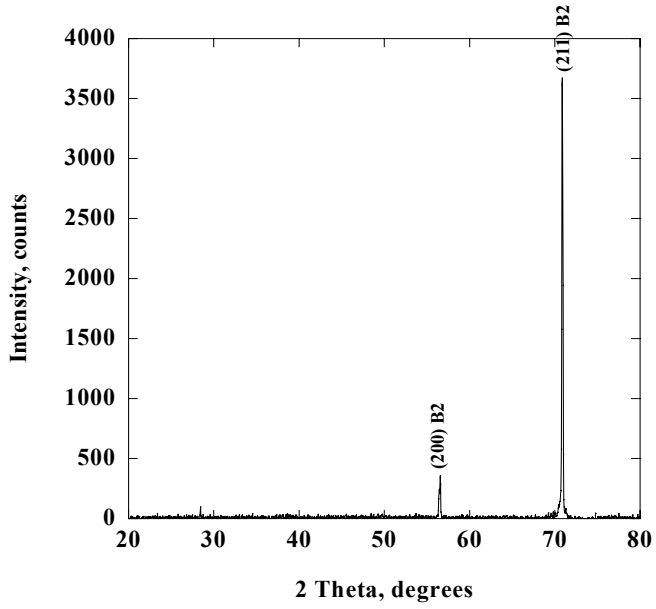

Figure A-16. Ti-21Al-29Nb HT:1075°C/3h/WQ XRD pattern.

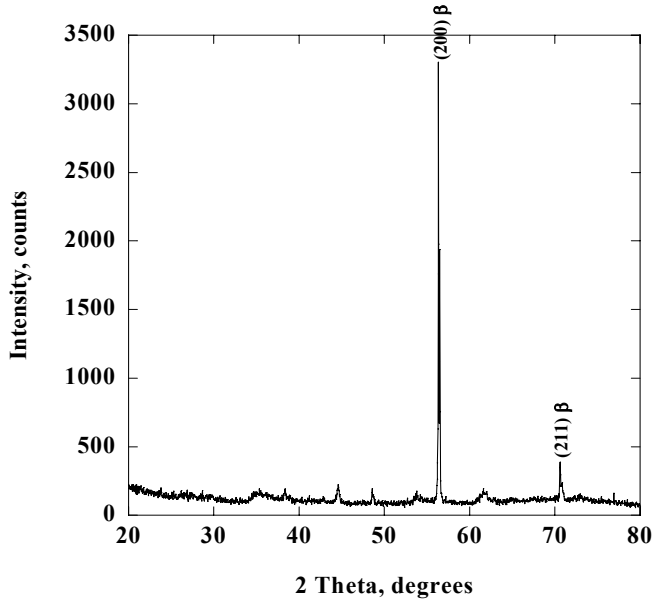

Figure A-17. Ti-15Al-33Nb HT:1105°C/3h/WQ XRD pattern.

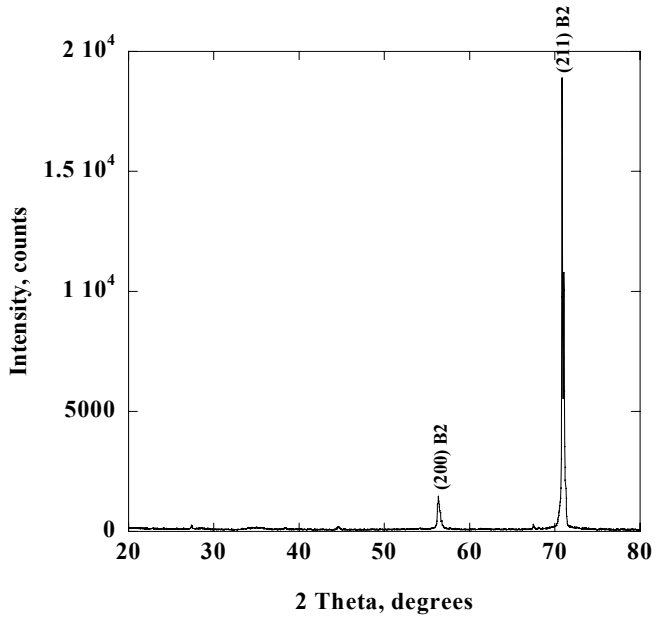

Figure A-18. Ti-21Al-29Nb HT:1105°C/3h/WQ XRD pattern.

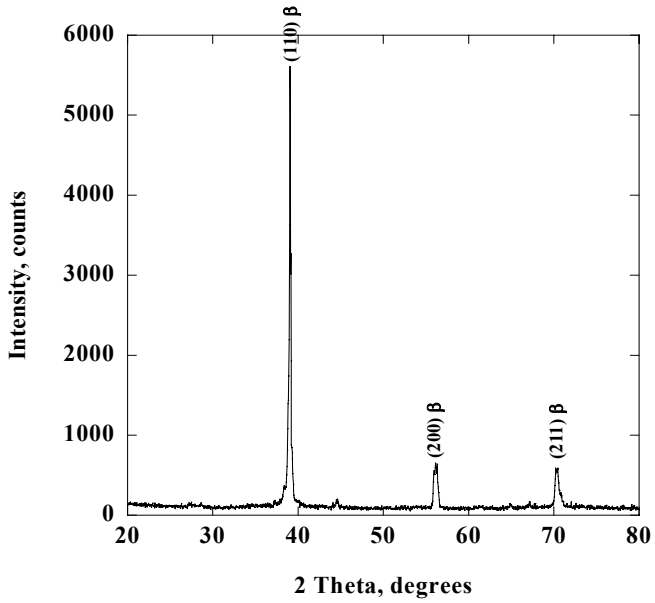

Figure A-19. Ti-16Al-33Nb HT:1105°C/3h/WQ XRD pattern.

Table A-I. Activation Energy Range Determined for Creep-Tested Samples

Stress, MPa	Alloy	Heat Treatment, °C	Activation Energy Determined, kJ/mol	Activation Energy + Estimated Resolution, kJ/mol	Activation Energy - Estimated Resolution, kJ/mol	Activation Energy Range, kJ/mol
50	Ti-15Al-33Nb	HT:960	115	80	166	80-166
	Ti-21Al-29Nb	HT:960	292	n/a	105	105-292
150	Ti-15Al-33Nb	HT:1005	163	118	239	118-239
	Ti-15Al-33Nb	HT:1105	181	128	281	128-281
	Ti-21Al-29Nb	HT:1005	215	175	279	175-279
275	Ti-15Al-33Nb	HT:1005	288	278	298	278-298
	Ti-15Al-33Nb	HT:1105	317	303	333	303-333

n/a indicates estimated resolution was greater than measured strain rate

Table A-II. Activation Energy Range Determined for BCC Grain Growth

Alloy	Activation Energy Determined, kJ/mol	Activation Energy Determined + Estimated Resolution, kJ/mol	Activation Energy Determined - Estimated Resolution, kJ/mol	Activation Energy Range, kJ/mol
Ti-15Al-33Nb	194	192	197	192-197
Ti-21Al-29Nb	311	305	317	305-317